

**Realization of $\text{YBa}_2\text{Cu}_3\text{O}_{7-\delta}$
nanostructures with a focused
Helium ion beam**

Dissertation

der Mathematisch-Naturwissenschaftlichen Fakultät
der Eberhard Karls Universität Tübingen
zur Erlangung des Grades eines
Doktors der Naturwissenschaften
(Dr. rer. nat.)

vorgelegt von
Max Karrer
aus Stuttgart

Tübingen
2024

Gedruckt mit Genehmigung der Mathematisch-Naturwissenschaftlichen Fakultät der Eberhard Karls Universität Tübingen.

Tag der mündl. Qualifikation:	18.07.2024
Dekan:	Prof. Dr. Thilo Stehle
1. Berichterstatter:	Prof. Dr. Dieter Kölle
2. Berichterstatter:	Prof. Dr. Alexander Buzdin

Abstract

Helium ion microscopy is a leading edge imaging technology that uses a beam of helium ions to acquire high-resolution images of a wide range of materials and specimens down to the nanoscale level. Beside the excellent imaging quality, not least because of the contrast mechanisms, the helium ion microscope can be simultaneously operated as a tool for nanostructuring. One approach, which was pursued in the context of this thesis, is the local modification of superconducting properties of $\text{YBa}_2\text{Cu}_3\text{O}_{7-\delta}$ thin films by irradiation with a focused helium ion beam created by a helium ion microscope. This technique allows for versatile and more complex circuit designs compared to state-of-the-art Josephson Junctions based on grain boundaries in $\text{YBa}_2\text{Cu}_3\text{O}_{7-\delta}$.

The first part deals with the characterization of Josephson Junctions and superconducting quantum interference devices, created by helium ion beam irradiation and their evolution with time when stored at room temperature. Through the choice of the irradiation dose, the electrical properties of these devices can be adjusted. When irradiated with a sufficiently high dose, the material can be driven into an insulating state with completely suppressed superconductivity, enabling to define geometries without removal of material.

Furthermore, by the same principle, this technique is capable of creating artificial pinning centers for Abrikosov vortices. In previous work, pinning arrays exhibited matching effects, i.e., effects of commensurability between the vortex lattice and the pinning array, only in the vicinity of the critical temperature of the thin film,

due to limitations in the nearest neighbor distance of artificial pinning sites obtained with the used fabrication techniques. By utilizing a focused helium ion beam beam, it becomes possible to fabricate pinning arrays with spacings down to 20 nm and first matching fields (where the densities of pinning centers and vortices coincide) up to 6 T over a wide temperature range significantly below the critical temperature, confirming strong pinning of the vortices at the artificially engineered pinning centers.

Kurzfassung

Die Helium-Ionen-Mikroskopie ist eine hochmoderne Bildgebungstechnologie, bei der ein Helium-Ionenstrahl eingesetzt wird, um hochauflösende Bilder einer breiten Palette von Materialien und Proben bis in den Nanobereich zu erstellen. Neben der hervorragenden Abbildungsqualität, nicht zuletzt aufgrund der Kontrastmechanismen, kann das Gerät gleichzeitig als Werkzeug für die Nanostrukturierung eingesetzt werden. Ein Ansatz, der im Rahmen dieser Arbeit verfolgt wurde, ist die lokale Modifikation der supraleitenden Eigenschaften von $\text{YBa}_2\text{Cu}_3\text{O}_{7-\delta}$ -Dünnschichten durch Bestrahlung mit einem fokussierten Helium-Ionenstrahl, der durch ein Helium-Ionenmikroskop erzeugt wird. Diese Technik ermöglicht vielseitigere und komplexere Schaltungsentwürfe im Vergleich zum Stand der Technik, der auf Korngrenzen in $\text{YBa}_2\text{Cu}_3\text{O}_{7-\delta}$ basiert.

Der erste Teil befasst sich mit der Charakterisierung von Josephson-Kontakten und supraleitenden Quanteninterferometern, die durch die Bestrahlung mit Helium-Ionenstrahlen erzeugt wurden, und ihrer zeitlichen Entwicklung bei Lagerung bei Raumtemperatur. Durch die Wahl der Bestrahlungsdosis können die elektrischen Eigenschaften dieser Bauteile eingestellt werden. Wenn das Material mit einer ausreichend hohen Dosis bestrahlt wird, kann es in einen isolierenden Zustand mit vollständig unterdrückter Supraleitung versetzt werden, wodurch sich Geometrien ohne Materialabtrag definieren lassen.

Außerdem können mit dieser Technik nach demselben Prinzip künstliche Pinning-Zentren für Abrikosov-Wirbel erzeugt werden. In früheren Arbeiten zeigten Pinning-Arrays nur in der Nähe der kritischen Temperatur des Dünnsfilms "Matching"-Effekte, d.h., Kommensurabilitätseffekte zwischen dem Vortex-Gitter und dem Pinning-Array, was auf den begrenzten Abstand der nächsten Nachbarn von künstlichen Haftzentren bei den verwendeten Herstellungstechniken zurückzuführen ist. Durch die Verwendung eines fokussierten Helium-Ionenstrahls ist es möglich, Pinning-Arrays mit Abständen von bis zu 20 nm und ersten Matching-Feldern (bei denen die Dichten der Haftzentren und Flusswirbel übereinstimmen) von bis zu 6 T über einen weiten Temperaturbereich deutlich unterhalb der kritischen Temperatur herzustellen, was ein starkes Pinning der Wirbel an den künstlich hergestellten Pinning-Zentren bestätigt.

List of Publications

This is a cumulative thesis based on the 6 publications presented below, divided into two thematic sections within each of which they are listed chronologically. Publications 1 and 2 address the fabrication and characterization of Josephson Junctions (JJs) and superconducting quantum interference devices (SQUIDs), as well as the evolution with respect to time of the former when stored at room temperature, whereas publications 3 to 6 deal with the engineering process and investigation of vortex pinning landscapes in type-2 superconductors. In all publications, the high-temperature superconductor $\text{YBa}_2\text{Cu}_3\text{O}_{7-\delta}$ (YBCO) has been used as the thin film material.

All publications are appended at the end of this thesis, while a comprehensive summary can be found in Chapter 2 for each manuscript.

Josephson Junctions and SQUIDs

- Publication 1** B. Müller, **M. Karrer**, F. Limberger, M. Becker, B. Schröppel, C. J. Burkhardt, R. Kleiner, E. Goldobin, and D. Koelle
Josephson Junctions and SQUIDs Created by Focused Helium-Ion-Beam Irradiation of $\text{YBa}_2\text{Cu}_3\text{O}_7$
Physical Review Applied **11**, 044082 (2019)

Publication 2 M. Karrer, K. Wurster, J. Linek, M. Meichsner, R. Kleiner, E. Goldobin, and D. Koelle
Temporal evolution of electric transport properties of $YBa_2Cu_3O_{7-\delta}$ Josephson junctions produced by focused helium-ion-beam irradiation
Physical Review Applied **21**, 014065 (2024)

Pinning Arrays

Publication 3 B. Aichner, B. Müller, M. Karrer, V. R. Misko, F. Limberger, K. L. Mletschnig, M. Dosmailov, J. D. Pedarnig, F. Nori, R. Kleiner, D. Koelle, and W. Lang
Ultradense Tailored Vortex Pinning Arrays in Superconducting $YBa_2Cu_3O_{7-\delta}$ Thin Films Created by Focused He Ion Beam Irradiation for Fluxonics Applications
ACS Applied Nano Materials **2**, 5108 (2019)

Publication 4 B. Aichner, K. L. Mletschnig, B. Müller, M. Karrer, M. Dosmailov, J. D. Pedarnig, R. Kleiner, D. Koelle, and W. Lang
Angular magnetic-field dependence of vortex matching in pinning lattices fabricated by focused or masked helium ion beam irradiation of superconducting $YBa_2Cu_3O_{7-\delta}$ thin films
Low Temperature Physics **46**, 331 (2020)

- Publication 5** L. Backmeister, B. Aichner, **M. Karrer**, K. Wurster, R. Kleiner, E. Goldobin, D. Koelle, and W. Lang
Ordered Bose Glass of Vortices in Superconducting $YBa_2Cu_3O_{7-\delta}$ Thin Films with a Periodic Pin Lattice Created by Focused Helium Ion Irradiation
Nanomaterials **12**, 3491 (2022)
- Publication 6** **M. Karrer**, B. Aichner, K. Wurster, C. Magén, C. Schmid, R. Hutt, B. Budinská, O. V. Dobrovolskiy, R. Kleiner, W. Lang, E. Goldobin, and D. Koelle
Vortex matching at 6 T in $YBa_2Cu_3O_{7-\delta}$ thin films by imprinting a 20-nm periodic pinning array with a focused helium-ion beam
Physical Review Applied **22**, 014043 (2024)

Publications not included in this thesis

- Publication I** J. Lin, B. Müller, J. Linek, **M. Karrer**, M. Wenzel, M. J. Martínez-Pérez, R. Kleiner, and D. Koelle
YBa₂Cu₃O₇ nano superconducting quantum interference devices on MgO bicrystal substrates
Nanoscale **12**, 5658 (2020)
- Publication II** B. Aichner, L. Backmeister, **M. Karrer**, K. Wurster, R. Kleiner, E. Goldobin, D. Koelle, and W. Lang
Angle-dependent Magnetoresistance of an Ordered Bose Glass of Vortices in YBa₂Cu₃O_{7-δ} Thin Films with a Periodic Pinning Lattice
Condensed Matter **8**, 32 (2023)
- Publication III** J. Niu, K. M. Bastiaans, J.-F. Ge, R. Tomar, J. Jesudasan, P. Raychaudhuri, **M. Karrer**, R. Kleiner, D. Koelle, A. Barbier, E. F. C. Driessen, Y. M. Blanter, and M. P. Allan
Why Shot Noise Does Not Generally Detect Pairing in Mesoscopic Superconducting Tunnel Junctions
Physical Review Letters **132**, 076001 (2024)

Contents

1	Introduction	1
2	Summary of publications and contributions	17
2.1	Josephson Junctions and SQUIDs	18
2.1.1	Publication 1: Josephson Junctions and SQUIDs Created by Focused Helium-Ion-Beam Irradiation of $\text{YBa}_2\text{Cu}_3\text{O}_7$	18
2.1.2	Publication 2: Temporal evolution of electric transport properties of $\text{YBa}_2\text{Cu}_3\text{O}_{7-\delta}$ Josephson junctions produced by focused helium-ion- beam irradiation	24
2.2	Vortex pinning arrays	33

2.2.1	Publication 3: Ultradense Tailored Vortex Pinning Ar- rays in Superconducting $\text{YBa}_2\text{Cu}_3\text{O}_{7-\delta}$ Thin Films Created by He Ion Beam Irra- diation for Fluxonics Applications	33
2.2.2	Publication 4: Angular magnetic-field dependence of vor- tex matching in pinning lattices fabricated by focused or masked helium ion beam irra- diation of superconducting $\text{YBa}_2\text{Cu}_3\text{O}_{7-\delta}$ thin films	40
2.2.3	Publication 5: Ordered Bose Glass of Vortices in Su- perconducting $\text{YBa}_2\text{Cu}_3\text{O}_{7-\delta}$ Thin Films with a Periodic Pin Lattice Created by Focused Helium Ion Irradiation	45
2.2.4	Publication 6: Vortex matching at 6 T in $\text{YBa}_2\text{Cu}_3\text{O}_{7-\delta}$ thin films by imprinting an ultradense hexagonal pinning array with a focused helium ion beam	51
3	Conclusion and outlook	61
	List of acronyms	65
	Bibliography	69
	Appended publications	75

Chapter 1

Introduction

Charged-particle microscopes are essential for applications where high-resolution imaging or patterning of the specimen is required. Well-known representatives are the scanning electron microscope (SEM) and the focused ion beam (FIB)¹ which are often combined into a single instrument to benefit from the complementary advantages. However, in terms of mass, they are basically on both ends of the spectrum, with electrons being on the light side and gallium ions on the heavy side of the charged particles typically used in this kind of microscopes. The heavier gallium ions allow for significant milling rates for various elements and compounds, while there is typically no milling effect

¹Especially the commonly used gallium focused ion beam (Ga-FIB).

when using electrons in an SEM. Nonetheless, specimen damage and degradation, e.g. due to heating, electrostatic charging, ionization damage and hydrocarbon contamination, can occur for certain acceleration voltages [1].

In 2007, the gas field ion source (GFIS) became commercially available as the source of the helium ion microscope (HIM), allowing one the use of helium ions, which are much more massive compared to electrons, but still less heavy than most of the other elements in the periodic table [2]. The key element for the creation of helium ions within the GFIS is an atomically sharp tip made out of tungsten surrounded by a defined atmosphere of helium gas with typical pressures on the order of 1×10^{-6} Torr [3]. By utilizing special procedure, the apex of the tip can be shaped in a way that allows it to be formed by only three tungsten atoms and therefore referred to as a *trimer*. With this geometry, the increase of the electric field in the vicinity of one trimer atom can be used to ionize the surrounding helium atoms by applying a sufficiently high enough positive extractor voltage to the trimer with respect to the extractor aperture. After ionization, the helium ions are accelerated to energies up to 30 keV and controlled by electrostatic lenses, quadrupoles and octupoles to obtain a small probe size of down to 0.25 nm on the specimen surface [4]. Alternatively, just by exchanging the helium with neon gas, a focused neon beam can be provided, further closing the gap between electrons and gallium ions².

²It should be noted that the term HIM is used even if it technically could also be a neon ion microscope (NIM).

The HIM does not only outperform other microscopes with respect to spatial resolution, but also enables other techniques for research due to different contrast mechanisms [5, 6], and allows for secondary ion mass spectroscopy (SIMS) [7] as well as the imaging of insulating, e.g. biological, samples by utilizing a built-in electron flood gun for charge compensation of the positively charged helium ions [8]. In some sense, the Ga-FIB is the axe and the HIM is the scalpel of nanostructuring while simultaneously offering new possibilities and methods for material analysis.

With the development of the HIM a new era in nanofabrication started, allowing for more sophisticated and precise structuring methods of various materials on the nanoscale. Among the most promising materials in the field of superconductivity is the type-II cuprate superconductor YBCO. The advantages of YBCO are a high critical temperature of around 93 K and a larger upper critical magnetic field compared to other well-researched materials like niobium, which is interesting for technical applications. However, YBCO sets high demands on the fabrication side and is challenging to handle due to its small coherence length, making the superconducting properties susceptible to local lattice defects in the YBCO. The orthorhombic³ crystal structure of YBCO is shown in Fig. 1.1 and mainly consists of two roughly 0.3 nm spaced CuO₂ planes, between which an yttrium ion is located. This structure follows a plane of barium oxide and a CuO plane, also referred to as CuO chains, since in *b*-direction, copper ions alternate with oxygen ions, while in *a*-direction, the oxygen is missing. Superconductivity takes place

³Lattice parameters $a \approx 3.820 \text{ \AA}$, $b \approx 3.885 \text{ \AA}$, $c \approx 11.683 \text{ \AA}$ [9]

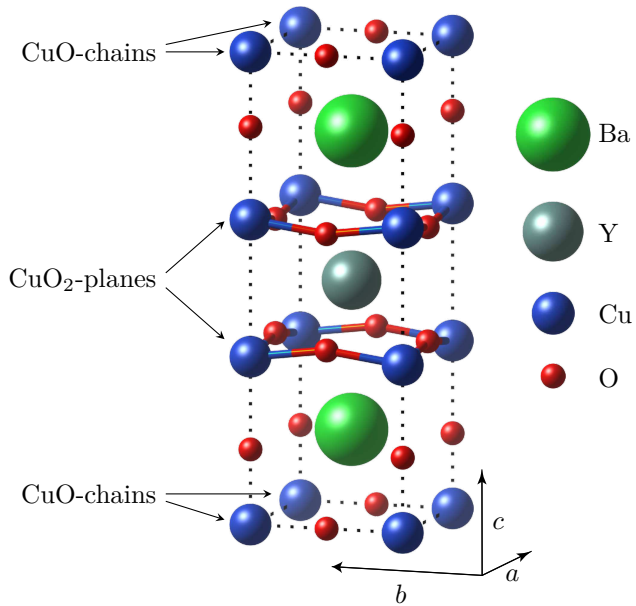


Figure 1.1: Unit cell of the crystal structure of $\text{YBa}_2\text{Cu}_3\text{O}_{7-\delta}$ with $\delta = 0$. Atomic coordinates were taken from [9] and atoms were drawn to scale with their corresponding atomic radii from [10].

in the CuO_2 planes, while the other planes act as a charge carrier supply to form Cooper pairs. The phase diagram of YBCO is shown in Fig. 1.2 and indicates the essential role of the oxygen deficiency δ for the properties of YBCO [11]. For $\delta = 1$, the oxygen in the CuO chains is not apparent anymore and the material can be described as an antiferromagnetic insulator. At $\delta \approx 0.6$, the antiferromagnetic phase vanishes and a transition into the superconducting phase can be observed. In the range $0.25 \lesssim \delta \lesssim 0.5$, a plateau with a critical temperature of 60 K is established, and for lower values, the maximum value of 93 K is reached right before $\delta = 0$ [12].

Superconductivity is generally known for a vanishing resistance below a material-dependent critical temperature, where the electrical current is, other than with normal conducting materials, not carried by single electrons, but instead by paired electrons forming *Cooper pairs* as stated in the BCS-Theory [13]. However, there is more to superconductivity, as experiments conducted by W. Meissner and R. Ochsenfeld in 1933 revealed that it has to be considered a novel thermodynamic phase [14]. The Meissner-Ochsenfeld effect shows that a superconductor will expel any magnetic field from entering the inside once it is cooled down below its corresponding critical temperature T_c . Thus, a superconductor is not only a perfect conductor, but also an ideal diamagnet with a magnetic susceptibility $\chi = -1$. But that is only half the story, because to expel the outer magnetic field, screening currents near the surface of the superconductor will flow and the magnetic field will exponentially decay towards the volume inside. In 1937, L. Shubnikov et al. found that above a certain magnetic field some superconductors are penetrated by

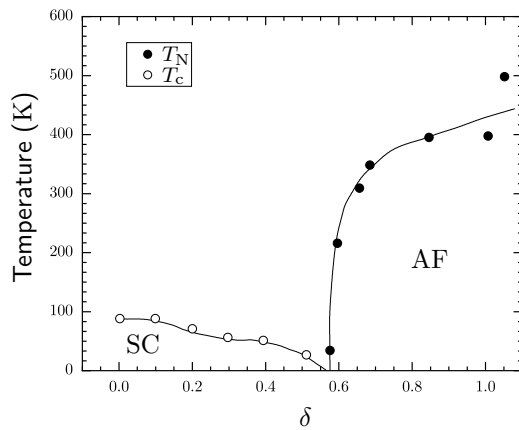


Figure 1.2: Phase diagram oxygen deficiency δ vs. temperature of $\text{YBa}_2\text{Cu}_3\text{O}_{7-\delta}$ with superconducting (SC) and antiferromagnetic (AF) phases. T_N denotes the Néel-temperature and T_c the critical temperature. Data was extracted from [12].

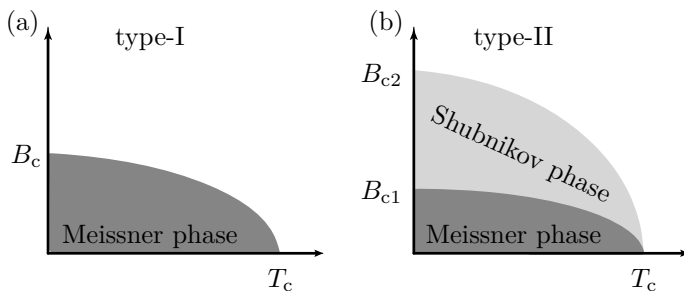


Figure 1.3: Schematic phase diagram of (a) type-I and (b) type-II superconductors with respect to temperature and magnetic field. The dark gray area indicates the Meissner phase and the Shubnikov phase is shown in light gray.

magnetic flux while maintaining ideal conductivity [15]. To distinguish them from superconductors only showing the Meissner effect, they are referred to as second kind or type-II superconductors. The phase diagram of type-I and type-II superconductors is shown in Fig. 1.3.

A type-I superconductor remains in the Meissner phase until the critical magnetic field B_c is reached and the material transitions into the normal conducting state. A type-II superconductor, on the other hand, has two critical fields. For fields

smaller than the lower critical field B_{c1} , it stays in the Meissner phase, whereas above this threshold, magnetic flux can penetrate the superconductor until the magnetic field reaches the upper critical field B_{c2} where the superconductive state collapses.

The physics of superconductors can phenomenologically be described by means of the Ginzburg-Landau (GL) theory [16]. Based on Landau's theory for second order phase transitions, Landau and Ginzburg argue that the free energy F of a superconductor near the transition to the superconducting state can be expressed by the order parameter Ψ that is identified as the complex quantum mechanical wavefunction describing the superconducting charge carriers (Cooper pairs) on a macroscopic scale. From the GL equations, two important characteristic length scales can be extracted. The first one is the coherence length ξ , which describes the scale on which thermodynamic fluctuations of the superconductor can be compensated, and determines the surface tension between the normal and superconducting phases. The second is the penetration depth λ describing the typical length scale on which a magnetic field can penetrate the superconductor. In 1957, A. A. Abrikosov realized that with the Ginzburg-Landau parameter $\kappa = \lambda/\xi$, one can differentiate between type-I and type-II superconductors because for $\kappa > 1/\sqrt{2}$, the free energy of an interface between a normal and superconducting phase is negative [17]. If the lower critical magnetic field is reached, it is energetically preferable, from an energetic point of view, to locally give up superconductivity and let magnetic flux through the now normal conducting volume. This arrangement is then referred to as an Abrikosov vortex. A single vortex exhibits cylindrical symmetry and the amount

of magnetic flux carried by a vortex is determined by one flux quantum $\Phi_0 = h/2e$, wherein h is Planck's constant and e the elementary charge. The dependence of the magnetic field, critical current and Cooper pair density of an isolated vortex with $\kappa \gg 1$ on the radial distance r from the vortex center are shown in Fig. 1.4. The magnetic field can be described through

$$B_z(r) = \frac{\Phi_0}{2\pi\lambda^2} K_0\left(\frac{\sqrt{r^2 + 2\xi_v^2}}{\lambda}\right) \quad , \quad (1.1)$$

with $K_0(x)$ being a zeroth-order, modified Bessel function⁴, r the radial component in cylindrical coordinates and ξ_v a variational core parameter with the same magnitude as the coherence length ξ [19]. Two vortices placed in a distance next to each other will experience repelling forces if oriented in the same direction. In a perfect type-II superconductor without any defects, this results in vortices arranging in a hexagonal lattice, thus minimizing the interaction energy. Besides the vortex-vortex interaction potential, the landscape of intrinsic or artificially created defects, so called *pinning sites*, in the material is of utmost importance. Here, the reduced condensation energy of the superconductor, either due to weakened or suppressed superconductivity makes it energetically preferable for the vortex to enter such pinning sites. By applying a current flow through the superconductor, a Lorentz force will be exerted on the vortices, limiting the maximum supercurrent when the vortices start depinning from the pinning sites, which leads to a dissipative vortex motion.

⁴With the limits $-\ln(x)$ for $x \ll 1$ and $(\pi/2x)^{1/2} \exp(-x)$ for $x \gg 1$.

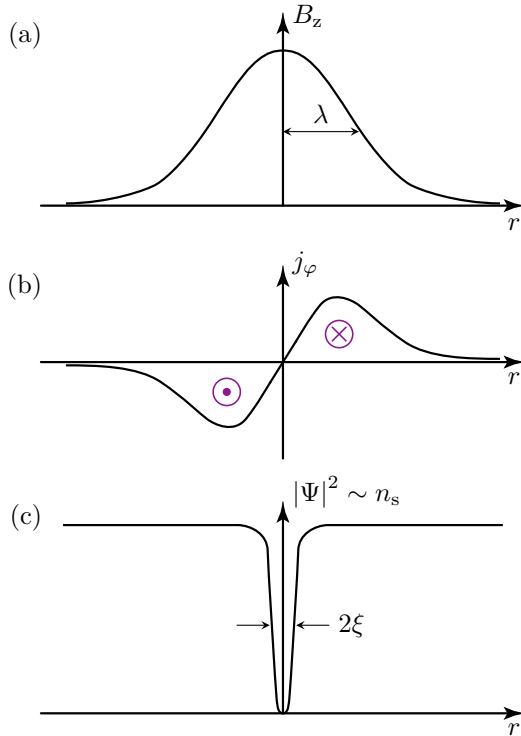


Figure 1.4: Schematic of the cross section with dependence of (a) magnetic field B_z , (b) current density j_φ , (c) cooper pair density n_s for an Abrikosov vortex. The arrows in (b) indicate the direction of the current density. Mathematical expressions can be found in Ref. [18].

In general there is a complex interplay between the different contributors to the overall pinning potential, which are usually temperature dependent. In regular pinning arrays, matching effects will occur if the applied magnetic field B fulfills the matching condition

$$B_n = n \cdot \frac{\Phi_0}{A} \quad , \quad (1.2)$$

where n denotes the number of pinned vortices within one unit cell of the regular array and A the area of such a unit cell.

Another important phenomenon in the field of superconductors is the so called Josephson effect [20]. This feature can be observed if two superconductors are close to each other with respect to the overlapping macroscopic wavefunctions outside the superconductors. If such a weak link between two superconductors exists, a JJ is formed - the basic device in superconducting electronic circuits. Using two JJs connected in parallel within a superconducting ring will result in a so-called SQUID, a highly sensitive device which can be used to measure magnetic fields down to the femtotesla range [21, 22]. SQUIDs were also used in the *Gravity Probe B* experiment funded by the National Aeronautics and Space Administration (NASA) in cooperation with the Stanford University to verify predictions of Einstein's theory of gravity, widely known as general relativity, conducted between 2004 and 2006 [23].

There are a variety of other application fields for SQUIDs. From medical applications as magnetoencephalography (MEG), where SQUIDs are used to measure neural activities by detecting magnetic fields, typically 10 fT for cortical activity and 10^3 fT for the human alpha rhythm, produced by electrical currents inside

the brain or magnetic resonance imaging (MRI), a technique for imaging the interior of a body for clinical analysis without the use of X-rays or ionizing radiation which is therefore less harmful to biological tissue. While in conventional high-field MRI magnetic fields, up to several teslas are used, MRI with SQUID readout can be operated at much lower magnetic fields in the microtesla to millitesla range [24–26]. Not only do such systems benefit from lower costs, but they are also more compact in comparison to conventional MRI as there is no need for generating large magnetic fields, where devices are bulky and expensive.

Considering the rapid development regarding computer science in the past few years, JJs and SQUIDs are also of interest to develop the analog to a bit in quantum computing - a quantum bit (qubit). Various designs of qubits have been developed, including the Cooper pair box [27] based on charge, the flux qubit [28], and the phase qubit [29] to implement a two-state system with quantum superposition. Advantages of superconducting qubits over other types are faster gate times and the fact that they can leverage advanced chip-making technologies, which makes manufacturing efficient and scalability easier compared to other technologies.

An example for an application in research for the analysis of a specimen is the scanning SQUID microscope (SSM). The SSM enables the imaging of a variety of physical quantities near the surface by placing a SQUID onto a tip which is then rastered over the sample surface enabling a mapping of magnetic fields [30], magnetic susceptibility [31], and electric currents [32] to the topography of the specimen. One of the main parts of this thesis was contributing fundamental scientific research on helium ion

induced barriers in YBCO and paving the way for more complex and sophisticated devices within a project called *FIBsuperProbes* [33], funded by the European Union, targeting a new era for SSM with unprecedented size, functionality and sensitivity of individually designed cantilevers to improve the understanding of phenomena in physics, chemistry and material science, which are intractable in current state-of-the-art technology.

The overall challenge when dealing with superconductors lies in the fact, that commonly used conventional superconductors like niobium and aluminium exhibit a low critical temperature below 10 K and a low critical magnetic field which limits the range of operation with devices based on such materials. As already stated, YBCO extends the operation range with a critical temperature of 93 K and an upper critical magnetic field⁵ up to 140 T [34]. However, the complex crystal structure shifts the challenges onto the side for fabrication and handling of the thin films. The state-of-the-art approach for the fabrication of superconducting devices in YBCO such as JJs is based on grain boundaries (GBs) utilizing a bicrystal substrate consisting of two crystals with different orientations of the crystal axis joined together so that an artificial grain boundary is created [35]. Epitaxially grown YBCO on top of the bicrystal has the same orientation as the underlying bicrystal layer and will therefore form a grain boundary itself at the same location as the bicrystal substrate underneath, hence limiting the degree of freedom and complexity of the circuit design since junctions can only be

⁵Applied parallel to the c -axis.

placed along the substrates grain boundaries. Moreover, it is noteworthy that bicrystal substrates are typically more expensive than their conventional counterparts due to the intricacies of their manufacturing process.

Previous work to create Josephson barriers in cuprate superconductors by irradiation with high-energy electrons [36, 37] or oxygen ions [38–40] resulted in inferior junction quality compared to GB based JJs, either because of limitations in the size of the slit in the irradiation mask or the straggling of the particles inside the sample, which leads to a broadening of the barrier. With the upcoming of the GFIS, irradiation with helium ions at sub-nm resolution became available, a technique which was first used and published by Cybart et al. in 2015. In their paper, an HIM is exploited to irradiate the YBCO, thus locally modifying the superconducting properties by inducing atom displacements to create thin barrier JJs, allowing them to be arbitrarily placed on the whole sample chip [41], making this fabrication technique a feasible and competitive option compared to GBJJs. This overcomes the limitations of the GBJJs technology and opens up the opportunity for a complete new way of circuit designing, which can be referred to as *direct write lithography* since no irradiation mask is used. In addition, a new parameter dose enters the field for adjusting the critical current density, as well as the properties of the barrier, while for GBJJs the only way to modify the created JJ after the thin film micro-structuring is by reducing the width, e.g. by ion beam milling. The creation of JJs with an HIM was recently demonstrated in other materials beside YBCO such as $\text{Bi}_2\text{Sr}_2\text{CaCu}_2\text{O}_{8+x}$ (BSCCO) flakes [42] and MgB_2 thin films [43].

This thesis is solely based on the described kind of fabrication technique and the interplay between YBCO and the HIM. In the first part, the research focus lies on the characteristics of JJs fabricated with a focused helium ion beam in YBCO. In **publication 1**, the first iteration of helium focused ion beam (He-FIB)JJs at the University of Tübingen are used to identify the impact of different dose values on the electric transport properties of the created barriers and for different sample substrates. This allowed for basic but crucial insights on how the standard process parameters influence the characteristics of these devices. During the handling and repeated measurements of our samples, we came across a change in the characteristics of these junctions when exposed to room temperature in between measurements. Subsequently, in order to better understand and control the properties of such devices, a quantitative study enclosed within **publication 2** was conducted to describe the effects of aging for helium ion induced barriers in YBCO and how they behave when treated with a post-annealing step under different partial oxygen pressures with the aim to pinpoint important timescales and mechanisms to increase the relaxation velocity for a faster transition into the state of equilibrium. Another promising approach, where the local modification of YBCO with an HIM can be applied, is to introduce artificial pinning centers into a thin film. As already described, YBCO is a type-II superconductor which, in its Shubnikov phase, has the ability to let magnetic flux penetrate the superconductor in quantized units of a flux quantum. By irradiation of the YBCO, a superconducting-to-insulating transition occurs that can be used to create artificial defects in the YBCO, allowing vortices

to prefer entering into these already existing defects, instead of trying to locally break up the superconductivity which is energetically unfavorable. With high resolution and a small spotsize, the HIM is the ultimate candidate to achieve unprecedented lattice spacing of the artificial array down to 20 nm. **Publications 3 and 4** describe the fabrication and characterization of these pinning arrays by helium ion irradiation with strong pinning and temperatures well below T_c , while for **publication 5**, the vortex Bose Glass phase of such pinning arrays is further analyzed. In **publication 6**, we optimized the fabrication process of such artificial pinning arrays in order to minimize the lattice constant of the artificial pinning arrays reaching the physical limit.

Chapter 2

Summary of publications and contributions

This chapter provides a summary for each of the 6 publications listed above which are covered in this thesis. Each summary is followed by a brief description of author contributions.

2.1 Josephson Junctions and SQUIDs

In publications 1 and 2, a focused helium ion beam is used to create JJs and SQUIDs in YBCO. While publication 1 focuses on junction properties directly after the irradiation, publication 2 takes this a step further and investigates the change in properties over time after the fabrication of these JJs when stored at room temperature and after annealing treatments under various environmental conditions.

2.1.1 Publication 1: Josephson Junctions and SQUIDs Created by Focused Helium-Ion-Beam Irradiation of $\text{YBa}_2\text{Cu}_3\text{O}_7$

Based on the preparatory work of Cybart et al. [41] in 2015, an in-depth study, including electrical as well as scanning transmission electron microscope (STEM) analysis, of JJs on various substrate materials with the described promising approach was performed. Publication 1 presents the results on He-FIB JJs and SQUIDs obtained in Tübingen.

YBCO thin films were prepared on three different single-crystal substrates (SrTiO_3 (STO), MgO , $(\text{LaAlO}_3)_{0.3}(\text{Sr}_2\text{TaAlO}_6)_{0.7}$ (LSAT)) by pulsed laser deposition (PLD) and junctions were patterned with an HIM with varying dose. Fig. 2.1(a) shows a schematic representation of

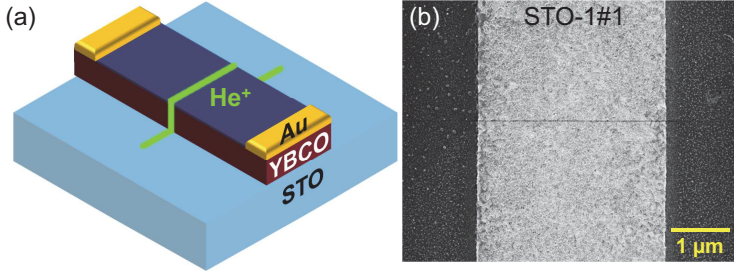


Figure 2.1: (a) Schematic illustration of the geometry and the fabrication process. (b) SEM image of a JJ, visible as a dark line due to carbon deposition. Figure from appended publication 1. Copyright © 2019 American Physical Society.

the irradiation process on the YBCO microbridge, while in Fig. 2.1(b), an SEM image of the irradiated microbridge reveals a dark line where the helium ion beam was scanned across the bridge and deposited carbon on the sample surface.

Resistance vs. temperature measurements as exemplified in Fig. 2.2 showed the existence of a threshold dose $D_{\text{th}} \gtrsim 1000$ ions/nm in a way that for higher doses, the irradiated linescan becomes resistive with no apparent supercurrent, while for lower doses, a supercurrent is still observable. A further increase in dose leads to resistances beyond $20 \text{ G}\Omega$, making the barrier highly resistive.

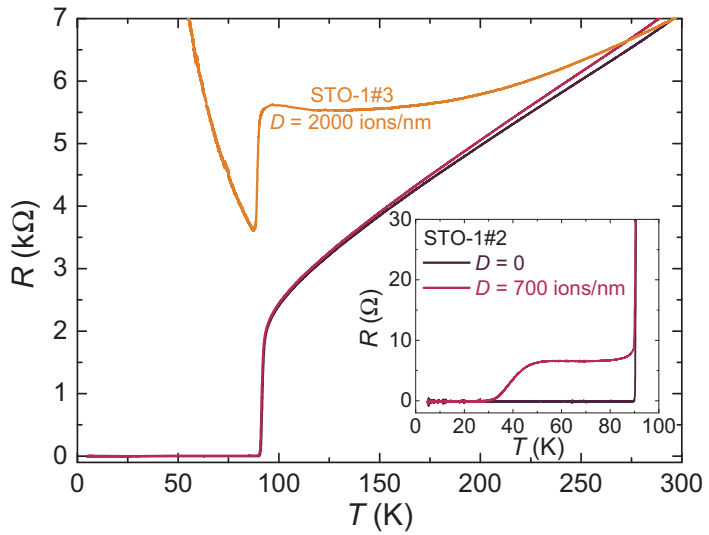


Figure 2.2: Resistance versus temperature measurement of a YBCO bridge before (black) and after irradiation with $D = 700$ ions/nm (red) and $D = 2000$ ions/nm (orange). Figure from appended publication 1. Copyright © 2019 American Physical Society.

STEM analysis of the irradiated linescans revealed an amorphous track for $D > D_{\text{th}}$ with increasing width for higher dose values. For $D < D_{\text{th}}$, however, there is no noticeable damage in the lattice structure of YBCO in the transmitted primary electron image captured by the STEM.

Further examination of the latter junctions with respect to the electronic transport properties revealed an exponential scaling of the critical current density $j_c \propto \exp(-D/D_0)$, the specific resistance ρ_n and the characteristic voltage $V_c = j_c \rho_n$ as shown in Fig. 2.3. For devices with $j_c \gtrsim 2 \text{ MA/cm}^2$, the Current Voltage Characteristics (IVCs) exhibit a flux-flow behavior, while the others can be approximately described within the resistively and capacitively shunted junction (RCSJ) model. From numerical simulations of the IVCs within this model, the Stewart-McCumber-Parameter β_c and the excess current density j_e was extracted. Below a critical current density of $j_c \approx 2 \times 10^5 \text{ A/cm}^2$, the devices did not exhibit any excess current. Furthermore, we were able to find a universal scaling for all He-FIB JJs of $V_c \propto j_c^{1/2}$, which has already been observed for other JJs in cuprate superconductors fabricated with a variety of different techniques.

As already stated, for high irradiation doses ($D > D_{\text{th}}$), the critical current density j_c can be fully suppressed. Using this approach, we fabricated a direct current (dc) SQUID with a nominally $300 \times 300 \text{ nm}^2$ normal conducting squared hole by irradiating this area with a dose of 4000 ions/nm^2 , and two JJs by irradiating with a linescan across the bridge over the already written hole with 230 ions/nm on an LSAT substrate. Characteristic voltage was determined to be $V_c = 414 \text{ } \mu\text{V}$, and

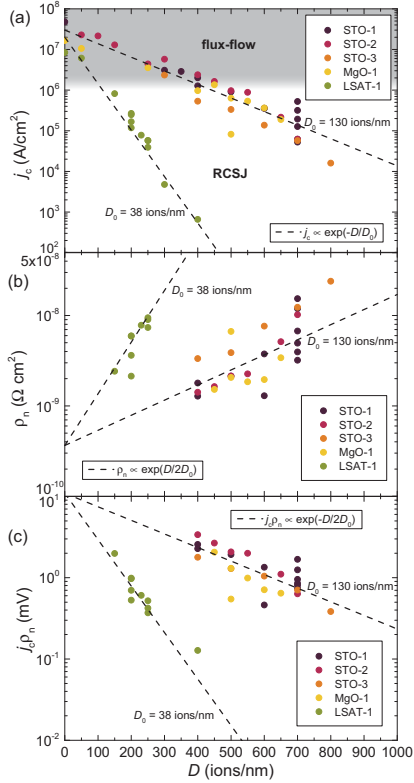


Figure 2.3: Dependence of device parameters (a) j_c , (b) ρ_n , and (c) $j_c \rho_n$ on line dose D for various samples on different substrates. The dashed lines indicate the exponential scaling behavior. Figure from appended publication 1. Copyright © 2019 American Physical Society.

a SQUID loop inductance of $L = 19$ pH could be extracted from simulations based on the RCSJ model. The SQUID could be operated in a bias point where a transfer function of $V_{\Phi} = 2.1$ mV/ Φ_0 could be achieved and measurements of the spectral density of flux noise S_{Φ} at this bias point revealed a frequency-dependent excess noise with roughly a $1/f$ -scaling, which is typical for YBCO SQUIDs due to I_c fluctuations in the JJs. The excess noise was still present at the upper bandwidth limit of the measurement setup. From this, we must conclude that the upper limit of the flux noise in the thermal white noise regime is given by $S_{\Phi}^{1/2} = 500$ n Φ_0 /Hz $^{1/2}$.

Contributions

This work was done in collaboration with the group of Applied Material Science and Electron Microscopy under supervisor C. J. Burkhardt at the NMI located in Reutlingen. Preparation of the STEM lamella was done by B. Schröppel and the STEM was operated by M. Becker for capturing the images. B. Müller adapted the fabrication process from Ref. [41], fabricated most of the samples and performed the characterization measurements at 4.2 K. I contributed by performing the irradiation and electrical characterization via $R(T)$ measurements of the high-dose samples and by assisting in the evaluation of the acquired STEM data, the sample fabrication and the 4.2 K measurements.

2.1.2 Publication 2: Temporal evolution of electric transport properties of $\text{YBa}_2\text{Cu}_3\text{O}_{7-\delta}$ Josephson junctions produced by focused helium- ion-beam irradiation

This publication is a direct sequel to publication 1. While publication 1 focuses on the properties of the fabricated devices directly after the irradiation process, this publication covers the temporal evolution with respect to the electrical transport properties within a year after the fabrication of JJs with an HIM when the samples are stored at room temperature. The acquired results are of high significance especially for applications where a SQUID is used as a magnetic field sensor, since these measurements must be reliable and the devices must be stable before a re-calibration is needed. The objective of this study was to qualitatively identify the aging of these junctions by characterizing the change in electric properties, e.g. the critical current density j_c versus time.

The starting point is comparable to publication 1; however, we focused on LSAT as the main substrate due to superior properties over other common substrate material, which results in YBCO thin films with a higher crystallinity, confirmed by X-ray diffraction (XRD) measurements. Figure 2.4 shows the modified layout with 7 close-spaced $3\ \mu\text{m}$ wide bridges used in this study.

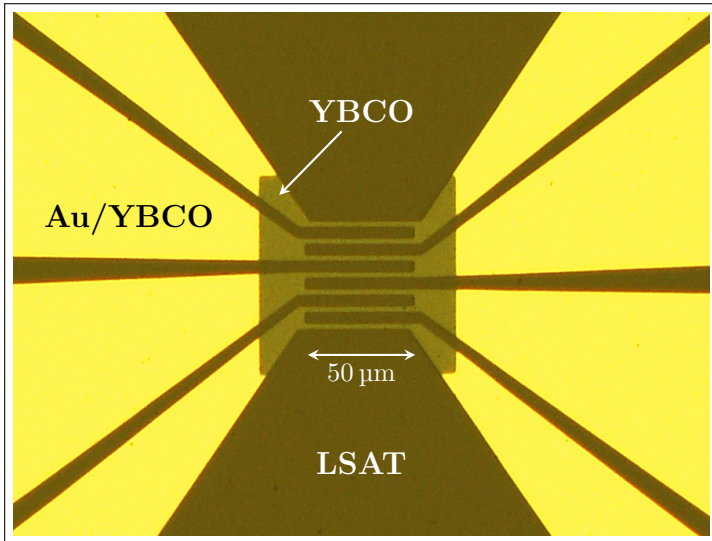


Figure 2.4: Optical microscope image of the central part of structure #2A with seven microbridges after prepatterning. Figure modified from appended publication 2. Copyright © 2024 American Physical Society.

We fabricated JJs through the He-FIB irradiation process described in publication 1 with doses ranging from 100 ions/nm to 1000 ions/nm, measured them directly after the irradiation at 4.2 K and stored them at room temperature under nitrogen (N_2) atmosphere. Subsequently and repeatedly, the junction properties at 4.2 K have been measured to see the temporal evolution. Over the whole dose range, the data can be best described by

$$j_c(t) = j_{c,\infty} \cdot \left[1 - b \cdot \exp\left(-\sqrt{\frac{t}{\tau}}\right) \right] , \quad (2.1)$$

with $j_{c,\infty}$ describing the equilibrium critical current density, b the reversible damage and τ a typical time scale of the relaxation process. This formula originates from a model where oxygen atoms diffuse back towards the barrier and partially restore the state before the irradiation. By fitting Eq. (2.1) to the corresponding data points of j_c vs. t for each junction, one can find the dose dependence of the fitting parameters as shown in Fig. 2.5. As established in publication 1, the critical current density j_c exponentially decreases with the dose D

$$j_{c,\infty}(D) \approx j_{c,\infty}(0) \exp(-D/D_0) , \quad (2.2)$$

with $j_{c,\infty}(0) = 3.2 \times 10^7$ A/cm² and $D_0 = 191.4$ ions/nm. Compared to the previous study, the value found for D_0 is higher and can be attributed to aging. Parameter b describes the degree of non-equilibrium created by the helium ion irradiation. For $b = 0$, there is nothing to recover because the equilibrium is already

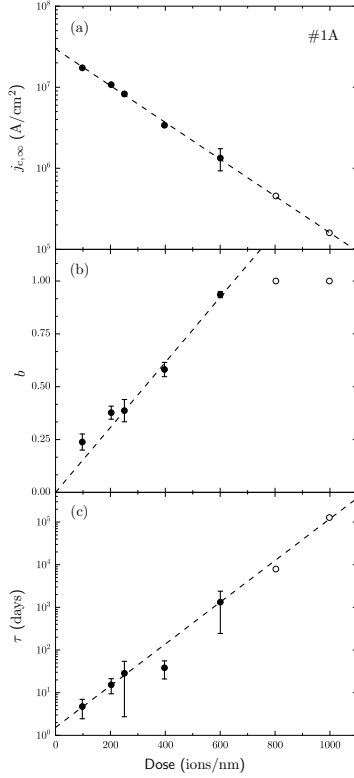


Figure 2.5: Dose dependence of the parameters $j_{c,\infty}$ (a), b (b) and τ (c) extracted from the fits with Eq. (2.1) to $j_c(t)$ data (not shown). The confidence intervals provided by the fitting algorithm are shown as error bars. Figure from appended publication 2. Copyright © 2024 American Physical Society.

reached, and for $b = 1$, the critical current density j_c is completely suppressed at $t = 0$ and approaches the final value $j_{c,\infty}$ for $t \rightarrow \infty$. From Fig. 2.5(b), we can see that b increases roughly linearly up to $D = 600$ ions/nm before it begins to saturate to $b = 1$. Taking a look at the time parameter τ , which describes on which timescale the evolution of the critical current density takes place, one can observe an exponential increase with the dose

$$\tau(D) \approx \tau_0 \exp(D/D_{0,\tau}) \quad , \quad (2.3)$$

with $\tau_0 = 1$ day and $D_{0,\tau} = 88.8$ ions/nm. An important conclusion is, that for junctions with RCSJ-like behavior without an excess current, i.e. $D \gtrsim 500$ ions/nm, the value of τ exceeds 100 days. That is to say that over several hundreds of days, these JJs will change their electric properties if stored at room temperature.

Using the normal resistivity ρ_n of a JJ, the characteristic voltage $V_c = j_c \cdot \rho_n$ can be calculated and is plotted against j_c , as shown in Fig. 2.6. Here we find an overall scaling of $V_c \propto j_c^{1/2}$, not only for different junctions with different doses as already stated in publication 1, but also for junctions measured several times after the irradiation and stored at room temperature. One difference holds true for the junction with $D = 1000$ ions/nm, showing a significant offset.

Furthermore, annealing was performed on another set of JJs after the irradiation to investigate the effects of increased temperature on the He induced barriers in YBCO. In general, the diffusion coefficient is temperature dependent, and therefore one should expect a significant effect on the JJs after a temperature

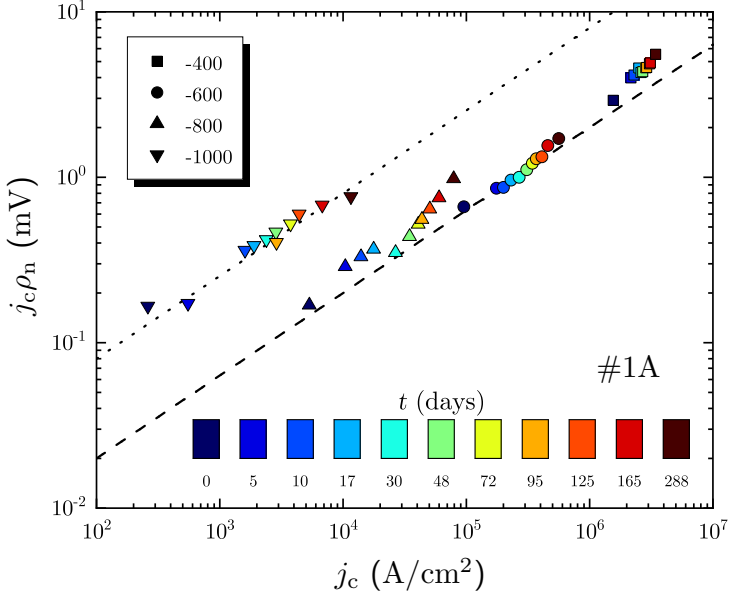


Figure 2.6: $j_c \rho_n$ vs j_c for He-FIB JJs (from #1A) stored at room temperature and measured at different times t after irradiation (indicated by the color scale). The dashed and dotted lines represent $j_c \rho_n = V_{c,1} \sqrt{j_c / j_{c,1}}$, with $V_{c,1} = 2 \text{ mV}$ and 8 mV , respectively ($j_{c,1} = 10^6 \text{ A}/\text{cm}^2$). Figure from appended publication 2. Copyright © 2024 American Physical Society.

treatment. Here, a temperature of 90°C where the samples were kept for 30 minutes and a partial oxygen pressure of 950 mbar was used. For this parameter set, we found that directly after the annealing step, the critical current density peaked, and that it dropped afterwards within one week to a stable value, which consecutive measurements confirmed as it is shown in Fig. 2.7. Repeating the annealing step for a second time, revealed the same overall behavior but with slightly increased decay time and (quasi-)equilibrium critical current densities.

Annealing was also performed at the same temperature as above, but this time while the sample stayed in an evacuated chamber. Interestingly, no qualitative difference between the samples annealed in pure oxygen and the ones annealed in vacuum could be observed. This indicates that the main contribution to the recovering of the damaged region must come from the oxygen atoms inside the YBCO displaced to other positions in the crystal lattice during irradiation.

Contributions

This work was realized within the physics department and Center for Quantum Science (CQ) and LISA⁺ at the University of Tübingen. I primarily planned the setup and execution of the experiments, grew, characterized and prepatterned the YBCO thin films, while K. Wurster supported in maintaining the PLD machine operational and the process parameters stable. K. Wurster and M. Meichsner assisted in the assembly of the annealing chamber and together with K. Wurster, I performed the intermediate annealing steps. The irradiation with the HIM and the electric

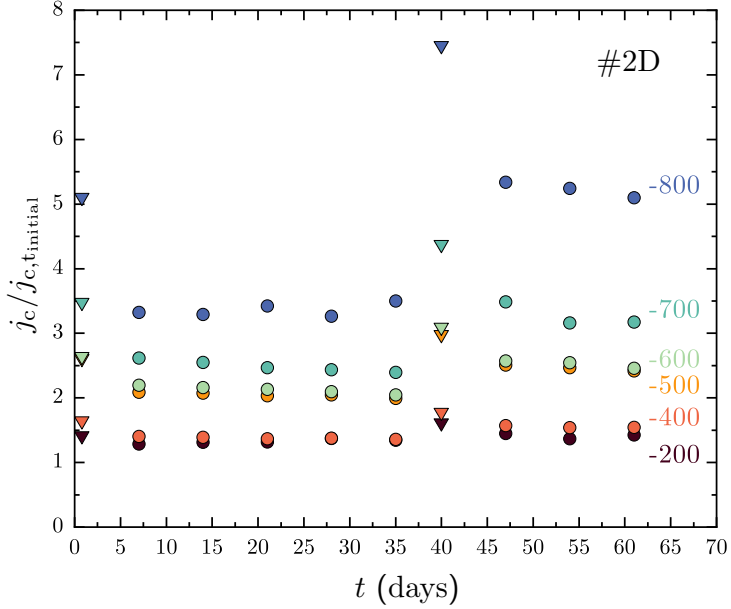


Figure 2.7: Temporal evolution of the critical current density j_c (normalized to j_c at $t = t_{\text{initial}}$) of He-FIB JJs from #2D, which were annealed at 90°C for 30 min in $p_{\text{O}_2} = 950$ mbar. Annealing was performed within one day after $t = t_{\text{initial}}$ for the first time and the second time at $t = 40$ days. Figure from appended publication 2. Copyright © 2024 American Physical Society.

transport measurements of the created samples were carried out by myself. In addition, I conducted the analysis and interpretation of the raw measurement data, with J. Linek assisting in the discussion of the results, and I wrote substantial parts of the manuscript.

2.2 Vortex pinning arrays

In publications 3 to 6, we investigated YBCO pinning arrays by irradiating different lattices with a focused helium ion beam. The high spatial resolution of the HIM allows for much denser arrays compared to conventional methods like masked ion-beam structuring (MIBS) and opens up new territories in the operation of magnetic flux-quantum-based devices. All of these publications were done in close collaboration with the group for Electronic Properties of Materials at the University of Vienna under supervision of Prof. Dr. Wolfgang Lang.

2.2.1 Publication 3:

Ultradense Tailored Vortex Pinning Arrays in Superconducting $\text{YBa}_2\text{Cu}_3\text{O}_{7-\delta}$ Thin Films Created by He Ion Beam Irradiation for Fluxonics Applications

The first part of this publication describes the irradiation process with the HIM to create pinning arrays in YBCO. The accelerated He ions of the beam collide with the atoms, interact with the sample and introduce defects into the lattice structure of YBCO. These defects, mainly the displaced oxygen atoms, lead to a local reduction or suppression of T_c , which can be controlled by the applied dose. The beam profile can be approximated by a gaussian distribution. Due to a lower acceleration voltage of 30 keV compared to dedicated ion implanters, the He ions still experience significant lateral straggling inside the 50 nm

to 80 nm thick sample, resulting in pinning centers of a conical shape instead of the desired cylindrical shape. An approach to minimize this effect is to intentionally widen the beam by adjusting the focal point with respect to the sample surface. Based on numerical simulations of ion-matter interactions and collision cascades, a beam diameter of 20 nm results in approximately 25 nm wide cylindrical defect channels (CDs) in a YBCO film, where T_c is reduced or suppressed up to a depth of 80 nm.

Two samples with quasi-kagomé (QK) pinning lattices have been irradiated with a dose of 15 000 ions/spot using an HIM as shown in Fig. 2.8. The QK lattice can be obtained by removing three neighboring sites from a hexagonal lattice. Sample QK90 has a nearest-neighbor distance of 90 nm and a YBCO film thickness of 75 nm, while for sample QK70, the lattice spacing was reduced to 70 nm at a film thickness of 50 nm.

The second part of this publication deals with the electric transport properties of the fabricated samples. Both samples exhibit pronounced vortex commensurability effects, i.e. maxima (matching peaks) in the critical current density $j_c(B)$ and minima in the magnetoresistivity $\rho(B)$ over a wide temperature range. For sample QK90, the first matching field is $B = 0.23$ T and $B = 0.38$ T for QK70 as shown in Fig. 2.9. Dominant interaction between vortices and the pinning potential of the CDs favors a very stable vortex arrangement (i.e., high j_c) at $B = B_6$, where each CD is filled with one vortex. Conversely, a strong vortex-vortex interaction will prefer a hexagonal configuration of the vortex ensemble with all CDs occupied and three interstitial vortices in the voids of the QK lattice, equivalent to matching field B_9 . However, a prominent matching peak appears at B_7

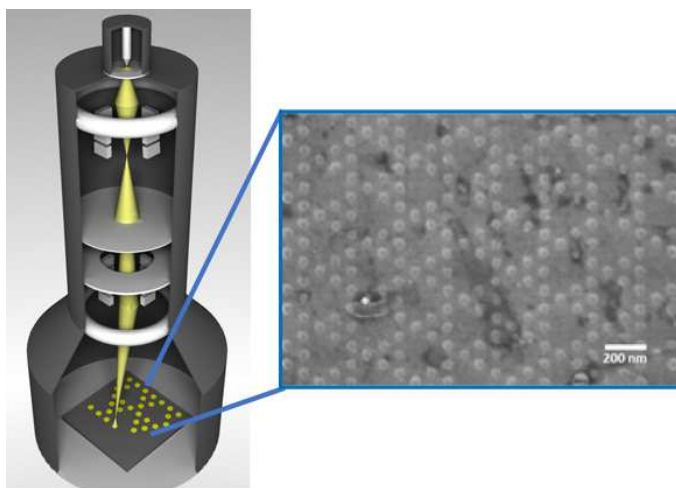


Figure 2.8: Schematic of the irradiation process with the HIM. The inset on the right shows a test pattern with the same QK lattice as sample QK90, but with a higher dose of 5×10^6 ions/spot for visualization. Figure from appended publication 3. Copyright © 2019 American Chemical Society.

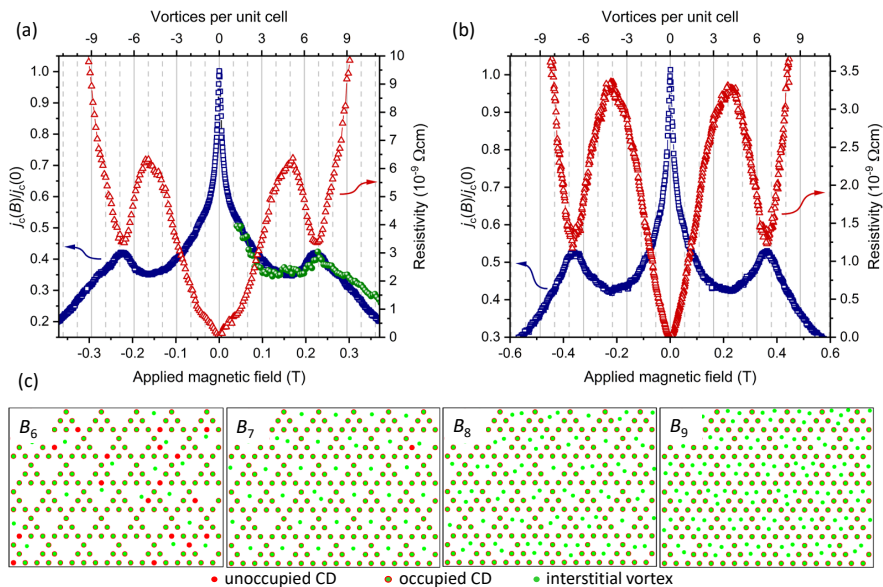


Figure 2.9: (a) Magnetic field dependence of the normalized critical current density at 83 K (blue squares) and resistivity at 83.5 K (red triangles) for sample QK90. The green dots represent the results from molecular dynamics simulations. (b) Magnetic field dependence of the normalized critical current density at 52 K (blue squares) and resistivity at 55 K (red triangles) for sample QK70. (c) Simulation of vortex distributions in QK90 for several applied magnetic fields corresponding to the matching fields B_6 to B_9 . Figure from appended publication 3. Copyright © 2019 American Chemical Society.

which can be seen in Fig. 2.9, corresponding to a fully occupied QK pinning array and one interstitial vortex in each unit cell. This observation can be confirmed by molecular dynamics simulations during which not only the vortex-vortex interaction and pinning force on the vortices at the CDs, but also an external driving force and a thermal stochastic force are taken into account. The vortex arrangements obtained by the simulation with the experimental conditions for sample QK90 and magnetic fields B_6 to B_9 are shown in Fig. 2.9(c). For B_6 , most of the pinning centers are occupied, but some interstitial vortices exist due to the strong repulsion between the vortices. These vortices are only weakly pinned and limit the critical current density. For B_7 , almost all pinning sites are occupied and typically one excess vortex sits in the centers of the voids of the QK lattice. This is an arrangement (vortex caging) that is favored by the repulsive vortex-vortex interaction, resulting in an increased j_c and thus matching features. By further increasing the magnetic field, all CDs are occupied and two (B_8) or three (B_9) interstitial vortices stay in the voids. Due to their repelling force on each other, they are very mobile, and thus j_c is reduced again. The simulation results are in good agreement with the experimental $j_c(B)$ measurement, as shown in Fig. 2.9(a).

By reducing the temperature, the balance between the pinning forces at the CDs and the vortex caging potential can be tuned. While both increase at lower temperatures, the pinning force at the artificial defects increases more rapidly. Therefore, one would expect that the vortex configuration prefers B_6 in order to minimize the energy.

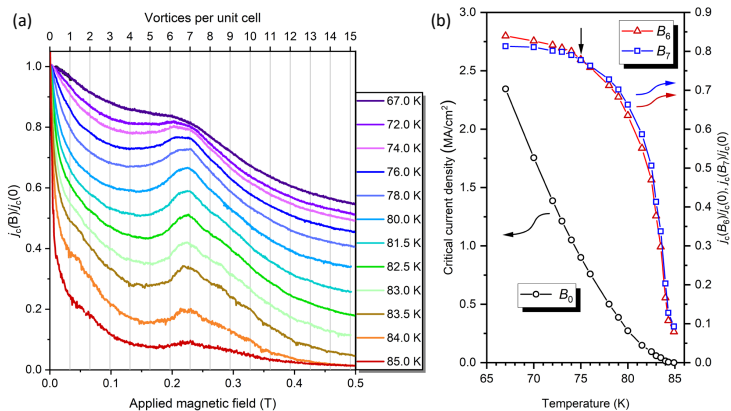


Figure 2.10: (a) Magnetic field dependence of the normalized critical current density of sample QK90 for different temperatures. (b) Temperature dependence of the critical current density without an applied magnetic field (black squares) and normalized critical current densities at matching fields B_6 (red triangles) and B_7 (blue squares). Figure from appended publication 3. Copyright © 2019 American Chemical Society.

Figure 2.10(a) displays the normalized critical current density $j_c(B)/j_c(0)$ measured at different temperatures of sample QK90 with visible matching features down to 67 K. At $T < 80$ K, a second peak at B_6 next to the B_7 peak can be observed. For temperatures below $T < 75$ K, the normalized critical current density at B_6 becomes larger than at B_7 , which is demonstrated in Fig. 2.10(b). This crossover reveals that the matching field with six vortices per unit cell becomes more efficient in pinning the vortices at lower temperatures, which is exactly the case when the vortex arrangement matches the artificial QK pinning array.

Contributions

This work was done in collaboration with the groups of W. Lang at the University of Vienna where the electric transport measurements and the simulations of the CDs were performed, V. R. Misko from the University of Antwerp and RIKEN and F. Nori from RIKEN who took care of the molecular dynamics simulations, and the group of J. Pedarnig at the Johannes Kepler University Linz, where the YBCO films were grown. B. Aichner and B. Müller developed the irradiation process for the HIM located at the University of Tübingen. B. Müller and I irradiated the YBCO thin-film samples and F. Limberger assisted in the irradiation. Additionally, I contributed by developing a process to visualize the pinning arrays within the HIM, acquired the corresponding images and supported in writing the manuscript.

2.2.2 Publication 4: Angular magnetic-field dependence of vortex matching in pinning lattices fab- ricated by focused or masked helium ion beam irradiation of superconducting $\text{YBa}_2\text{Cu}_3\text{O}_{7-\delta}$ thin films

This publication is a follow-up on publication 3, investigating in detail the dependence of matching effects if the applied magnetic field is tilted against the sample surface normal by an angle α and comparing the fabrication methods of the focused helium ion beam approach with a conventional approach using MIBS.

We fabricated two YBCO samples with square pinning arrays by two different methods of Helium ion irradiation. Sample SQ200 with a film thickness of 80 nm was irradiated with the process described in publication 3. A beam diameter of ~ 50 nm was used and a square lattice with 200 nm spacing and a dose of $\sim 51\,000$ ions/spot was written into the YBCO film, as shown in Fig. 2.11(a). The second square lattice sample SQ500 with a 500 nm spacing was patterned by MIBS as sketched in Fig. 2.11(b). In contrast to the irradiation process with the HIM, a collinear beam of 75 keV He ions and a Si stencil mask with holes 180 nm in diameter was used. Due to a larger acceleration voltage with the ion implanter a YBCO film thickness of 210 nm could be used. Both samples had $T_c \sim 90$ K after film growth with transition widths $\Delta T_c \sim 1$ K.

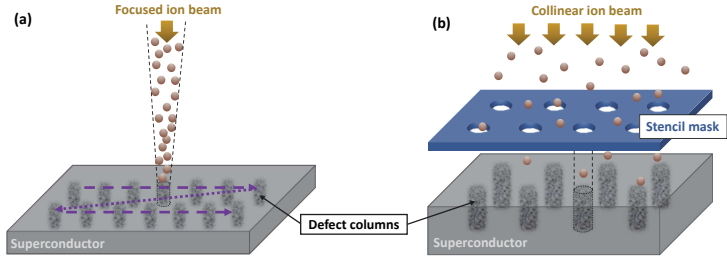


Figure 2.11: Schematic illustration of the irradiation process for (a) sample SQ200 using a HIM and (b) sample SQ500 using MIBS. Figure from appended publication 4. Copyright © 2020 Authors.

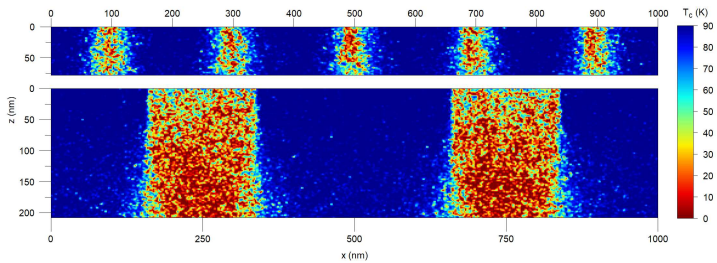


Figure 2.12: Cross-sectional view of the simulated T_c distributions for sample SQ200 (top panel) and sample SQ500 (bottom panel). Figure from appended publication 4. Copyright © 2020 Authors.

By utilizing the Stopping and Range of Ions in Matter (SRIM) application suite, the defect distributions of the two different irradiation methods of the pinning arrays can be simulated and are shown in Fig. 2.12. As stated by the simulations, both irradiation methods produce efficient pinning landscapes by creating clearly separated CDs with suppressed T_c . This can be also experimentally verified by their marginal impact on the zero-field electrical transport properties. Only a minor reduction of the critical temperature $\Delta T_c = 2.6$ K ($\Delta T_c = 4$ K) in sample SQ200 (SQ500) has been observed after the irradiation.

In electric transport measurements, both samples exhibit matching effects at the expected values of the applied magnetic field B_a and thereby demonstrate the validity of the different methods for the fabrication of pinning arrays.

For pronounced pinning at the artificial introduced pinning array, the magnetic flux should prefer the CDs irrespectively of the angle α between the applied magnetic field B_a and the symmetry axis of the CDs as sketched in the inset of Fig. 2.13. The matching peaks should then appear if the parallel component¹ of B_a fulfills the matching condition. As shown in Fig. 2.13, the measured $R(B_{\parallel})$ curves of sample SQ200 manifest matching effects at the same values of B_{\parallel} for angles up to 70° . Since the parallel component of the matching field is independent of the tilt angle α , the pinning at the CDs of the artificial pinning landscape is dominating the intrinsic pinning of vortices in the YBCO thin film. The same holds true for sample SQ500, which

¹ $B_{\parallel} = B_a \cos(\alpha)$

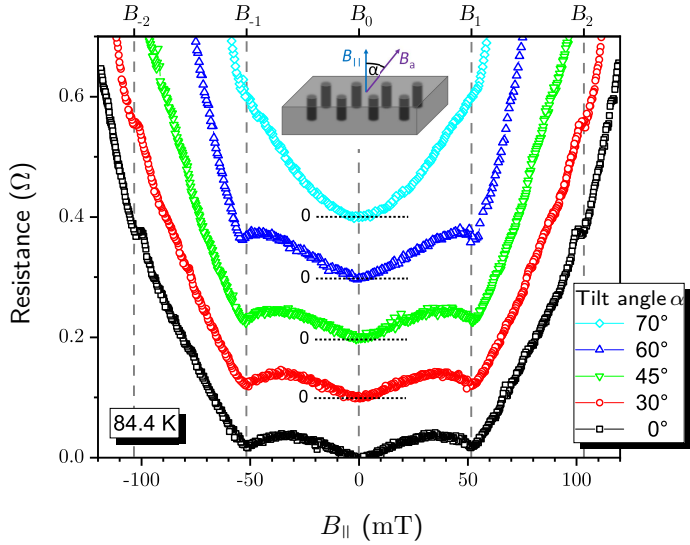


Figure 2.13: Resistance versus the parallel component of the applied magnetic field of sample SQ200 for different tilt angles shown in the inset. For $\alpha \neq 0$, an offset is applied for clarity. Figure modified from appended publication 4. Copyright © 2020 Authors.

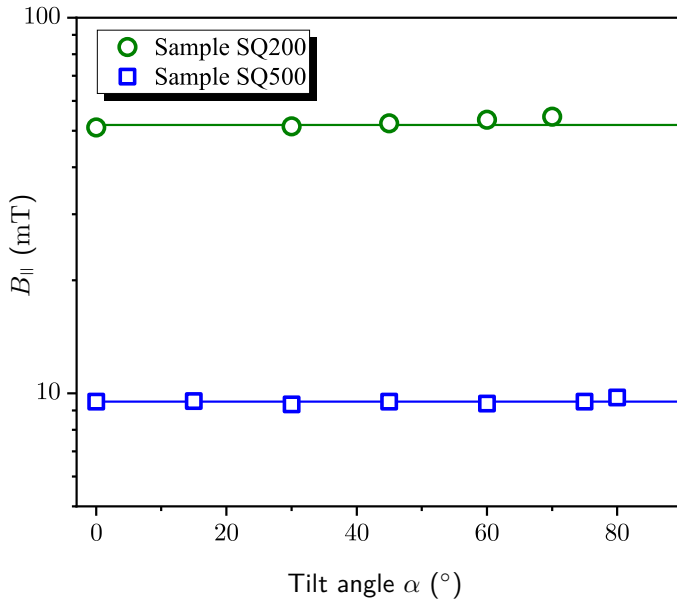


Figure 2.14: Angular dependencies of the parallel component of the first matching fields for samples SQ200 and SQ500. The horizontal lines indicate that the parallel component of the applied magnetic determines the matching peak, irrespective of the tilt angle α . Figure modified from appended publication 4. Copyright © 2020 Authors.

can be concluded from Fig. 2.14, where the angular dependence of the parallel component B_a for the first matching field B_1 is shown for both samples and within the margin of error constant with respect to the tilt angle α .

Contributions

This work was done in collaboration with the groups of W. Lang at the University of Vienna where the electric transport measurements and the simulations of the CDs were performed, and the group of J. Pedarnig at the Johannes Kepler University Linz, where the YBCO thin film was deposited and the MIBS irradiation was conducted. B. Aichner and B. Müller developed the irradiation process for the HIM located at the University of Tübingen. B. Müller irradiated the samples and I supported the fabrication process. Further, I assisted in writing of the manuscript.

2.2.3 Publication 5: **Ordered Bose Glass of Vortices in Superconducting $\text{YBa}_2\text{Cu}_3\text{O}_{7-\delta}$ Thin Films with a Periodic Pin Lattice Created by Focused Helium Ion Irradiation**

Different theories have been proposed for randomly distributed pinning defects, depending on their dimensionality. The vortex glass (VG) model for point-like defects and the Bose glass (BG) model for CDs penetrating the entire thickness of the sample.

With the developed HIM irradiation technique, established and improved in publications 3 and 6, it is possible to engineer and investigate periodic pinning sites in YBCO with spacings smaller than the London penetration depth and pronounced vortex pinning effects down to temperatures below the magnetic field dependent glass temperature $T_g(B)$, allowing for a novel kind of glass-vortex correlations which we call ordered Bose glass (OBG) and which are the subject of research within this publication by measuring the V - I isotherms at various temperatures and magnetic fields.

The nominal 30 nm thick YBCO sample film was prepared by PLD on LSAT substrate and irradiated by 30 keV He ions with a 30 nm triangular spot lattice, using a dose of 10^4 ions/spot. Figure 2.15(a) shows the temperature dependence of the resistance R of a patterned microbridge, as well as an unirradiated bridge for reference. The inset displays an optical microscopy image of the YBCO bridge taken after the irradiation. The critical temperature of the patterned microbridge dropped from 88.4 K to 76.0 K. A possible explanation is the scattering of a small portion of ions scattering and creating point defects between the CDs.

Figure 2.15(b) presents the pronounced commensurability effect for the critical current density $j_c(B)$ at 5 K and the resistance $R(B)$ at 72 K for an applied magnetic field perpendicular to the sample surface. Matching peaks occur at the expected magnetic field values for a 30 nm hexagonal lattice, confirming a successful fabrication process.

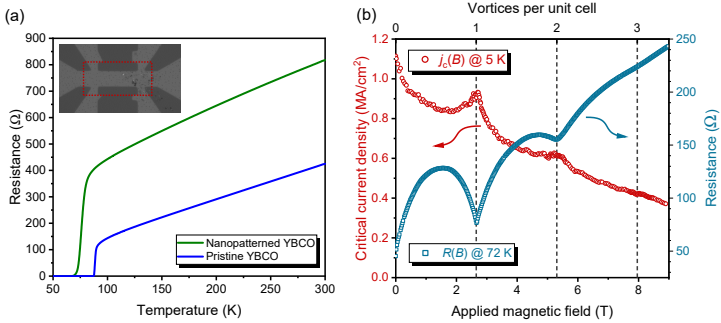


Figure 2.15: (a) Resistances of a YBCO thin film with a hexagonal array of 30-nm spaced columnar defects and an unirradiated reference bridge fabricated on the same substrate. Inset: Optical microscopy picture of the bridge taken after irradiation. The red dotted rectangle marks the irradiated area of $36 \times 16 \mu\text{m}^2$. (b) Critical current density at 5 K and resistance at 72 K of the irradiated bridge. The broken lines indicate the number of vortices per unit cell of the hexagonal CD lattice, corresponding to the matching fields $B_m = m \times 2.653 \text{ T}$. Figure from appended publication 5. Copyright © 2022 Authors.

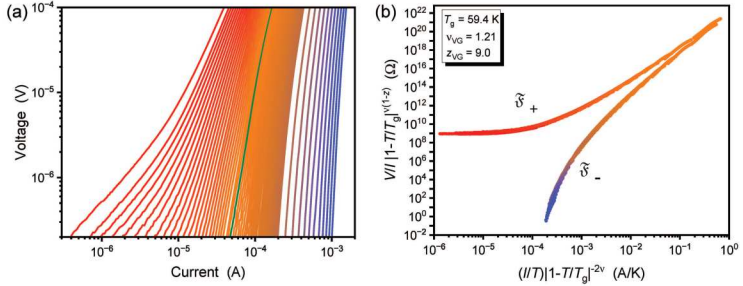


Figure 2.16: (a) V - I isotherms at 66 K (red), 65.5 K to 52 K in 0.25 K steps, and 50 K to 30 K (blue) in 2 K steps of the nanopatterned sample at the matching field $B_1 = 2.653$ T. The green line indicates the isotherm at 59.5 K, which is closest to the glass temperature $T_g = 59.4$ K. (b) V/I vs. I isotherms plotted according to the VG scaling. The isotherms collapse onto the two universal functions \mathfrak{F}_+ above and \mathfrak{F}_- below T_g , respectively. The colors of the data points represent the temperature and are the same as in panel (a). Figure from appended publication 5. Copyright © 2022 Authors.

The V - I characteristics were measured in static magnetic fields between 1.0 T to 8.0 T for temperatures in the vicinity of the glass temperature T_g . Measurement results for an applied magnetic field equal to the first matching field B_1 are shown in Fig. 2.16. Theory predicts a critical scaling of parameters for the continuous second-order phase transition between vortex or Bose glass and the vortex liquid, which can experimentally be accessed by the V - I isotherms. Applying the scaling theories, one can deduce

the graph shown in Fig. 2.16(b) resulting in qualitatively similar findings compared to previous work. However the dynamic parameter $z_{\text{VG}} = 9.0$ lies outside the reasonable range predicted by the VG theory.

An evaluation of the V - I isotherms for the complete range of applied magnetic fields reveals the systematic change of parameters as depicted in Fig. 2.17. While pristine YBCO shows a nearly linear decrease of T_g with increasing magnetic field, we can observe the same behavior as long as the applied magnetic field is not near a matching field. At the matching fields B_1 and B_2 , peaks in the phase boundary $T_g(B)$ are visible.

The scaling parameters v_{VG} and z_{VG} behave very differently with respect to each other. The value of $v_{\text{VG}} = 1.3$ is independent of the applied magnetic field within the range that has been reported for pristine YBCO. The dynamic parameter z_{VG} changes drastically with variable B , first increasing slowly up to $z_{\text{VG}} \approx 5.8$ until $B \approx 2.5$ T, followed by a narrow peak at the first matching field at B_1 with a maximum value of $z_{\text{VG}} = 9.0$, clearly outside the 3-dimensional VG scaling range. For fields above the peak at B_1 , it quickly relaxes to a value of $z_{\text{VG}} = 6.5$ for magnetic fields between 3 T to 8 T. At the second matching field, no distinct peak for $z_{\text{VG}}(B)$ is recognizable. Only a broader bump is showing up at B_2 , roughly being inside the margin of errors.

Converting the critical exponents to the ones of the BG theory, we found $v_{\text{BG}} = 0.81$ and $z_{\text{BG}} = 14$ at B_1 .

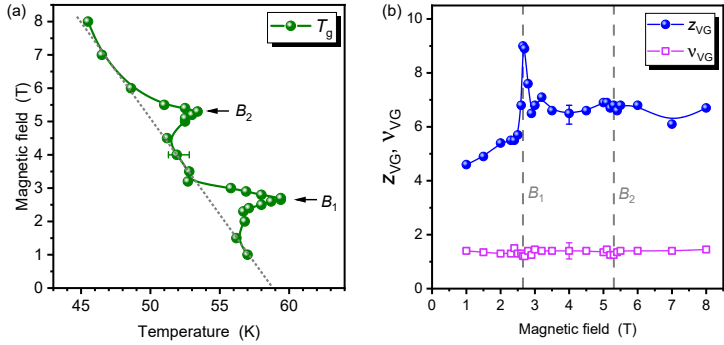


Figure 2.17: Scaling parameters of the nanopatterned YBCO film. The representative error bars indicate the uncertainty caused by interdependence between the fit parameters T_g , z_{VG} , and ν_{VG} . The size of the symbols represents the uncertainty of the parameter when the other two parameters are kept fixed. Solid lines are guides to the eye. (a) The phase boundary between the vortex liquid and the glass phase is represented by the glass temperature T_g as a function of the external magnetic field. The grey dotted line symbolizes a linear trend of T_g . (b) Parameters from the scaling analyses. Figure from appended publication 5. Copyright © 2022 Authors.

Contributions

This work was done in collaboration with the group of W. Lang at the University of Vienna. The electric transport measurements were performed by L. Backmeister, B. Aichner and W. Lang. K. Wurster grew the YBCO thin film, I prepatterned the film and performed the focused helium ion beam irradiation, L. Backmeister and W. Lang analyzed the transport data. As all of the authors, I contributed in discussion of the results and assisted in writing the manuscript.

2.2.4 Publication 6:

Vortex matching at 6 T in $\text{YBa}_2\text{Cu}_3\text{O}_{7-\delta}$ thin films by imprinting an ultradense hexagonal pinning array with a focused helium ion beam

In publication 3, artificial pinning arrays with commensurability effects up to 0.4 T were fabricated by using a focused helium ion beam setting a milestone in the manufacturing of sub-100 nm pinning landscapes. However, there was still an opportunity to further improve the process and dive deeper into the reduction of the lattice parameter a approaching new limits. This publication deals with the advanced fabrication and investigation of hexagonal pinning arrays in YBCO with matching effects up to 6 T with nearest-neighbor distances between artificial pinning sites down to 20 nm.

The first part describes the considerations taken into account for the optimization of the irradiation process used in publication 3. Main steps of the manufacturing process are depicted in Fig. 2.18. One important step is to use a reduced YBCO film thickness below 50 nm since the acceleration voltage of the commercially available HIM is limited to 30 keV, which will result in larger lateral spread inside the sample compared to higher acceleration voltages, realizable with available helium ion implanters as it was shown in publication 4. With a film thickness below this threshold, it is no longer necessary to intentionally widen the helium ion beam with the focusing lens in order to create CDs in the YBCO as previously done in publications 3 and 4. In this case, the HIM can be operated at optimal resolution for the fixed aperture settings. An essential tool for finding a suitable parameter range is the SRIM software simulation package, providing the collision trajectories and the ion damage to generate cross-sectional damage profiles of the CDs within the YBCO. For accurate and meaningful simulation results, the beam diameter needs to be known, which can be estimated with various methods. The simulation results for different pattern parameters are summarized in Fig. 2.19. From the simulations, one can find well-separated CDs with superconducting percolation paths in between for lattice spacings down to 20 nm. In contrast, for an array with $a = 15$ nm, the overlap of the CDs becomes more significant, thus reducing the contrast between regions with modified and pristine YBCO. Experimentally, we used STEM on a lamella, cut from a hexagonal lattice which was irradiated

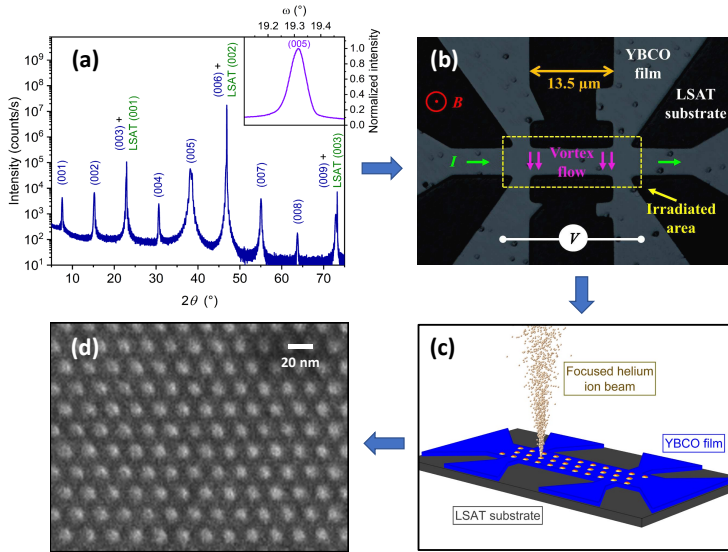


Figure 2.18: (a) XRD graph of the sample after PLD. (b) Optical microscope image of bridge H20. (c) Schematic of the patterning process inside the HIM. (d) Secondary electron image of a reference pattern with a hexagonal $a = 20$ nm lattice, irradiated with $D = 6 \times 10^4$ i/dot to visualize the pattern. The white spots is material blistered by the high irradiation dose. Figure from appended publication 6. Copyright © 2024

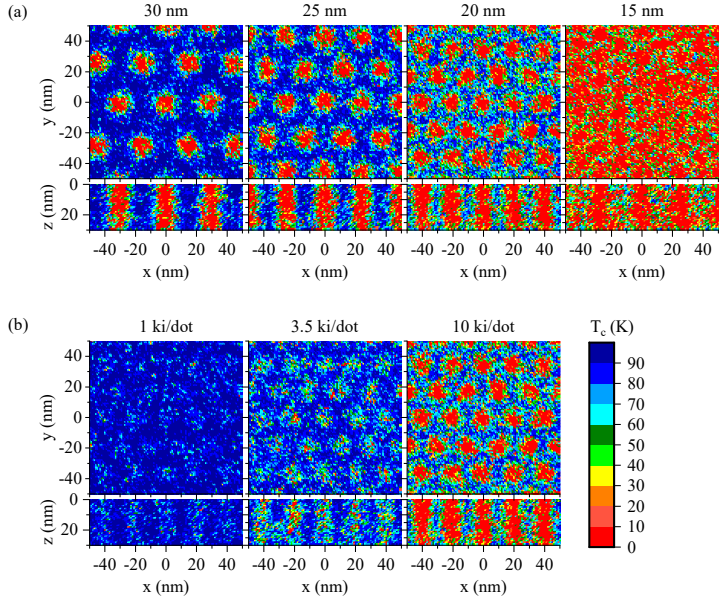


Figure 2.19: SRIM simulations of the damage profiles mapped to the corresponding T_c suppression for both important cross-sections. The x - y -plots show cuts at $z = 15$ nm and the x - z -plots cuts at $y = 0$. (a) Hexagonal lattices with different spacings of a 9 nm full width at half maximum (FWHM) He ion beam and a dose of 10^4 i/dot. (b) Hexagonal lattice with fixed $a = 20$ nm spacing and different doses. Figure from appended publication 6. Copyright © 2024

with a linear-scaled dose from 0.689 ki/dot to 80 ki/dot, to find, that for low doses, the YBCO crystal structure is preserved, while the amorphization becomes visible at the critical dose of $D_c \approx 13$ ki/dot.

The optimal irradiation parameters used, were as follows: Beam current was adjusted to 500 fA at Spot Control (SC)² equal to 5 and the dimensions of the irradiated area were fixed to fit inside a Field of View (FoV) of 30 μm , which not only kept the irradiation time within reasonable ranges, but also decreased beam precision errors which usually are proportional to different powers of the FoV, depending on their root cause within the electrostatic lens system in the ion beam column. As important as the choice of the SC setting is the choice of ions per pinning dot, for simplicity referred to as dose. Fig. 2.20 illustrates the differences between pinning arrays fabricated on the same substrate under equal conditions while varying SC and dose. While Fig. 2.20(a) shows the resistivity ρ dependency with applied magnetic field B for doses ranging from 1 ki/dot to 10 ki/dot, one can see, that although matching effects are starting to become visible at around 2 ki/dot, strong pinning with prominent matching dips at the first and second matching field occur only at 10 ki/dot, in accordance with our simulation results from Fig. 2.19. In Fig. 2.20(b) the resistivity $\rho(B)$ dependence is plotted for different values of SC, showing that for a lower setting,

²SC is a dimensionless setting (ranging from 1 to 10) which describes the distance of the virtual source to the beam aperture. Higher values reduce beam current but result in a narrower beam profile.

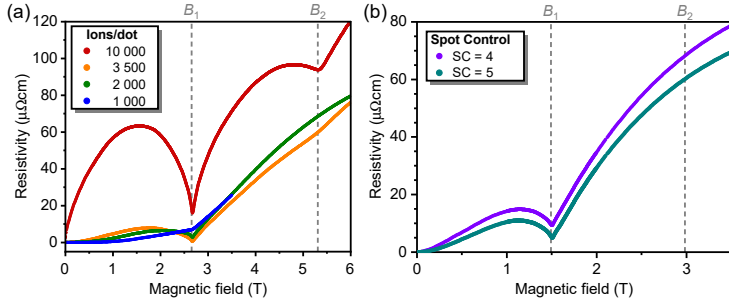


Figure 2.20: Vortex matching effects in the resistivity vs field curves of irradiated YBCO bridges. (a) Comparison of various doses ranging from 1 ki/dot to 10 ki/dot. Magneto-resistivity of four samples at $T/T_c \sim 0.96$ after irradiation with an $a = 30$ nm hexagonal pattern using SC = 4. (b) Comparison of different SC settings of the HIM with a fixed dose of $D = 3.5$ ki/dot. Two hexagonal pinning arrays with $a = 30$ nm were prepared on the same substrate. The magneto-resistivity at 86.5 K, corresponding to $T/T_c \sim 0.96$ is plotted for both SC settings used. Figure from appended publication 6. Copyright © 2024

thus larger beam diameter, the qualitative matching behavior is similar to the bridge irradiated with $SC = 5$, however, due to the larger spot size, and therefore a enlarged volume of defects, the resistivity is significantly increased.

The second part puts more focus on the electronic transport properties of the fabricated sample with nearest-neighbor distance of 20 nm. For our study, several hexagonal CD arrays with spacings from 30 nm to 15 nm and dose values from 10^3 ions/spot to 10^4 ions/spot were fabricated. In agreement with the simulations shown in Fig. 2.19, lattice spacings down to 20 nm lead to well separated CDs, maintaining zero-resistance transport characteristics, while sample H15 with $a = 15$ nm exhibits a semiconducting temperature dependence without any superconducting transitions above 2 K. This marks the resolution limit of the fabrication method due to the overlapping CDs, resulting in a complete suppression of the superconducting properties. Sample H20, with a 20 nm hexagonal pinning lattice, not only has a remaining transition into the superconducting state, but also clearly shows vortex matching effects in high magnetic fields at 6 T and over wide temperature ranging from 2 K to 60 K as shown in Fig. 2.21. For lower temperatures, the matching peak at $B_1 = 6$ T can be identified more easily in the inset of Fig. 2.21(a). In this graph, one can also make out that the peaks at higher temperature are more pronounced due to a faster decrease of the pinning force for intrinsic defects compared to that of the CDs. Previous work on this topic did not identify such a behavior, which indicates that this must be a natural consequence of ultradense and strong pinning sites produced by the irradiation with a helium ion beam.

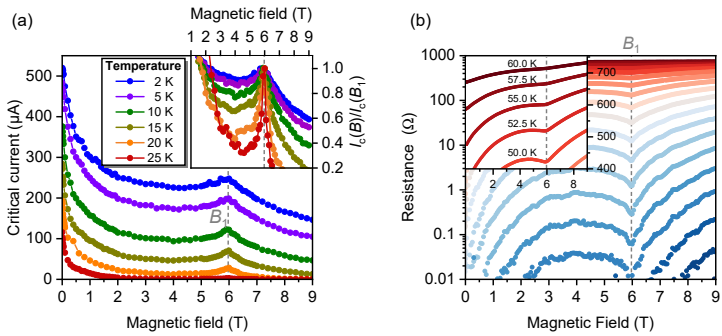


Figure 2.21: Vortex commensurability effects of sample H20 with a hexagonal $a = 20$ nm CD lattice. (a) Critical current versus applied magnetic field for temperatures ranging from 2 K to 25 K. The inset shows the same graph with critical currents normalized to the value at the first matching field B_1 . (b) Resistance versus applied magnetic field for temperatures from 17.5 K to 60 K in steps of 2.5 K. The inset shows a zoom-in on the first matching peak at higher temperatures. Figure from appended publication 6. Copyright © 2024

Contributions

This work was done in collaboration with the groups of W. Lang at the University of Vienna, where the electric transport measurements and the simulations of the CDs were performed by B. Aichner and B. Budinská. STEM lamella preparation and examination was conducted by C. Magén in the Instituto de Nanociencia y Materiales de Aragón at CSIC-Universidad de Zaragoza on samples that were provided by C. Schmid and R. Hutt. K. Wurster grew the YBCO thin film, I characterized and prepatterned the thin film used for the transport experiments conducted at Vienna. Furthermore, I worked on improving the irradiation and visualization process with the HIM and irradiated the samples for the electric transport measurements and assisted in writing of the manuscript.

Chapter 3

Conclusion and outlook

As the first part of this thesis, JJs and SQUIDs based on the high-transition temperature cuprate superconductor $\text{YBa}_2\text{Cu}_3\text{O}_{7-\delta}$ have been successfully fabricated by using a helium ion microscope. Electric transport measurements were conducted to investigate the physical properties of the created devices directly after the irradiation process and to assess how they evolve with time when stored under nitrogen atmosphere at room temperature. The presented fabrication technique is highly versatile and straightforward with respect to the needed process steps compared to state-of-the-art GBJJs. It enables, for instance, the placement of a magnetic nanoparticle on the prepatterned mi-

crostrip in advance of writing the SQUID, thus lowering demands on the positioning of the nanoparticle with micro manipulators by leveraging the precision of the helium ion microscope. Whereas, this thesis has only laid the foundation for such He-FIB devices, this technique opens a path towards more sophisticated devices like geometric π Josephson Junctions [44] or Bi-SQUIDs [45], which can, in contrast to using other methods, be more easily realized with this approach. However, due to the novelty of both material and tool combination, observed effects are not always completely understood, but require and invite for further research.

In the second part of this thesis, the appealing physics of vortex pinning arrays was investigated. With the same approach as above, local cylindrical defect channels with regular patterns, e.g quadratic and quasi-kagomé, were engineered and fabricated in $\text{YBa}_2\text{Cu}_3\text{O}_{7-\delta}$ with spacings down to 70 nm by irradiation with an intentionally defocused beam of a helium ion microscope. The samples exhibited strong matching effects with temperatures far below the critical temperature of the thin films, overcoming the uncorrelated pinning sites from impurities and other crystal defects. For the quasi-kagomé lattice, an unconventional commensurability effect of magnetically caged interstitial vortices, as well as the competition between the artificial pinning landscape and the repelling vortex-vortex interaction could be observed by measurements conducted at variable temperature. Through measurements with an oblique applied magnetic field, it was confirmed that the matching features solely depend on the component parallel to the defect columns of the magnetic field, which confirms that the magnetic flux is penetrated along

the artificial cylindrical defect channels. Further optimization resulted in a reduction in nearest neighbor distance to 30 nm in a hexagonal pinning array, allowing for the observation of an ordered Bose glass, marked by a characteristic scaling of the voltage-current isotherms. Ultimately, a hexagonal pinning lattice with a spacing of 20 nm was realized, with outstanding commensurability effects of 6 T.

So far, in the publications presented above, it is only in two fields, namely JJs and pinning arrays, that we have laid the groundwork for this promising technology to develop its full potential in the future. Thus, where we have only scratched the surface of focused helium ion beam irradiated $\text{YBa}_2\text{Cu}_3\text{O}_{7-\delta}$ so far, it is now time to take a look underneath and reveal more of its intriguing physics.

List of acronyms

dc direct current

YBCO $\text{YBa}_2\text{Cu}_3\text{O}_{7-\delta}$

N₂ nitrogen

HIM helium ion microscope

NIM neon ion microscope

GFIS gas field ion source

SQUID superconducting quantum interference device

SEM scanning electron microscope

STEM scanning transmission electron microscope

Ga-FIB gallium focused ion beam

He-FIB helium focused ion beam

FIB focused ion beam

SIMS secondary ion mass spectroscopy

GL Ginzburg-Landau

GB grain boundary

JJ Josephson Junction

RCSJ resistively and capacitively shunted junction

CD cylindrical defect channel

QK quasi-kagomé

MIBS masked ion-beam structuring

SRIM Stopping and Range of Ions in Matter

IVC Current Voltage Characteristic

MRI magnetic resonance imaging

MEG magnetoencephalography

SSM scanning SQUID microscope

SC Spot Control

FoV Field of View

PLD pulsed laser deposition

XRD X-ray diffraction

FWHM full width at half maximum

VG vortex glass

BG Bose glass

OBG ordered Bose glass

LSAT $(\text{LaAlO}_3)_{0.3}(\text{Sr}_2\text{TaAlO}_6)_{0.7}$

NASA National Aeronautics and Space Administration

BSCCO $\text{Bi}_2\text{Sr}_2\text{CaCu}_2\text{O}_{8+x}$

STO SrTiO_3

Bibliography

- [1] R. Egerton, P. Li, and M. Malac, *Micron* **35**, 399 (2004).
- [2] J. A. Notte, *Microscopy Today* **20**, 16 (2012).
- [3] B. W. Ward, J. A. Notte, and N. P. Economou, *Journal of Vacuum Science & Technology B: Microelectronics and Nanometer Structures* **24**, 2871 (2006).
- [4] M. T. Postek, A. E. Vladar, J. Kramar, L. A. Stern, J. Notte, and S. McVey, *AIP Conference Proceedings* **931**, 161 (2007).
- [5] J. Notte, B. Ward, N. Economou, R. Hill, R. Percival, L. Farkas, and S. McVey, *AIP Conference Proceedings* **931**, 489 (2007).
- [6] D. C. Bell, *Microscopy and Microanalysis* **15**, 147 (2009).
- [7] O. S. Ovchinnikova, N. Borodinov, A. A. Trofimov, S. T. King, M. Lorenz, W. Lamberti, D. Abmayr, and A. V. Ievlev, *ACS Applied Polymer Materials* **3**, 3478 (2021).

- [8] M. S. Joens, C. Huynh, J. M. Kasuboski, D. Ferranti, Y. J. Sigal, F. Zeitvogel, M. Obst, C. J. Burkhardt, K. P. Curran, S. H. Chalasani, L. A. Stern, B. Goetze, and J. A. J. Fitzpatrick, *Scientific Reports* **3**, 3514 (2013).
- [9] A. Williams, G. H. Kwei, R. B. V. Dreele, I. D. Raistrick, and D. L. Bish, *Physical Review B* **37**, 7960 (1988).
- [10] J. C. Slater, *The Journal of Chemical Physics* **41**, 3199 (1964).
- [11] Y. Suyama, M. Matsumoto, S. Kageyama, and I. Sato, in *Advances in superconductivity III*, edited by K. Kajimura and H. Hayakawa (1991), pp. 391–394.
- [12] J. M. Tranquada, A. H. Moudden, A. I. Goldman, P. Zolliker, D. E. Cox, G. Shirane, S. K. Sinha, D. Vaknin, D. C. Johnston, M. S. Alvarez, A. J. Jacobson, J. T. Lewandowski, and J. M. Newsam, *Physical Review B* **38**, 2477 (1988).
- [13] J. Bardeen, L. N. Cooper, and J. R. Schrieffer, *Physical Review* **108**, 1175 (1957).
- [14] W. Meissner and R. Ochsenfeld, *Die Naturwissenschaften* **21**, 787 (1933).
- [15] L. V. Shubnikov, V. I. Khotkevich, Y. D. Shepelev, and Y. N. Ryabinin, *Zh. Eksp. Teor. Fiz.* **7**, 221 (1937).
- [16] V. L. Ginzburg and L. D. Landau, *Zh. Eksp. Teor. Fiz.* **20**, 1064 (1950).
- [17] A. A. Abrikosov, *Zh. Eksp. Teor. Fiz.* **32**, 1442 (1957).

- [18] J. R. Clem, *Journal of Low Temperature Physics* **18**, 427 (1975).
- [19] E. H. Brandt, *Reports on Progress in Physics* **58**, 1465 (1995).
- [20] B. D. Josephson, *Physics Letters* **1**, 251 (1962).
- [21] R. Kleiner, D. Koelle, F. Ludwig, and J. Clarke, *Proceedings of the IEEE* **92**, 1534 (2004).
- [22] M. Paulsen, J. Lindner, B. Klemke, J. Beyer, M. Fechner, D. Meier, and K. Kiefer, *Review of Scientific Instruments* **94**, 103904 (2023).
- [23] C. W. F. Everitt et al., *Classical and Quantum Gravity* **32**, 224001 (2015).
- [24] Q. Guo, C. Ma, X. Zhang, Y. Xu, M. Fan, P. Yu, T. Hu, Y. Chang, and X. Yang, *Concepts in Magnetic Resonance Part B, Magnetic Resonance Engineering* **2020**, edited by L. G. Hanson, 1 (2020).
- [25] S.-J. Lee, K. Jeong, J. H. Shim, H. J. Lee, S. Min, H. Chae, S. K. Namgoong, and K. Kim, *Scientific Reports* **9**, 12422 (2019).
- [26] J. Clarke, M. Hatridge, and M. Mößle, *Annual Review of Biomedical Engineering* **9**, 389 (2007).
- [27] P. Lafarge, P. Joyez, D. Esteve, C. Urbina, and M. H. Devoret, *Nature* **365**, 422 (1993).
- [28] J. E. Mooij, T. P. Orlando, L. Levitov, L. Tian, C. H. van der Wal, and S. Lloyd, *Science* **285**, 1036 (1999).

- [29] A. J. Berkley, H. Xu, R. C. Ramos, M. A. Gubrud, F. W. Strauch, P. R. Johnson, J. R. Anderson, A. J. Dragt, C. J. Lobb, and F. C. Wellstood, *Science* **300**, 1548 (2003).
- [30] V. T. Dang, H. T. Huy, S. Miyajima, H. Matsumoto, H. Miyoshi, T. Okamoto, T. Ishida, M. Maezawa, and M. Hidaka, in 15th international superconductive electronics conference (ISEC) (July 2015).
- [31] J. R. Kirtley, L. Paulius, A. J. Rosenberg, J. C. Palmstrom, C. M. Holland, E. M. Spanton, D. Schiessl, C. L. Jermain, J. Gibbons, Y.-K.-K. Fung, M. E. Huber, D. C. Ralph, M. B. Ketchen, G. W. Gibson, and K. A. Moler, *Review of Scientific Instruments* **87**, 093702 (2016).
- [32] L. Knauss, A. Cawthorne, N. Lettsome, S. Kelly, S. Chattraphorn, E. Fleet, F. Wellstood, and W. Vanderlinde, *Microelectronics Reliability* **41**, 1211 (2001).
- [33] FIBsuperProbes, <https://www.fibsuperprobes.com/> (2020).
- [34] J. L. Smith, J. S. Brooks, C. M. Fowler, B. L. Freeman, J. D. Goettee, W. L. Hults, J. C. King, P. M. Mankiewich, E. I. D. Obaldia, M. L. O'Malley, D. G. Rickel, and W. J. Skocpol, *Journal of Superconductivity* **7**, 269 (1994).
- [35] H. Hilgenkamp and J. Mannhart, *Rev. Mod. Phys.* **74**, 485 (2002).
- [36] W. E. Booij, A. J. Pauza, E. J. Tarte, D. F. Moore, and M. G. Blamire, *Physical Review B* **55**, 14600 (1997).
- [37] S. K. Tolpygo, S. Shokhor, B. Nadgorny, J.-Y. Lin, M. Gurvitch, A. Bourdillon, S. Y. Hou, and J. M. Phillips, *Applied Physics Letters* **63**, 1696 (1993).

- [38] N. Bergeal, J. Lesueur, M. Sirena, G. Faini, M. Aprili, J. P. Contour, and B. Leridon, *Journal of Applied Physics* **102**, 083903 (2007).
- [39] F. Kahlmann, A. Engelhardt, J. Schubert, W. Zander, C. Buchal, and J. Hollkott, *Applied Physics Letters* **73**, 2354 (1998).
- [40] D.-J. Kang, G. Burnell, S. J. Lloyd, R. S. Speaks, N. H. Peng, C. Jeynes, R. Webb, J. H. Yun, S. H. Moon, B. Oh, E. J. Tarte, D. F. Moore, and M. G. Blamire, *Applied Physics Letters* **80**, 814 (2002).
- [41] S. A. Cybart, E. Y. Cho, T. J. Wong, B. H. Wehlin, M. K. Ma, C. Huynh, and R. C. Dynes, *Nature Nanotechnology* **10**, 598 (2015).
- [42] Y.-T. Wang, J. C. LeFebvre, E. Y. Cho, S. J. McCoy, H. Li, G. Gu, K. Kadowaki, and S. A. Cybart, *IEEE Transactions on Applied Superconductivity* **31**, 1 (2021).
- [43] L. Kasaei, T. Melbourne, V. Manichev, L. C. Feldman, T. Gustafsson, K. Chen, X. X. Xi, and B. A. Davidson, *AIP Advances* **8**, 075020 (2018).
- [44] A. Gumann, C. Iniotakis, and N. Schopohl, *Applied Physics Letters* **91**, 192502 (2007).
- [45] V. K. Kornev, N. V. Kolotinskiy, and O. A. Mukhanov, *Superconductor Science and Technology* **33**, 113001 (2020).
- [46] B. Müller, M. Karrer, F. Limberger, M. Becker, B. Schröppel, C. J. Burkhardt, R. Kleiner, E. Goldobin, and D. Koelle, *Physical Review Applied* **11**, 044082 (2019).

- [47] M. Karrer, K. Wurster, J. Linek, M. Meichsner, R. Kleiner, E. Goldobin, and D. Koelle, *Physical Review Applied* **21**, 014065 (2024).
- [48] B. Aichner, B. Müller, M. Karrer, V. R. Misko, F. Limberger, K. L. Mletschnig, M. Dosmailov, J. D. Pedarnig, F. Nori, R. Kleiner, D. Koelle, and W. Lang, *ACS Applied Nano Materials* **2**, 5108 (2019).
- [49] B. Aichner, K. L. Mletschnig, B. Müller, M. Karrer, M. Dosmailov, J. D. Pedarnig, R. Kleiner, D. Koelle, and W. Lang, *Low Temperature Physics* **46**, 331 (2020).
- [50] L. Backmeister, B. Aichner, M. Karrer, K. Wurster, R. Kleiner, E. Goldobin, D. Koelle, and W. Lang, *Nanomaterials* **12**, 3491 (2022).
- [51] M. Karrer, B. Aichner, K. Wurster, C. Magén, C. Schmid, R. Hutt, B. Budinská, O. V. Dobrovolskiy, R. Kleiner, W. Lang, E. Goldobin, and D. Koelle, *Physical Review Applied* **22**, 014043 (2024).

Appended publications

Publication 1

Reprinted with permission from
B. Müller et al., *Physical Review Applied* **11**, 044082 (2019)
Copyright © 2019 by the American Physical Society.

Josephson Junctions and SQUIDs Created by Focused Helium-Ion-Beam Irradiation of $\text{YBa}_2\text{Cu}_3\text{O}_7$

B. Müller,^{1,*} M. Karrer,¹ F. Limberger,¹ M. Becker,^{1,2} B. Schröppel,² C.J. Burkhardt,² R. Kleiner,¹ E. Goldobin,¹ and D. Koelle¹

¹Physikalisches Institut – Experimentalphysik II and Center for Quantum Science (CQ) in LISA⁺, University of Tübingen, Auf der Morgenstelle 14, Tübingen 72076, Germany

²NMI Natural and Medical Sciences Institute at the University of Tübingen, Markwiesenstraße 55, Reutlingen 72770, Germany

 (Received 25 January 2019; published 25 April 2019)

By scanning with a 30-keV focused He ion beam (He-FIB) across $\text{YBa}_2\text{Cu}_3\text{O}_7$ (YBCO) thin-film microbridges, we create Josephson barriers with critical current density j_c adjustable by irradiation dose D . The dependence $j_c(D)$ yields an exponential decay. At 4.2 K, a transition from flux-flow to Josephson behavior occurs when j_c decreases below approximately 2 MA/cm². The Josephson junctions exhibit current-voltage characteristics (IVCs) that are well described by the resistively and capacitively shunted junction model, without excess current for characteristic voltages $V_c \lesssim 1$ mV. Devices on MgO and LSAT substrates show nonhysteretic IVCs, while devices on SrTiO₃ show a small hysteresis. For all junctions, an approximate scaling $V_c \propto j_c^{1/2}$ is found. He-FIB irradiation with a high dose produces barriers with $j_c = 0$ and high resistances of 10 k Ω to 1 G Ω . This provides the possibility to write highly resistive walls or areas into YBCO using a He-FIB. Transmission electron microscopy reveals an amorphous phase within the walls, whereas for lower doses the YBCO stays crystalline. We have also “drawn” superconducting quantum-interference devices (SQUIDs) by using a He-FIB for the definition of the SQUID hole and the junctions. The SQUIDs show high performance, with flux noise < 500 n Φ_0 /Hz^{1/2} in the thermal white-noise limit for a device with 19 pH inductance.

DOI: [10.1103/PhysRevApplied.11.044082](https://doi.org/10.1103/PhysRevApplied.11.044082)

I. INTRODUCTION

Josephson junctions (JJs), i.e., weak links between two superconducting electrodes [1], are key elements in superconducting electronic circuits and are used both for basic studies of superconductivity and for many applications [2,3]. For conventional metallic superconductors, a mature trilayer thin-film technology based on Nb electrodes, separated by insulating or normal conducting barriers, has been well established for decades. This technology offers fabrication of JJs on a wafer scale with a small spread of characteristic parameters, such as critical current density j_0 and normal resistance times area ρ_n , even with lateral JJ size well below 1 μm [4,5].

For the high-transition temperature (high- T_c) cuprate superconductors, JJ technology is much less mature. Because of the complex nature of these materials, and in particular their small coherence length associated with strong sensitivity to defects on the atomic scale, a reliable trilayer JJ technology does not exist so far. On the other hand, the peculiar properties of cuprate superconductors,

such as high T_c , large upper critical field, large energy gap, and d -wave symmetry of the superconducting order parameter, can provide major advantages, if JJ devices and circuits can be realized with sufficient control over JJ parameters. Promising examples are, e.g., in the field of terahertz generation [6], self-biased rapid single flux quantum circuits [7], or magnetometry based on superconducting quantum-interference devices (SQUIDs) [8,9].

Apart from intrinsic JJs in stacks of $\text{Bi}_2\text{Sr}_2\text{CaCu}_2\text{O}_{8+\delta}$ single crystals, used for terahertz generation [6], most developed cuprate JJs are based on epitaxially grown $\text{YBa}_2\text{Cu}_3\text{O}_{7-\delta}$ (YBCO) thin films with $T_c \approx 90$ K that also offer operation with cryocoolers or liquid nitrogen; a large variety of JJ types have been developed and their properties have been investigated [10–13].

Until recently, the most reliable, simple, and most frequently used high- T_c JJs have been YBCO grain-boundary (GB) JJs [11]. They are usually fabricated by the epitaxial growth of YBCO films on (rather expensive) bicrystal substrates from only a few materials. The GBJJs can be placed only along the single GB line, which not only imposes topological limitations, but also limits the complexity of feasible circuits. The more advanced biepitaxial

*benedikt.mueller@uni-tuebingen.de

technique allows one to fabricate so-called tilt-twist GBs [12]. Such GBJJs can be distributed all over the chip and one can even fabricate $0-\pi$ JJs [14]. Still, GBJJs suffer from hardly controllable inhomogeneity along the GB line, which makes the properties of the JJs not very reproducible and causes a substantial spread in JJ parameters. Alternative approaches to create Josephson barriers in cuprates are based on local irradiation of thin films with a high-energy focused electron beam [15–18] or on irradiation with high-energy ions (protons [18], neon [19,20], oxygen [21,22]) through a lithographically defined mask with a nanogap. The local irradiation drives the material from the superconducting to the normal conducting or even insulating state. So far, this approach has been hampered by the fact that it was not possible to create ultrathin Josephson barriers that would provide JJs with high characteristic voltage $V_c = j_0 \rho_n$ and current-voltage characteristics (IVCs) without excess current that are well described by the resistively and capacitively shunted junction (RCSJ) model [23,24]. This is an important prerequisite for many applications. For reviews on various approaches to modify the properties of cuprate superconductors by local irradiation, see, e.g., Refs. [25,26] and references therein.

With the recent development of helium ion microscopy (HIM) [27], a sharply focused He ion beam with an approximately 0.5-nm diameter can be used to irradiate and modify cuprate superconductors on the nanoscale. This approach has been successfully used by Cybart and co-workers to fabricate JJs using focused helium-ion-beam (He-FIB) irradiation of YBCO thin films, and they demonstrated that the barriers in such He-FIB JJs can be changed continuously from conducting to insulating by varying the irradiation dose [28]. Moreover, the same group demonstrated already the integration of He-FIB JJs into SQUID devices [29], and the feasibility to use high-dose irradiation for nanoscale patterning (without removing material) in YBCO devices [30,31]. For a short review on this approach, also including irradiation with a focused Ne ion beam, see Ref. [32]. First attempts to extend this technique to the fabrication of JJs in other cuprate materials have been reported [33], and the creation of JJs in MgB₂ thin films by He-FIB irradiation has been demonstrated very recently [34].

Here, we report on the realization of He-FIB JJs in YBCO thin films on different substrates. We focus on the analysis of the electric-transport properties at 4.2 K of such JJs, complemented by numerical simulations based on the RCSJ model and on the dependence of the JJ properties on irradiation dose. We also present results on scanning transmission electron microscopy analysis of the local structural modification of the YBCO films, which can be made highly resistive by He-FIB irradiation with a high dose. The latter feature has been used to fabricate SQUIDS, by combination of medium-dose irradiation to produce two JJs with high-dose irradiation to produce the

SQUID loop, and we demonstrate dc SQUID operation, including low-noise performance.

II. DEVICE FABRICATION

We fabricate epitaxially grown *c*-axis-oriented YBCO thin films of thickness d by pulsed laser deposition (PLD) on various single-crystal (001)-oriented SrTiO₃ (STO), MgO, and (LaAlO₃)_{0.3}(Sr₂AlTaO₆)_{0.7} (LSAT) substrates (10×10 mm²). The crystalline quality of the YBCO films is characterized by x-ray diffraction to determine the full width at half maximum (FWHM) of the rocking curve of the YBCO (005) peak and to extract d via Laue oscillations at the YBCO (001) Bragg peak. YBCO films on STO substrates are covered *in situ* by an epitaxially grown STO cap layer with a thickness of 10 unit cells (3.9 nm). For details on the PLD growth of our YBCO films on STO substrates, as well as their structural and electric-transport properties, see Refs. [35,36].

For electrical contacts on STO and MgO chips, we photolithographically define a resist mask, covering the central area of the chips, remove an approximately 10-nm-thick surface layer (including the STO cap layer) by Ar ion milling, and *in situ* deposit a Au film by magnetron sputtering, followed by a lift-off process. For electrical contacts on LSAT chips, we deposit *in-situ*, after the PLD process, a Au film onto the YBCO by *in-situ* electron beam evaporation after the PLD process. Subsequently, we photolithographically define a resist mask, covering the outer area of the chips, and remove the Au film on the central area of the chip by Ar ion milling.

Afterward, we use photolithography and Ar ion milling to prepattern 156 YBCO microbridges of width $w \approx 4$ μ m (and length ≈ 200 μ m) on each chip for He ion irradiation and electric-transport measurements in a four-point configuration. Table I gives an overview of the five chips, with some basic properties of their YBCO microbridges, which have been used for fabricating devices via He-FIB irradiation. A specific bridge on one of the chips is labeled by the chip name, followed by $-n$ for bridge number n , e.g., STO-1-4 corresponds to bridge number 4 on the chip STO-1.

TABLE I. Properties of studied chips with YBCO thin film microbridges used for fabricating He-FIB-irradiated devices. To calculate the effective penetration depth $\lambda_{\text{eff}} = \lambda_L^2/d$, we assume a London penetration depth $\lambda_L = 250$ nm.

Chip (substrate)	T_c (K)	FWHM (deg)	d (nm)	w (μ m)	λ_{eff} (μ m)
STO-1	89	0.11	50	3.2	1.25
STO-2	89	0.15	29	4.0	2.16
STO-3	91	0.08	46	3.8	1.36
MgO-1	89	0.17	53	4.1	1.18
LSAT-1	86	0.07	50	4.4	1.25

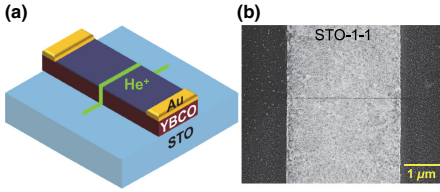


FIG. 1. (a) Schematic illustration of the He-FIB JJ geometry. (b) SEM image of a JJ (visible as thin dark line) fabricated with $D = 600$ ions/nm.

After pre patterning the YBCO microbridges, focused He-ion-beam irradiation is done in a Zeiss Orion NanoFab He/Ne ion microscope (HIM) with 30-keV He^+ ions. A beam current of 200 fA is used, and the beam is focused to a nominal diameter of 0.5 nm. A dwell time of 1 μs is used to irradiate line patterns with a dwell point spacing of 0.25 nm, which corresponds to a single linescan dose $D_{\text{SL}} = 5$ ions/nm. To obtain a certain line dose $D = Nd_{\text{SL}}$, a single linescan is repeated N times. To irradiate an area, adjacent linescans are offset by $\Delta = 0.25$ nm. In that case, a line dose of, e.g., $D = 100$ ions/nm corresponds to an area dose of $D_A \equiv D/\Delta = 400$ ions/nm² or 4×10^{16} ions/cm².

Figure 1(a) schematically illustrates the sample geometry and irradiation process for a single JJ. A scanning electron microscopy (SEM) image of STO-1-1 fabricated with $D = 600$ ions/nm is shown in Fig. 1(b). The irradiated linescan appears as a dark line in the SEM image due to He-FIB-induced carbon deposition from residual gas inside the He ion microscope chamber.

III. YBCO BRIDGES WITH HE-FIB-INDUCED BARRIERS AND JOSEPHSON JUNCTIONS

In this section, we present results obtained from devices fabricated on the chips listed in Table I.

A. Resistance vs temperature

Figure 2 shows measurements of the resistance R (at constant bias current $I_b = 1 \mu\text{A}$) vs temperature T of two YBCO microbridges. The $R(T)$ curve of STO-1-2, measured before He ion irradiation, shows a decrease of the resistance by about a factor of 3 from 300 to 100 K, with resistivity $\rho(100 \text{ K}) \approx 190 \mu\Omega\text{cm}$, followed by a sharp transition to $R < 1 \Omega$ at $T_c = 89$ K. After irradiation with $D = 700$ ions/nm (and thus producing a JJ), the $R(T)$ curve of STO-1-2 shows an additional footlike structure with a plateau at $R = 6.6 \Omega$ between approximately 40 K and T_c (see inset). This foot structure is due to thermally activated phase slippage [37] causing a finite voltage

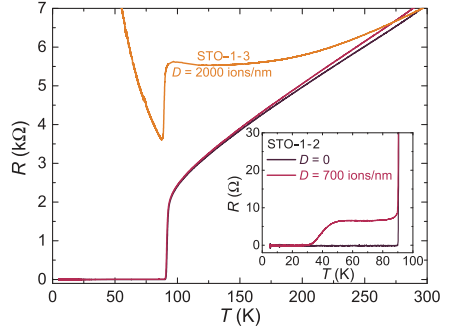


FIG. 2. $R(T)$ dependence of YBCO bridge STO-1-2 before and after irradiation and of STO-1-3 after irradiation. The inset shows an enlargement of the resistive transitions of STO-1-2.

drop across the JJ when (upon increasing T) the thermal energy $k_B T$ approaches the Josephson coupling energy $E_J = I_0 \Phi_0 / (2\pi)$. Here, I_0 is the noise-free critical current of the JJ (which decreases with increasing T) and Φ_0 is the magnetic flux quantum. Accordingly, the plateau reflects the situation when the measurable critical current I_c drops below the bias current I_b , causing the JJ to reach its normal state resistance R_n . He-FIB irradiation with a high dose fully suppresses I_c . This is shown in Fig. 2 for sample STO-1-3, which has been irradiated with $D = 2000$ ions/nm. At $T = 4.2$ K, the resistance is > 20 k Ω .

B. Transmission electron microscopy analysis

By the combination of atomic force microscopy and scanning near-field optical microscopy, it has been shown by Gozar *et al.* [33] that He-FIB irradiation with doses above 10^{18} ions/cm² induces amorphous tracks in $\text{La}_{1.84}\text{Sr}_{0.16}\text{CuO}_4$ thin films with a substantial lateral width of approximately 500 nm. In contrast to this, He-FIB produced JJs in YBCO films have been reported to show IVCs well described by the RCSJ model, indicating much less lateral damage [28]. However, no results have been reported on microstructural changes induced by a He-FIB in YBCO films so far.

To image possible structural modifications induced by He-FIB irradiation in our YBCO films, we use scanning transmission electron microscopy (STEM). For the STEM studies, we irradiate the YBCO bridge STO-1-4 with a series of 14 parallel lines using increasing doses from $D = 50$ to 10^3 ions/nm, with well-defined spacing (200 nm in most cases) between adjacent lines. Subsequently, we prepare a cross-sectional TEM lamella containing all irradiated lines, by *in situ* lift-out using a Ga-FIB microscope together with a micromanipulator. Figures 3(a)–3(d)

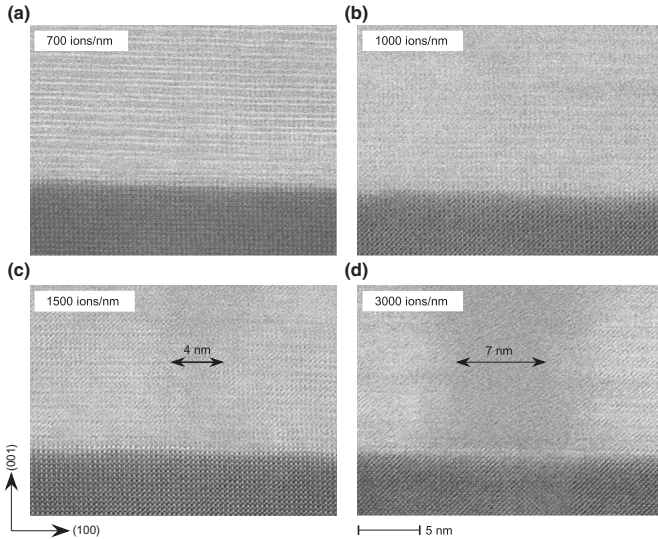


FIG. 3. Cross-section STEM images of the YBCO/STO interface (top/bottom, respectively) at the location of He-FIB irradiation with increasing dose D from (a) to (d). Arrows indicate the widths of amorphous regions.

show cross-section STEM images, viewed along the [010] zone axis, of four regions of the bottom part of the YBCO film at the YBCO/STO interface that are irradiated with $D = 700, 1000, 1500,$ and 3000 ions/nm, respectively. The areas that are irradiated with $D \geq 3000$ ions/nm can be easily located in the STEM images due to significant changes in the microstructure of the YBCO films. As we know the exact spacing between the different areas irradiated along the lamella, we can also easily localize in the STEM images the areas that have been irradiated with lower D . For $D = 700$ and 1000 ions/nm [cf. Figs. 3(a) and 3(b)], we cannot identify any change in the structure of the irradiated sections. For $D = 1500$ ions/nm, an amorphous track of width $w_a \approx 4$ nm appears [cf. Fig. 3(c)], increasing to $w_a \approx 7$ nm for $D = 3000$ ions/nm [cf. Fig. 3(d)]. We note that with further increasing D , the amorphous track width w_a increases roughly linearly up to approximately 170 nm for the highest dose $D = 10^5$ ions/nm that we investigate.

Our STEM analysis indicates that medium doses do not induce significant structural damage of the YBCO crystal lattice, which is consistent with the assumption that the He-FIB easily moves oxygen ions from the Cu-O chains to interstitial sites [30], thereby altering the local electric-transport properties of YBCO on the nanometer scale without destroying the crystal lattice as a whole. Hence, He-FIB irradiation with a medium dose seems to

be a very promising approach for creating JJs in YBCO. Moreover, we find that irradiation with larger doses of some 1000 ions/nm induces amorphous, and hence presumably highly resistive, regions, but still with a relatively small lateral extension of only a few nanometers.

C. Transport characteristics of He-FIB-induced Josephson junctions

In the following, we present electric-transport characteristics of approximately 50 YBCO bridges that are irradiated with doses up to $D = 800$ ions/nm to produce JJs. We measure IVCs, i.e., current I vs voltage V , and the modulation of the critical current I_c in an externally applied magnetic field B (perpendicular to the substrate plane) in an electrically and magnetically shielded environment, with the samples at $T = 4.2$ K immersed in liquid He.

For all devices exhibiting IVCs that can be described by the RCSJ model, we perform numerical simulations, including thermal noise, to determine their noise-free critical current I_0 , normal resistance R_n , and capacitance C . From these simulations, we determine the Stewart-McCumber parameter $\beta_C \equiv 2\pi I_0 R_n^2 C / \Phi_0$ and also the amount of excess current I_e , if present.

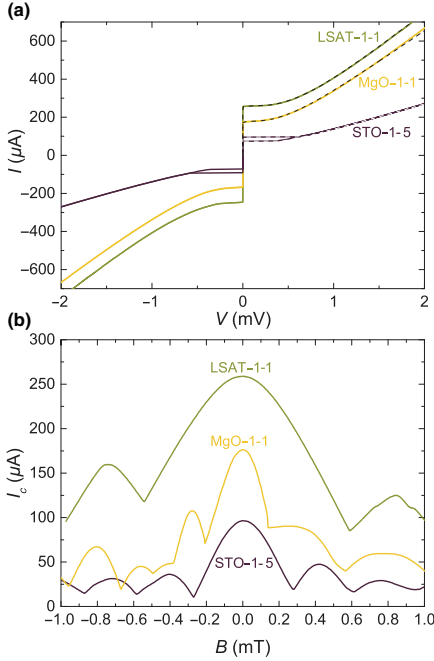


FIG. 4. Electric-transport characteristics of He-FIB JJs fabricated on different substrates: (a) IVCs showing experimental data (solid lines) and numerical simulation results for $I > 0$ (dashed lines) and (b) $I_c(B)$ patterns.

Figure 4 shows a representative set of IVCs [Fig. 4(a)] and $I_c(B)$ patterns [Fig. 4(b)] for JJs on different substrate materials. Irradiation doses and characteristic JJ parameters are given in Table II. As shown by the simulated curves [dashed lines in Fig. 4(a)], the IVCs can be well described by the RCSJ model and do not show any excess current. Only the JJ on STO shows a hysteresis in the IVC, with a JJ capacitance $C = 0.17$ pF and $\beta_C = 2.77$ obtained from simulations. Data regarding β_C for all JJs are presented and discussed at the end of this section.

TABLE II. Irradiation doses and device parameters of JJs shown in Fig. 4.

	D (ions/nm)	I_0 (μA)	R_n (Ω)	V_c (μV)	C (pF)	β_C	λ_J (μm)	λ_J^{NL} (μm)	B_{c1}^{ex} (mT)	B_{c1}^{LO} (mT)	B_{c1}^{NL} (mT)
STO-1-5	700	99	7.44	737	0.17	2.77	0.42	1.8	0.31	0.63	0.28
MgO-1-1	500	178	3.07	546	0.15	0.77	0.37	2.6	0.25	0.75	0.17
LSAT-1-1	200	260	2.69	699	0.15	0.83	0.30	3.5	0.76	0.88	0.15

The $I_c(B)$ patterns shown in Fig. 4(b) exhibit clear modulation of the critical current with applied magnetic field; however, they significantly deviate from the Fraunhofer-like shape expected for homogeneous JJs in the short junction limit $w \lesssim 4\lambda_J$, where

$$\lambda_J = \sqrt{\frac{\Phi_0}{2\pi\mu_0 d_{\text{eff}} j_0}} \quad (1)$$

is the Josephson penetration depth with the effective JJ inductance $\mu_0 d_{\text{eff}}$. Our YBCO films grown on STO have a London penetration depth $\lambda_L \approx 250$ nm [38–41]. Therefore, the devices discussed here are clearly in the thin-film limit $d \ll \lambda_L$ and, hence, the effective penetration depth $\lambda_{\text{eff}} = \lambda_L^2/d$ (see Table I) should be used to determine $d_{\text{eff}} = 2\lambda_{\text{eff}}$ in Eq. (1). Thus, we obtain the values of λ_J listed in Table II and see that all JJs are in the long JJ limit ($w > 4\lambda_J$).

Moreover, since $\lambda_J \ll \lambda_{\text{eff}}$, these JJs are in the nonlocal regime [42–46]. In this regime, the $I_c(B)$ patterns can be calculated analytically [42,46] only in the narrow JJ limit, i.e., for $w < \lambda_{\text{eff}}$ and $w < \lambda_J^{\text{NL}}$, where $\lambda_J^{\text{NL}} = \lambda_J^2/d$ is a nonlocal Josephson length [42]; see Table II. In our case, the above conditions are not really satisfied. Thus, our JJs are in the intermediate regime, where the exact shape of $I_c(B)$ is not known. However, we can roughly estimate the value of the penetration field B_{c1} [defined as a continuation of the first lobe of the $I_c(B)$ dependence down to $I_c = 0$] using (i) the local long JJ model and (ii) the narrow nonlocal JJ model [42] and compare them with experimentally measured values of B_{c1}^{ex} , given in Table II. The local long JJ model yields $B_{c1}^{\text{LO}} = \Phi_0/(\pi d_{\text{eff}} \lambda_J)$, whereas for a nonlocal narrow JJ [42], $B_{c1}^{\text{NL}} = \Phi_0/(0.715 w^2)$ (independent of j_0). By comparing these values with the experimental ones (see Table II), we see that B_{c1}^{ex} for STO-1-5 and MgO-1-1 are better described by the nonlocal theory, while B_{c1}^{ex} for LSAT-1-1 is closer to a local long JJ.

A detailed study of the $I_c(B)$ patterns of our He-FIB-induced JJs is out of the scope of the work presented here. Typically, our JJs on MgO have more irregular $I_c(B)$ patterns than those on STO and LSAT [cf. Fig. 4(b)]. This result indicates more inhomogeneous barrier properties of He-FIB-induced JJs on MgO and may either be attributed to the much larger lattice mismatch between MgO and YBCO and correspondingly poorer crystalline quality of

YBCO films or stronger charging of the MgO substrates that is observed during the He-FIB process.

In the following, we analyze the scaling of characteristic JJ properties j_c , ρ_n , and $j_c \rho_n$ with irradiation dose D . Note that devices irradiated with the lowest doses do not show JJ behavior. Therefore, we denote here all critical current densities as j_c . For all devices showing RCSJ behavior, however, the values given here refer to the noise-free values of j_0 obtained from numerical simulations.

Figure 5(a) summarizes $j_c(D)$ for all investigated devices. We attribute the significant scatter (cf. e.g., the

data points for 700 ions/nm on STO-1) to instabilities in the fabrication process that we have not yet optimized. For instance, slight variations in the He-FIB focus spot size and beam current both affect the barrier properties. In spite of this scatter, we clearly find an exponential decay $j_c(D) \approx j_{c,0} \exp(-D/D_0)$, with $j_{c,0} = 3 \times 10^7$ A/cm² and with $D_0 = 38$ ions/nm for LSAT-1 and $D_0 = 130$ ions/nm for the other chips. The reason for the much stronger decay of $j_c(D)$ on LSAT compared to the devices on STO or MgO has not been clarified yet. Clearly, we do not find a correlation of D_0 with YBCO film thickness or crystalline quality (cf. FWHM values in Table I).

For $j_c \lesssim 2$ MA/cm², the IVCs show RCSJ-like behavior, whereas devices with higher critical current densities yield flux-flow-type IVCs, as indicated by the gray area in Fig. 5(a). Altogether, the range of variation of j_c covers 5 orders of magnitude. We note that an exponentially decaying behavior of j_c is well known from cuprate grain boundaries, where j_c decays exponentially with the grain-boundary misorientation angle Θ [11,47,48]. In a theoretical analysis of cuprate grain-boundary JJs, Graser *et al.* [48] related the exponential decay of $j_c(\Theta)$ to charging of the interface near defects induced by the structural distortions at the grain boundary. For the He-FIB-induced JJ barriers, the locally induced defect structure is not known yet, and it remains to be clarified whether a similar charging mechanism is responsible for the exponential decay of $j_c(D)$. A simple explanation of the exponential decay of j_c with increasing D would be a linear increase of the JJ barrier thickness. As stated in Sec. B, the STEM analysis yields a roughly linear increase of the amorphous track width with increasing D for doses above 1000 ions/nm. However, for lower doses, the STEM data do not allow us to make a statement on the width of the induced defect regions and their scaling with D .

Our analysis of the IVCs of He-FIB JJs produced with variable doses also yields a systematic scaling of the resistance times area product $\rho_n \equiv R_n w d \approx \rho_{n,0} \exp(D/2D_0)$ with $\rho_{n,0} = 0.37$ n Ω cm²; i.e., ρ_n increases exponentially with D as shown in Fig. 5(b). Interestingly, the stronger decay of $j_c(D)$ for JJs on LSAT comes along with a correspondingly stronger increase in $\rho_n(D)$; i.e., we can use the same values of D_0 for the scaling of $\rho_n(D)$ as used for the scaling of $j_c(D)$. Accordingly, the characteristic voltage $V_c = j_c \rho_n$ also shows an exponential scaling $V_c \approx V_{c,0} \exp(-D/2D_0)$ with $V_{c,0} = j_{c,0} \rho_{n,0} = 11$ mV, as shown in Fig. 5(c). We note here that Figs. 5(b) and 5(c) contain only data points that correspond to RCSJ-type IVCs.

The fact that our analysis of the scaling of characteristic JJ properties (j_c , ρ_n , and V_c) with D can be described by the same values of D_0 indicates a universal scaling of V_c with either j_c or ρ_n independent of substrate material. This result is shown in Fig. 6, where we display $V_c(j_c)$ and $V_c(\rho_n)$ for all investigated JJs. Despite the

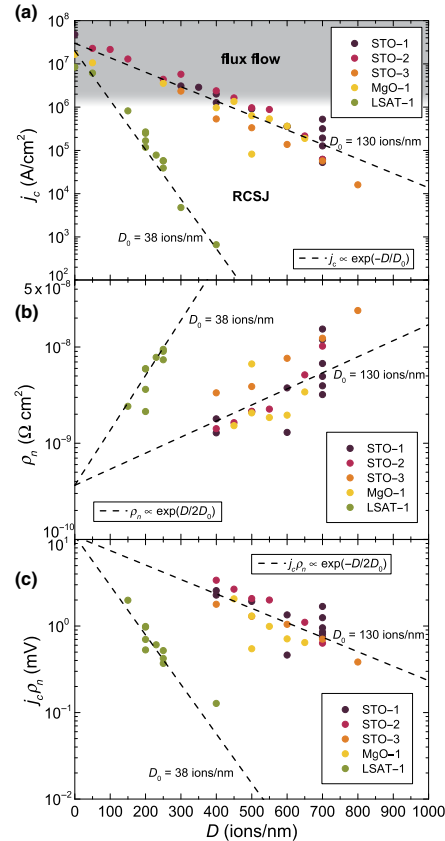


FIG. 5. Dependence of device parameters on He ion line dose D for various samples on different substrates: (a) $j_c(D)$, (b) $\rho_n(D)$, and (c) $j_c \rho_n(D)$. The dashed lines indicate the approximate scaling behavior as discussed in the text.

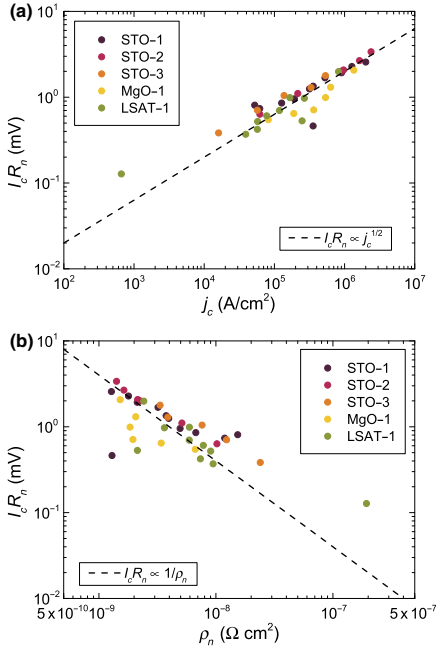


FIG. 6. Characteristic voltage $I_c R_n$ for He-FIB JJs with RCSJ-like IVCS on different substrates (a) vs critical current density j_c and (b) vs resistance times area ρ_n . Dashed lines indicate $I_c R_n \propto \sqrt{j_c}$ in (a) and $I_c R_n \propto 1/\rho_n$ in (b) as discussed in the text.

significant scatter in the data, a clear trend is visible, which can be described by $I_c R_n \approx V_{c,1} (j_c/j_{c,1})^{1/2}$ [dashed line in Fig. 6(a)], with $V_{c,1} = 2$ mV and $j_{c,1} = 10^6$ A/cm² and by $I_c R_n \approx V_{c,1} (\rho_{n,1}/\rho_n)$ [dashed line in Fig. 6(b)] with $\rho_{n,1} = 2$ n Ω cm². We note that an approximate scaling $I_c R_n \propto \sqrt{j_c}$ and $I_c R_n \propto 1/\rho_n$ has also been observed for many cuprate grain-boundary JJs and other JJ types in cuprate superconductors, albeit with a slightly larger $V_{c,1}$ for the same $j_{c,1}$ and $\rho_{c,1}$ [10]. However, we should also note that the existence or absence of a universal scaling of $I_c R_n$ vs j_c or ρ_n for all cuprate JJs and the origin of such a scaling has been discussed controversially in the literature; see, e.g., Refs. [10, 11, 16]. At least, for oxygen-depleted grain boundaries [11], there seems to be consensus on the same scaling as we see in our He-FIB JJs. This result is probably not surprising, because the He-FIB irradiation induces such an oxygen depletion [28].

So, obviously, for achieving large values of V_c , one should use doses that are as small as possible to obtain

large values of j_c , but still provide JJs with RCSJ-type IVCS. Moreover, for fabricating SQUIDS (cf. Sec. IV), one wants to have nonhysteretic IVCS, i.e., $\beta_C \lesssim 1$. To address these issues, we determine from RCSJ simulations the dependencies of β_C and of the excess current densities j_e of our He-FIB JJs on j_c .

Figure 7(a) shows $\beta_C(j_c)$. We clearly find a significant difference for devices on STO as compared to those on LSAT or MgO. While for devices on LSAT and MgO the values of β_C are essentially independent of j_c and yield values between approximately 0.5 and 1, for devices on STO, β_C is always above 1 (up to approximately 4) and decays with increasing j_c . This result reflects the fact that we observe hysteretic IVCS at 4.2 K for all JJs on STO substrates and nonhysteretic IVCS for all JJs on MgO and LSAT. We attribute this behavior to a significant stray capacitance contribution caused by the large permittivity of STO at low T [49]. However, a more detailed analysis of this behavior would require a systematic variation of the JJ width, which we do not perform for the present study. For YBCO grain-boundary JJs, the capacitance C per area A has been found to vary roughly [11] within 10^{-6} to 10^{-4} F/cm², with a significant increase with increasing j_c from roughly 10^3 to 10^6 A/cm². In contrast, for our He-FIB JJs, we find for most devices C/A to scatter within the range from 5×10^{-5} to 2×10^{-4} F/cm² with no clear dependence on j_c in the range from 2×10^4 to 2×10^6 A/cm² (not shown).

Figure 7(b) shows the normalized excess current density j_e/j_c vs j_c . For the largest values of j_c , we find excess currents that decay with decreasing j_c and finally disappear at $j_c \approx 2 \times 10^5$ A/cm². This behavior seems to be independent of the substrate material. The appearance of excess currents has also been reported for cuprate grain-boundary JJs and electron-beam damaged JJs with large current densities [11, 16]. Such JJs are often modeled as superconductor–normal-metal–superconductor (S – N – S) JJs. For He-FIB JJs in YBCO films, Cybart *et al.* [28] reported on the transition from S – N – S -type to superconductor–insulator–superconductor (S – I – S) type JJs upon increasing the irradiation dose. Our results are consistent with this observation; a more detailed analysis, however, requires transport measurements at variable temperature, which we have not performed so far in detail.

To conclude this section, we can state that for obtaining devices that do not exhibit excess currents, one should not exceed $j_c \approx 10^5$ A/cm². For devices on STO, however, such low j_c values come with values of β_C clearly above 1, i.e., with hysteretic IVCS. The $I_c(B)$ patterns of devices on MgO, on the other hand, show the strongest deviations from a Fraunhofer-like behavior. Hence, at the current state it seems that, among the substrate materials investigated here, He-FIB JJ devices on LSAT are most promising for applications.

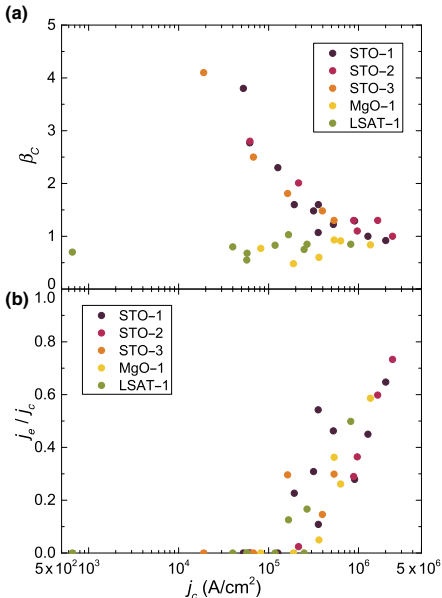


FIG. 7. (a) Stewart-McCumber parameter $\beta_c(j_c)$ and (b) normalized excess current $j_e/j_c(j_c)$ for He-FIB JJs on different substrates.

IV. HE-FIB-INDUCED DC SQUIDS

By irradiation with high He ion doses (typically for $D \gtrsim 1000$ ions/nm), j_c can be fully suppressed, as shown in Fig. 2, and the He-FIB-induced barriers can be made highly resistive (reaching even gigaohm resistances at 4.2 K for $D \gtrsim 5000$ ions/nm). This technique offers the possibility to define the sample geometry—ultimately on the nanometer scale—via direct-write lithography, without removing material by milling [30,31].

The combination of He-FIB irradiation with medium and high doses provides a simple way of fabricating dc SQUIDs from photolithographically prepatterned YBCO thin-film bridges on single-crystal substrates, with tailored JJ properties and SQUID inductance. We use this approach to fabricate simple micro- and nano-SQUIDs on STO, MgO, and LSAT substrates by first scanning over a square-shaped area at the center of the prepatterned YBCO bridge to define the SQUID “hole” (i.e., a highly resistive, magnetically transparent area) and a subsequent linescan across the whole width of the bridge using a medium dose to produce the JJs. A SEM image of such a SQUID is shown in the inset of Fig. 8(a) for a device fabricated

on STO-1 with a $1 \times 1\text{-}\mu\text{m}^2$ hole (irradiated with $D_A = 4000$ ions/nm²). Again, the locations of the JJs (irradiated with $D = 700$ ions/nm) and the SQUID hole are visible via the He-FIB-induced carbon deposition.

Since the hysteresis in the IVCs severely limits the performance of SQUIDs on STO substrates, the electric-transport and noise data shown in the following are measured on a device fabricated on LSAT-1. On the LSAT substrate, however, SEM imaging is only possible in poor quality due to charging of the substrate. For the device on LSAT, the SQUID hole is defined as a $300 \times 300\text{-nm}^2$ square, irradiated with $D_A = 4000$ ions/nm². The JJs are fabricated by a linescan with $D = 230$ ions/nm and have a width of approximately $2 \mu\text{m}$ each.

Figure 8(a) shows the IVCs for different applied magnetic flux to yield maximum (black) and minimum (red) positive critical current, exhibiting neither hysteresis nor excess current. From RCSJ simulations, we determine a mean per-junction critical current $I_0 = 43.6 \mu\text{A}$ and normal state resistance $R_n = 9.50 \Omega$ ($V_c = 414 \mu\text{V}$) and $\beta_C = 0.74$. The dependence of the critical current $I_{c,s}$ of the SQUID on the magnetic field is shown in Fig. 8(b) as solid lines, together with the numerically simulated dependence, based on the RCSJ model [50] (symbols). From the simulations, we extract the screening parameter $\beta_L \equiv 2I_c L / \Phi_0 = 0.79$, inductance $L = 19 \text{ pH}$, and asymmetry parameters [50] for the critical current $\alpha_I = 0.145$ and inductance $\alpha_L = -0.15$. Figure 8(c) shows the voltage-flux dependence of the SQUID for a range of bias currents $I_b \approx \pm 110 \mu\text{A}$ in steps of $4 \mu\text{A}$. The dark dot near the center on the curve for $I_b = -85 \mu\text{A}$ indicates the working point with a transfer function $V_\Phi = 2.1 \text{ mV}/\Phi_0$, which is used for the noise measurement shown in Fig. 9.

To determine the spectral density of flux noise S_Φ vs frequency f of the SQUID, we use Magnicon SEL-1 SQUID electronics [51] in direct readout mode [52]. Figure 9 shows the measured rms spectral density of flux noise $S_\Phi^{1/2}(f)$ of the SQUID (red), together with the background noise of the readout electronics (black). The noise spectrum is dominated by frequency-dependent excess noise, scaling roughly as $S_\Phi \propto 1/f$ ($1/f$ noise), with a small bump (at approximately 10 kHz). This excess noise extends all the way up to the cutoff frequency $f_{el} = 166 \text{ kHz}$ of our readout electronics (limited by the sampling rate of the analog-to-digital converter), where it almost reaches the noise floor of the readout electronics. For YBCO SQUIDs, one typically finds a strong $1/f$ noise contribution due to I_c fluctuations in the JJs [8]. This result is also probably the case for the SQUID presented here. To further clarify this, one should operate the SQUIDs in current-bias reversal mode [53], which eliminates the excess noise contribution from I_c fluctuations. We have already successfully demonstrated this approach for YBCO nano-SQUIDs based on grain-boundary JJs [54]; however, for the simple SQUID layout without a suitable

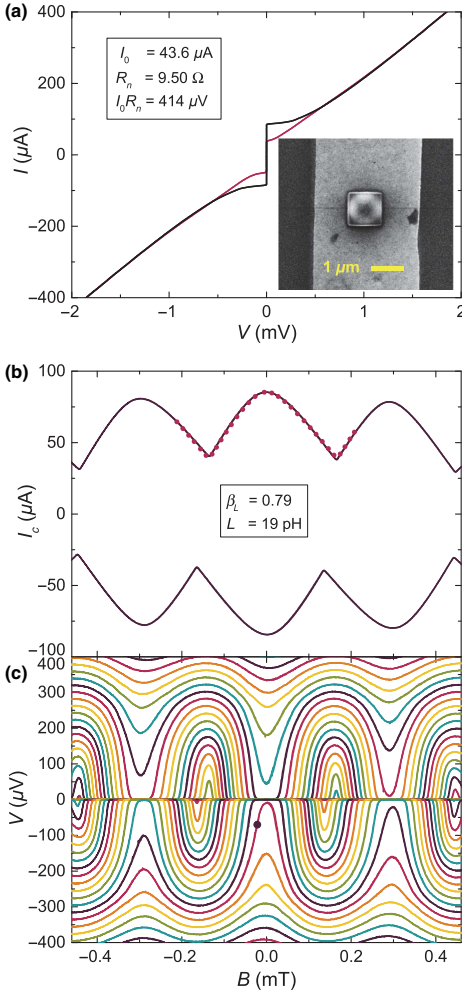


FIG. 8. Electric-transport characteristics of a He-FIB dc SQUID fabricated on LSAT-1-2. (a) IVCs for applied flux yielding maximum (black) and minimum (red) positive critical current. The inset shows a SEM image of a similar SQUID fabricated on STO-1. (b) Critical current vs magnetic field: experimental data (solid lines) and numerical simulation (symbols). (c) Voltage-flux dependence for bias currents I_b within approximately $\pm 110 \mu\text{A}$ in steps of $4 \mu\text{A}$. The dark dot near the center indicates the working point for noise measurement.

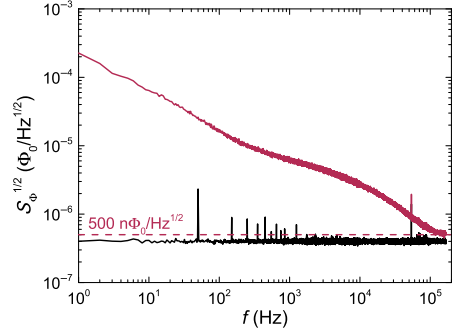


FIG. 9. Noise characteristics of a He-FIB dc SQUID fabricated on LSAT-1-2, with flux noise spectra of the SQUID (red) and electronics background (black). The dashed line indicates the upper limit for thermal white noise $S_{\Phi,wt}^{1/2} = 500 \text{ n}\Phi_0/\text{Hz}^{1/2}$ of the SQUID.

on-chip flux coupling structure, as used in this work, it is not possible to use this approach. At least, from the noise data shown in Fig. 9, we can give an upper limit for the thermal white noise $S_{\Phi,wt}^{1/2} \lesssim 500 \text{ n}\Phi_0/\text{Hz}^{1/2}$, which is impressively low for a $L \approx 20 \text{ pH}$ SQUID.

V. CONCLUSIONS

We demonstrate the fabrication of YBCO Josephson junctions and dc SQUIDs by using a focused He ion beam, which locally modifies epitaxially grown YBCO thin films and allows us to “write” Josephson barriers and insulating areas with high spatial resolution. The analysis of the electric-transport properties at 4.2 K of our He-FIB-induced structures confirms and extends earlier results obtained by Cybart and co-workers [28–30].

We study in detail the dependence of characteristic JJ properties on the irradiation dose for devices on STO, MgO, and LSAT substrates. Upon increasing the irradiation dose, we find a transition from flux-flow to RCSJ-like behavior with some excess current contribution that vanishes upon further increasing the dose. Moreover, we find an exponential decay of the critical current density j_0 with increasing dose. For currently unclear reasons, this decay is much faster for devices on LSAT as compared to devices on STO and MgO. Another major difference regarding JJ behavior on different substrates is the observation of hysteretic IVCs for devices on STO, while devices on LSAT and MgO show no hysteresis. We attribute the hysteresis in the IVCs to a stray capacitance contribution from the STO substrates. The analysis of the characteristic voltage V_c of the fabricated JJs yields an approximate scaling $V_c \propto \sqrt{j_0}$.

Altogether, He-FIB JJs offer new perspectives for creating Josephson devices, because of the possibility to control the JJ properties by irradiation dose, even on the same substrate, and to place the JJs at virtually arbitrary positions. This flexibility obviously offers an enormous advantage for creating advanced devices, in particular employing multi-JJ configurations. Our detailed analysis of the JJ properties can be helpful for designing optimized devices for applications.

Moreover, irradiation with a high dose drives the material to be highly resistive. In this regime, our STEM analysis shows the creation of amorphous tracks in the YBCO films, which for not-too-high doses still have a lateral extension down to only a few nanometers. This observation indicates that He-FIB irradiation is a promising tool for nanopatterning (without removal of material) of YBCO films with ultrahigh resolution. We use this feature to produce dc SQUIDs by patterning both the JJs and the SQUID loop by He-FIB irradiation. For a device on LSAT, we demonstrate very low flux noise in the thermal white-noise regime. The observed low-frequency excess noise still has to be investigated in detail in further studies. Although we have not yet pushed to the ultimate limit of miniaturization, we envisage that He-FIB irradiation should be ideally suited for the realization of ultralow-noise nano-SQUIDs [55,56] due to the high spatial resolution of helium ion microscopy.

ACKNOWLEDGMENTS

B.M. acknowledges funding by the German Academic Scholarship Foundation. We gratefully acknowledge fruitful discussions with S. Cybart, V.G. Kogan, R.G. Mints, and R. Menditto and technical support by M. Turad and R. Löffler (LISA⁺), W. Nisch and C. Warres (NMI), and C. Back. This work is supported by the COST action NANOCOBYBRI (Grant No. CA16218).

-
- [1] K. K. Likharev, Superconducting weak links, *Rev. Mod. Phys.* **51**, 101 (1979).
 - [2] A. Barone and G. Paternò, *Physics and Applications of the Josephson Effect* (John Wiley & Sons, New York, 1982).
 - [3] R. Kleiner and W. Buckel, *Superconductivity*, 3rd ed., (Wiley-VCH, Weinheim, 2016).
 - [4] M. Bhushan and E. M. Macedo, Nb/AIO_x/Nb trilayer process for the fabrication of submicron Josephson junctions and low-noise dc SQUIDs, *Appl. Phys. Lett.* **58**, 1323 (1991).
 - [5] D. Hagedorn, O. Kieler, R. Dolata, R. Behr, F. Müller, J. Kohlmann, and J. Niemeyer, Modified fabrication of planar sub- μm superconductor-normal metal-superconductor Josephson junctions for use in a Josephson arbitrary waveform synthesizer, *Supercond. Sci. Technol.* **19**, 294 (2006).
 - [6] U. Welp, K. Kadowaki, and R. Kleiner, Superconducting emitters of THz radiation, *Nat. Photon.* **7**, 702 (2013).
 - [7] T. Ortlepp, Ariando Amd O. Mielke, C. J. M. Verwijs, K. F. K. Foo, H. Rogalla, F. H. Uhlmann, and H. Hilgenkamp, Flip-flopping fractional flux quanta, *Science* **312**, 1495 (2006).
 - [8] D. Koelle, R. Kleiner, F. Ludwig, E. Dantsker, John Clarke, High-transition-temperature superconducting quantum interference devices, *Rev. Mod. Phys.* **71**, 631 (1999).
 - [9] M. I. Faley, J. Dammers, Y. V. Maslennikov, J. F. Schneiderman, D. Winkler, V. P. Koshelets, N. J. Shah, and R. E. Dunin-Borkowski, High- T_c SQUID biomagnetometers, *Supercond. Sci. Technol.* **30**, 083001 (2017).
 - [10] R. Gross, L. Alf, A. Beck, O. M. Froehlich, D. Koelle, and A. Marx, Physics and technology of high temperature superconducting Josephson junctions, *IEEE Trans. Appl. Supercond.* **7**, 2929 (1997).
 - [11] H. Hilgenkamp and J. Mannhart, Grain boundaries in high- T_c superconductors, *Rev. Mod. Phys.* **74**, 485 (2002).
 - [12] F. Tafuri and J. R. Kirtley, Weak links in high critical temperature superconductors, *Rep. Prog. Phys.* **68**, 2573 (2005).
 - [13] F. Tafuri, D. Massarotti, L. Galletti, D. Stormaiuolo, D. Montemurro, L. Longobardi, P. Lucignano, G. Rotoli, G. P. Pepe, A. Tagliacozzo, and F. Lombardi, Recent achievements on the physics of high- T_c superconductor Josephson junctions: Background, perspectives and inspiration, *J. Supercond. Nov. Magn.* **26**, 21 (2013).
 - [14] K. Cedergren, J. R. Kirtley, T. Bauch, G. Rotoli, A. Troeman, H. Hilgenkamp, F. Tafuri, and F. Lombardi, Interplay between Static and Dynamic Properties of Semifluxons in YBa₂Cu₃O_{7- δ} 0- π Josephson Junctions, *Phys. Rev. Lett.* **104**, 177003 (2010).
 - [15] S. K. Tolpygo, B. Nadgorny, S. Shokhor, F. Tafuri, Y. Lin, A. Bourdillon, and M. Gurvitch, Electron beam writing in fabricating planar high- T_c Josephson junctions, *Phys. C* **209**, 211 (1993).
 - [16] A. J. Pauza, W. E. Booij, K. Herrmann, D. F. Moore, M. G. Blamire, D. A. Rudman, and L. R. Vale, Electron-beam damaged high-temperature superconductor Josephson junctions, *J. Appl. Phys.* **82**, 5612 (1997).
 - [17] W. E. Booij, A. J. Pauza, D. F. Moore, E. J. Tarte, and M. G. Blamire, Electrodynamics of closely coupled YBa₂Cu₃O_{7- δ} junctions, *IEEE Trans. Appl. Supercond.* **7**, 3025 (1997).
 - [18] W. E. Booij, C. A. Elwell, E. J. Tarte, P. F. McBrien, F. Kahlmann, D. F. Moore, M. G. Blamire, N. H. Peng, and C. Jaynes, Electrical properties of electron and ion beam irradiated YBa₂Cu₃O_{7- δ} , *IEEE Trans. Appl. Supercond.* **9**, 2886 (1999).
 - [19] K. Chen, S. A. Cybart, and R. C. Dynes, Planar thin film YBa₂Cu₃O_{7- δ} Josephson junction pairs and arrays via nanolithography and ion damage, *Appl. Phys. Lett.* **85**, 2863 (2004).
 - [20] K. Chen, S. A. Cybart, and R. C. Dynes, Study of closely spaced YBa₂Cu₃O_{7- δ} Josephson junction pairs, *IEEE Trans. Appl. Supercond.* **15**, 149 (2005).
 - [21] S. S. Tinchev, Investigation of RF SQUIDs made from epitaxial YBCO films, *Supercond. Sci. Technol.* **3**, 500 (1990).

- [22] N. Bergeal, X. Grison, J. Lesueur, G. Faini, M. Aprili, and J. P. Contour, High-quality planar high- T_c Josephson junctions, *Appl. Phys. Lett.* **87**, 102502 (2005).
- [23] W. C. Stewart, Current-voltage characteristics of Josephson junctions, *Appl. Phys. Lett.* **12**, 277 (1968).
- [24] D. E. McCumber, Effect of ac impedance of dc voltage-current characteristics of Josephson junctions, *J. Appl. Phys.* **39**, 3113 (1968).
- [25] S. A. Cybart, P. X. T. Yen, E. Y. Cho, J. U. Huh, V. N. Glyantsev, C. S. Yung, B. Moeckly, J. W. Beeman, and R. C. Dynes, Comparison of Y–Ba–Cu–O films irradiated with helium and neon ions for the fabrication of Josephson devices, *IEEE Trans. Appl. Supercond.* **24**, 1100105 (2014).
- [26] W. Lang, and J. D. Pedarnig, in *Nanoscience and Engineering in Superconductivity*, edited by V. Moshchalkov, R. Wördenweber, and W. Lang (Springer Verlag, Berlin Heidelberg, 2010) Chap. 3, p. 81.
- [27] G. Hlawacek and A. Götzhäuser, eds., *Helium Ion Microscopy* (Springer International Publishing, Cham, Switzerland, 2016).
- [28] S. A. Cybart, E. Y. Cho, J. T. Wong, B. H. Wehlin, M. K. Ma, C. Huynh, and R. C. Dynes, Nano Josephson superconducting tunnel junctions in $\text{YBa}_2\text{Cu}_3\text{O}_{7-\delta}$ directly patterned with a focused helium ion beam, *Nat. Nano* **10**, 598 (2015).
- [29] E. Y. Cho, M. K. Ma, C. Huynh, K. Pratt, D. N. Paulson, V. N. Glyantsev, R. C. Dynes, and S. A. Cybart, $\text{YBa}_2\text{Cu}_3\text{O}_{7-\delta}$ superconducting quantum interference devices with metallic to insulating barriers written with a focused helium ion beam, *Appl. Phys. Lett.* **106**, 252601 (2015).
- [30] E. Y. Cho, Y. W. Zhou, J. Y. Cho, and S. A. Cybart, Superconducting nano Josephson junctions patterned with a focused helium ion beam, *Appl. Phys. Lett.* **113**, 022604 (2018).
- [31] E. Y. Cho, H. Li, J. C. LeFebvre, Y. W. Zhou, R. C. Dynes, and S. A. Cybart, Direct-coupled micro-magnetometer with Y–Ba–Cu–O nano-slit SQUID fabricated with a focused helium ion beam, *Appl. Phys. Lett.* **113**, 162602 (2018).
- [32] S. Cybart, R. Bali, G. Hlawacek, F. Röder, and J. Fassbender, in *Helium Ion Microscopy*, edited by G. Hlawacek and A. Götzhäuser (Springer International Publishing, Cham, Switzerland, 2016) Chap. 17, p. 415.
- [33] A. Gozar, N. E. Litombe, Jennifer E. Hoffman, and I. Bozovic, Optical nanoscopy of high T_c cuprate nanoconstriction devices patterned by helium ion beams, *Nano Lett.* **17**, 1582 (2017).
- [34] L. Kasaei, T. Melbourne, V. Manichev, L. C. Feldman, T. Gustafsson, Ke Chen, X. X. Xi, and B. A. Davidson, MgB_2 Josephson junctions produced by focused helium ion beam irradiation, *AIP Adv.* **8**, 075020 (2018).
- [35] R. Werner, C. Raisch, A. Ruosi, B. A. Davidson, P. Nagel, M. Merz, S. Schuppler, M. Glaser, J. Fujii, T. Chassé, R. Kleiner, and D. Koelle, $\text{YBa}_2\text{Cu}_3\text{O}_7/\text{La}_{0.7}\text{Ca}_{0.3}\text{MnO}_3$ bilayers: Interface coupling and electric transport properties, *Phys. Rev. B* **82**, 224509 (2010).
- [36] T. Schwarz, J. Nagel, R. Wölbling, M. Kemmler, R. Kleiner, and D. Koelle, Low-noise nano superconducting quantum interference device operating in tesla magnetic fields, *ACS Nano* **7**, 844 (2013).
- [37] R. Gross, P. Chaudhari, D. Dimos, A. Gupta, and G. Koren, Thermally Activated Phase Slippage in High- T_c Grain-boundary Josephson Junctions, *Phys. Rev. Lett.* **64**, 228 (1990).
- [38] R. Wölbling, T. Schwarz, B. Müller, J. Nagel, M. Kemmler, R. Kleiner, and D. Koelle, Optimizing the spin sensitivity of grain boundary junction nanoSQUIDs – Towards detection of small spin systems with single-spin resolution, *Supercond. Sci. Technol.* **27**, 125007 (2014).
- [39] L. Thiel, D. Rohner, M. Ganzhorn, P. Appel, E. Neu, B. Müller, R. Kleiner, D. Koelle, and P. Maletinsky, Quantitative nanoscale vortex imaging using a cryogenic quantum magnetometer, *Nat. Nanotechnol.* **11**, 677 (2016).
- [40] M. J. Martínez-Pérez, B. Müller, D. Schwabius, D. Korinski, R. Kleiner, J. Sesé, and D. Koelle, NanoSQUID magnetometry of individual cobalt nanoparticles grown by focused electron beam induced deposition, *Supercond. Sci. Technol.* **30**, 024003 (2017).
- [41] D. Rohner, L. Thiel, B. Müller, M. Kasperczyk, R. Kleiner, D. Koelle, and P. Maletinsky, Real-space probing of the local magnetic response of thin-film superconductors using single spin magnetometry, *Sensors* **18**, 3790 (2018).
- [42] M. Moshe, V. G. Kogan, and R. G. Mints, Edge-type Josephson junctions in narrow thin-film strips, *Phys. Rev. B* **78**, 020510 (2008).
- [43] A. A. Abdumalikov Jr., G. L. Alfimov, and A. S. Malishevskii, Nonlocal electrodynamics of Josephson vortices in superconducting circuits, *Supercond. Sci. Technol.* **22**, 023001 (2009).
- [44] John R. Clem, Josephson junctions in thin and narrow rectangular superconducting strips, *Phys. Rev. B* **81**, 144515 (2010).
- [45] A. A. Boris, A. Rydh, T. Golod, H. Motzkau, A. M. Klushin, and V. M. Krasnov, Evidence for Nonlocal Electrodynamics in Planar Josephson Junctions, *Phys. Rev. Lett.* **111**, 117002 (2013).
- [46] V. G. Kogan and R. G. Mints, Manipulating Josephson junctions in thin-films by nearby vortices, *Phys. C* **502**, 58 (2014).
- [47] R. Gross and B. Mayer, Transport processes and noise in $\text{YBa}_2\text{Cu}_3\text{O}_{7-\delta}$ grain boundary junctions, *Phys. C* **180**, 235 (1991).
- [48] S. Graser, P. J. Hirschfeld, T. Kopp, R. Gutser, B. M. Andersen, and J. Mannhart, How grain boundaries limit supercurrents in high-temperature superconductors, *Nature Phys.* **6**, 609 (2010).
- [49] A. Beck, A. Stenzel, O. M. Froehlich, R. Gerber, R. Gerdemann, L. Alff, B. Mayer, R. Gross, A. Marx, J. C. Villegier, and H. Moriceau, Fabrication and superconducting transport properties of bicrystal grain boundary Josephson junctions on different substrates, *IEEE Trans. Appl. Supercond.* **5**, 2192 (1995).
- [50] B. Chesca, R. Kleiner, and D. Koelle, in *The SQUID Handbook*, Vol. 1: Fundamentals and Technology of SQUIDs and SQUID systems, edited by John Clarke and Alex I. Braginski (Wiley-VCH, Weinheim, 2004) Chap. 2, p. 29.
- [51] SQUID electronics SEL-1 from Magnicon GmbH, Lemshaldt Landstr. 171, D-22397 Hamburg, Germany; <http://www.magnicon.com>.


- [52] D. Drung, High- T_c and low- T_c dc SQUID electronics, *Supercond. Sci. Technol.* **16**, 1320 (2003).
- [53] D. Drung, and M. Mück, in *The SQUID Handbook, Vol. 1: Fundamentals and Technology of SQUIDs and SQUID systems*, edited by John Clarke and Alex I. Braginski, (Wiley-VCH Weinheim, 2004) Chap. 4, p. 127.
- [54] T. Schwarz, R. Wölbing, C. F. Reiche, B. Müller, M. J. Martínez-Pérez, T. Mühl, B. Büchner, R. Kleiner, and D. Koelle, Low-noise $\text{YBa}_2\text{Cu}_3\text{O}_7$ Nano-SQUIDs for Performing Magnetization-reversal Measurements on Magnetic Nanoparticles, *Phys. Rev. Appl.* **3**, 044011 (2015).
- [55] C. Granata and A. Vettoliere, Nano superconducting quantum interference device: A powerful tool for nanoscale investigations, *Phys. Rep.* **614**, 1 (2016).
- [56] M. J. Martínez-Pérez and D. Koelle, NanoSQUIDs: Basics & recent advances, *Phys. Sci. Rev.* **2**, 20175001 (2017).

Publication 2

Reprinted with permission from
M. Karrer et al., Physical Review Applied **21**, 014065 (2024)
Copyright © 2024 by the American Physical Society.

Temporal evolution of electric transport properties of $\text{YBa}_2\text{Cu}_3\text{O}_{7-\delta}$ Josephson junctions produced by focused-helium-ion-beam irradiation

M. Karrer[✉], K. Wurster, J. Linek, M. Meichsner, R. Kleiner, E. Goldobin, and D. Koelle^{✉*}
Physikalisches Institut, Center for Quantum Science (CQ) and LISA⁺, Eberhard Karls Universität Tübingen, Auf der Morgenstelle 14, Tübingen 72076, Germany

 (Received 18 November 2023; accepted 18 January 2024; published 31 January 2024)

We examined the temporal evolution of Josephson and resistive barriers created by a 30-keV focused helium ion beam in microbridges of epitaxially grown single-crystal $\text{YBa}_2\text{Cu}_3\text{O}_{7-\delta}$ thin films. Repeated electric transport measurements at 4.2 K within 300 days after irradiation revealed an increase in the critical current density j_c for devices stored at room temperature under nitrogen atmosphere. This behavior can be described by a diffusion-based model of displaced chain oxygen moving back to original lattice sites, thus healing the barrier and partially restoring critical current. We find that $j_c \propto \exp(-\sqrt{t/\tau})$ with time t . The relaxation time τ increases exponentially with helium irradiation dose and can exceed several hundred days for high-quality Josephson junctions. To achieve higher diffusion rates and thus shorter relaxation times, we annealed some devices in different oxygen partial pressures, right after irradiation. Within a week, those junctions relaxed to a quasistable state, making this a feasible option to achieve temporal stability of device parameters.

DOI: [10.1103/PhysRevApplied.21.014065](https://doi.org/10.1103/PhysRevApplied.21.014065)

I. INTRODUCTION

The manufacturing of superconducting electronics devices and circuits based on the high-transition temperature (high- T_c) cuprate superconductors is still challenging. Using a multilayer technology including trilayer Josephson junctions (JJs), difficulties arise due to complex material composition, the short superconductor coherence length and the need for fully epitaxial layer growth [1,2]. So far, high- T_c JJ technologies are vastly based on single-layer $\text{YBa}_2\text{Cu}_3\text{O}_{7-\delta}$ (YBCO) thin films with grain boundaries as Josephson barriers [3,4]. However, to rely on grain boundaries is heavily restricting with respect to possible circuit designs. In the 1990s, another approach was pursued with various attempts to create Josephson barriers in epitaxially grown YBCO films by local irradiation with high-energetic electron or ion beams [5–9]. However, the resulting barriers were lacking quality, e.g., in terms of lower values of the characteristic voltage V_c (critical current times junction resistance) and larger excess currents compared to grain-boundary-based JJs. After the invention of the gas-field ion source (GFIS) [10], which enabled unprecedentedly high spatial resolution in focused-ion-beam (FIB) imaging and patterning with 30-keV helium ions, a breakthrough in fabrication of JJs occurred [11]. Since then, the fabrication of JJs and more sophisticated devices by irradiating high- T_c

cuprate superconductors with a 30-keV focused He ion beam (He FIB) was reported by several groups [12–16].

The mechanism behind the fabrication of He-FIB-induced Josephson barriers in YBCO is, presumably as follows. The accelerated He ions with an energy of 30 keV have significant momentum compared to electrons and are capable of displacing the atoms in the YBCO lattice. SRIM [17] simulations show that mainly the chain oxygen, with approximately 1-eV binding energy [18] is displaced, which creates oxygen vacancies in YBCO [19]. Since superconductivity in YBCO heavily depends on the oxygen doping, one can expect a local reduction of the superconducting properties [20–22]. Therefore, He-FIB irradiation introduces a local imbalance of doping, which reduces with time due to thermal diffusion of oxygen, which drives the system back towards a state of (quasi)equilibrium.

Obviously, the temporal evolution of the He-FIB-induced defect structure at the barrier directly affects the electronic characteristics of the devices, i.e., device properties changes with time. This effect is certainly detrimental to applications where stable device properties are required. It has been shown already that devices can be stabilized by annealing after irradiation. So far, annealing of devices in YBCO was performed for devices produced by irradiation with (80–120)-keV electrons with a scanning-transmission-electron microscope [6] and 175-keV Ne^+ ions using a trilayer implantation mask [23]. However, the temporal evolution of parameters describing the electrical

*koelle@uni-tuebingen.de

transport properties of YBCO JJs produced by He-FIB irradiation has not yet been investigated, while research of the temporal stability of ion-irradiated junctions using nanolithography has already been reported [24,25]. Temporal stability is useful not only for applications where stable device parameters are needed over time but also for research, e.g., in concurrent measurements that need some time to setup. An easy known way for achieving temporal stability of He-FIB JJs is to store them at cryogenic temperatures. However, this method is under most circumstances not very suitable.

In this paper, we present the results obtained with a different approach: we first investigated the temporal evolution of electric transport parameters of He-FIB JJs, which were stored at room temperature in a nitrogen (N_2) atmosphere. Subsequently, we investigated how an annealing process with different oxygen (O_2) partial pressures changes the junction properties and their temporal evolution.

II. SAMPLE FABRICATION

We fabricated epitaxially grown *c*-axis-oriented YBCO thin films on $10 \times 10 \text{ mm}^2$ single-crystal (100) $(\text{LaAlO}_3)_{0.3}(\text{Sr}_2\text{AlTaO}_6)_{0.7}$ (LSAT) substrates by pulsed-laser deposition (PLD) with a 20-nm-thick *in situ* Au layer on top deposited by electron-beam evaporation. For this study we used two chips (1 and 2), which were fabricated with nominally the same process parameters. To estimate the quality of the unpatterned YBCO films, x-ray diffraction (XRD) was performed after film growth, and the critical temperature T_c was measured using an inductive method [26].

Figure 1 shows a representative set of XRD measurements from chip 2. From the positions of the (00ℓ) Bragg peaks along the 2θ axis, the *c*-axis lattice constant of the YBCO film was determined to be 11.67 Å. A YBCO film thickness $d = 30 \text{ nm}$ could be extracted from the Laue fringes [27] at the YBCO (001) Bragg peak (see left inset in Fig. 1). The right inset in Fig. 1 shows the rocking curve of the YBCO (005) Bragg peak. The full width at half maximum (FWHM) of the rocking curve is 0.069° , thus indicating a high crystal quality. Our films yield $T_c \approx 89 \text{ K}$, with a transition width below 1 K. Both YBCO films showed variations of their properties (T_c , thickness, FWHM of the rocking curve and *c*-axis lattice constant) below 5% of the given values.

For a two-step photolithography process we used a MLA100 MASKLESS ALIGNER (Heidelberg Instruments) and positive resist MA-P 1205 (Micro Resist Technology). During the first step we patterned the Au/YBCO bilayer by Ar ion milling to create microbridges with width $w = 3 \mu\text{m}$ and contact pads covered by Au. During the second step we removed the Au layer with commercially available Lugol's iodine TECHNIETCHTMAC12 only on top of the

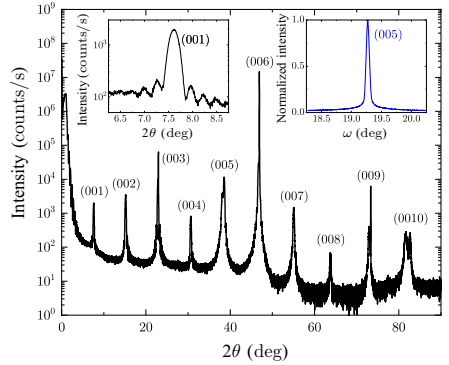


FIG. 1. XRD data of the unpatterned chip 2. Main graph: 2θ - ω overview scan with (00ℓ) Bragg peaks. Left inset: enlargement of the YBCO (001) peak with Laue fringes. Right inset: ω scan (rocking curve) at the YBCO (005) peak.

microbridges to expose the YBCO underneath, and along narrow stripes across the contact pads to split the Au contacts into two parts, enabling four-point measurements of the junctions later on. On each chip, we fabricated eight structures (A to H), each of which contain seven microbridges (each $50 \mu\text{m}$ long) in a meandering configuration. Figure 2 shows an optical microscope image after lithography of the central part of chip 2, structure A, denoted as 2A.

For He-FIB irradiation, the samples were mounted (and electrically grounded) on an aluminum sample stub and loaded into a ORION NANOFAB (Zeiss Microscopy). Junctions with different line dose D were written by irradiating with a 30-keV He FIB along a line perpendicular

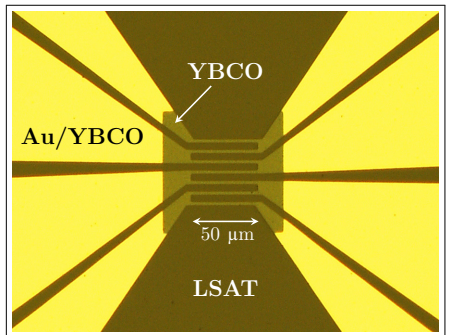


FIG. 2. Optical microscope image of the central part of structure 2A with seven microbridges after pre patterning.

to the YBCO microbridges. The beam current for fixed parameters of the ion focusing unit, e.g., spot size and aperture, resulted in 325 fA for 1A, 300 fA for 2D, and 200 fA for 2E. The dwell time per pixel was set to 1 μ s and the number of line repeats was varied to set different dose values in units of ions per nm, which are directly proportional to the beam current and automatically set for the deflection unit by the used NanoPatterning and Visualization Engine (NPVE). For typical beam currents of around 300 fA, the used doses from 100 to 1000 ions/nm require about 10 to 100 repeats, respectively. Within each structure, we denote the seven junctions by the different line doses used for He-FIB irradiation; for example, the junction on chip 1 located in structure A and irradiated with $D = 300$ ions/nm is denoted as 1A-300.

III. EXPERIMENTAL SETUP AND PROCEDURE

We measured current-voltage (I - V) characteristics and the modulation of the critical current I_c in an externally applied magnetic field B (along the normal to the YBCO film plane) in a current bias mode. For the $I_c(B)$ measurements a voltage criterion of 3 μ V was used to determine I_c . This criterion was 1 μ V above the typical noise level in our setup for the used gain settings of the preamplifiers. Measurements were performed by immersing the samples in liquid helium at temperature $T = 4.2$ K inside an electrically and magnetically shielded environment within a high-frequency shielding chamber.

In order to investigate the evolution of the properties of the junctions over time, we define day zero ($t = 0$) as the day when the bridges have been He-FIB-irradiated to form the JJs. Due to inevitable delays in the handling of the sample, the first measurement after the irradiation is conducted at $0 < t_{\text{initial}} \leq 1$ day. Furthermore, for the compensation of errors on the time axis we tracked (and subtracted) the time when the sample was in the measurement setup and exposed to lower temperatures.

A. Temporal evolution of the properties of junctions stored at room temperature

Chip 1 was stored in a flow box under N_2 atmosphere between measurements to avoid degradation of the YBCO surface due to air humidity [28]. Subsequently, and repeatedly, the JJ properties have been measured. In the beginning, measurements were performed more frequently for a better resolution of the larger rate of change of JJ properties right after irradiation.

B. Annealing at elevated temperatures

To stabilize the JJ properties, we annealed samples for a certain time t_a in an oxygen partial pressure p_{O_2} . Annealing was performed in a vacuum (annealing) chamber with inlets for O_2 and N_2 , with the sample placed on a resistive

heating element with an integrated temperature sensor. A digital temperature controller OMRON E5AC was used to set and keep the sensor temperature T_a constant during annealing. After sample loading, the annealing chamber was evacuated to an absolute pressure < 0.1 mbar, then flooded with oxygen and evacuated to < 0.1 mbar again to flush the chamber and the pipes from the gas bottle to the annealing system. After this procedure, p_{O_2} was set to the desired value and the temperature was ramped up to $T_a = 90^\circ\text{C}$ with a rate of $20^\circ\text{C}/\text{min}$. Pristine YBCO remains unharmed at 90°C with no degradation even in vacuum [29].

After writing barriers into structure 2D, the chip 2 was annealed at $p_{O_2} = 950$ mbar for $t_a = 30$ min before the annealing chamber was flooded with O_2 to ambient pressure. Subsequently, the sample was placed onto a stainless steel plate for cooldown, outside the chamber in air. After completing measurements on structure 2D we wrote barriers into structure 2E and annealed chip 2 in vacuum. For this we just left the vacuum pump of the annealing chamber connected after the flushing procedure, i.e., during the subsequent annealing process for $t_a = 30$ min we had $p_{O_2} < 0.1$ mbar. Subsequently, we switched off the heater, vented the chamber with N_2 and then placed the sample onto a stainless steel plate for cooldown, outside the chamber in air.

Samples were measured directly after irradiation (at $t = 0$), have been annealed with the corresponding oxygen partial pressure at $t = 1$ day and measured subsequently all within 2 days. After this, the chip was stored under N_2 environment at room temperature and the junctions were repeatedly measured.

C. Evaluation of I - V characteristics

For junctions irradiated with $D \gtrsim 800$ ions/nm, i.e., close to the transition from medium to high dose (where amorphization sets in) [13], the I - V characteristics exhibit a $I \sim V^3$ contribution, in addition to a linear scaling $I \sim V$ (see Fig. 3), while for junctions with $D < 500$ ions/nm I - V characteristics exhibit an excess current I_{ex} . In order to consistently determine the normal state resistance R_n for all junctions, we applied an external magnetic field to suppress the critical current I_c and used the functional dependence

$$I(V) = aV^3 + \frac{V}{R_n} + \text{sgn}(V)I_{\text{ex}} \quad (1)$$

to fit all our measured I - V characteristics. Since I_c was never fully suppressed to zero, we discarded parts of the I - V characteristics where $|V| \leq 1$ mV for the evaluation of R_n . Here, the 1-mV criterion was used, as this was the typical voltage level, above which the I - V characteristics did coincide for any value of applied external magnetic field.

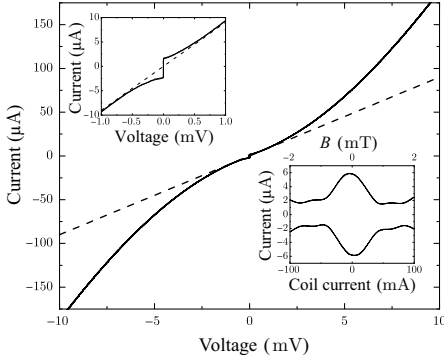


FIG. 3. I - V characteristics of junction 1A-1000 taken at the first minimum ($B \approx 0.94$ mT) of $I_c(B)$ after $t = 160$ days clearly bending away from an Ohmic resistance (dashed line) for larger voltages. The upper left inset shows an enlargement of the I - V characteristics at smaller voltages and currents. The lower right inset shows a measurement of $I_c(B)$. The bottom axis refers to the applied coil current and the top axis is the calculated magnetic field from the experimentally determined coil constant by using a Hall probe.

The maximum critical current $I_{c,\max}$ for each junction was determined from the maximum of the recorded $I_c(B)$ curves. Note that due to thermal noise rounding, the experimentally determined $I_{c,\max}$ can be significantly suppressed below the noise-free maximum critical current I_0 . From numerical simulations of overdamped JJs within the resistively and capacitively shunted junction (RCSJ) model, one knows that for a noise parameter $\Gamma \equiv I_{\text{th}}/I_0 = 0.05$, with $I_{\text{th}} = 2\pi k_B T/\Phi_0$, $I_{c,\max}$ of a nonhysteretic junction is suppressed by approximately 10% (Φ_0 is the magnetic flux quantum and k_B is the Boltzmann constant) [30]. With $I_{\text{th}} \approx 176$ nA at $T = 4.2$ K, a noise parameter $\Gamma = 0.05$ corresponds to $I_0 \approx 3.5$ μ A, i.e., significant noise rounding is only expected for JJs with critical currents below a few μ A, which is only relevant for the junction 1A-1000, for which the measured $I_{c,\max}$ is a lower bound.

IV. RESULTS AND DISCUSSION

Now we discuss and analyze the evolution of the electric transport properties of He-FIB JJs with time. Note that unless stated otherwise, for simplicity, we denote now the maximum (with respect to variable magnetic field B) critical current as I_c and the corresponding maximum critical current density as $j_c = I_c/wd$.

A. Temporal evolution of electric transport properties of He-FIB JJs stored at room temperature

Here, we present results on He-FIB JJs, which were stored at room temperature. Figure 4 shows the time

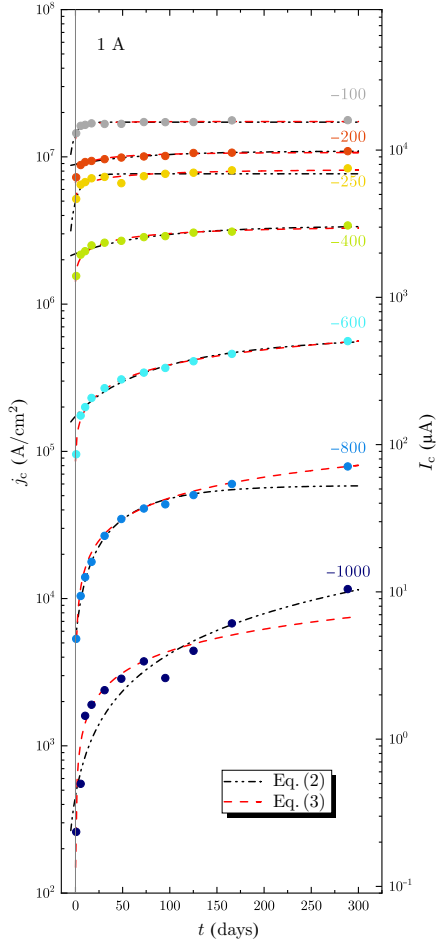


FIG. 4. Time dependence of the critical current density $j_c(t)$ (right axis: critical current I_c) for junctions from 1A-100 to 1A-1000 and stored at room temperature. The dash-dotted and dashed lines show fits to the experimental data (symbols), obtained from Eqs. (2) and (3), respectively.

dependence of the critical current density $j_c(t)$ of the seven JJs 1A-100 to 1A-1000 located in structure 1A over 160 days after irradiation. Obviously, j_c is largest for the JJ irradiated with the lowest dose $D = 100$ ions/nm (top curve in Fig. 4) and smallest for the JJ irradiated with the

highest dose $D = 1000$ ions/nm (bottom curve in Fig. 4). We find a monotonous increase in $j_c(t)$, which tends to saturate for long enough times. However, we also see a clear dose dependence in the evolution of $j_c(t)$. For the lowest dose (junction 1A-100), already after a few days j_c saturates. With increasing dose (junctions 1A-200 to 1A-400), the time until saturation of j_c is reached steadily increases, and for the highest doses (junctions 1A-600 to 1A-1000) $j_c(t)$ has not saturated at $t = 288$ days.

To fit the experimental data we used two different equations

$$j_c(t) = j_{c,\infty} \left[1 - b \exp\left(-\frac{t}{\tau}\right) \right]; \quad \text{and} \quad (2)$$

$$j_c(t) = j_{c,\infty} \left[1 - b \exp\left(-\sqrt{\frac{t}{\tau}}\right) \right]. \quad (3)$$

Here $j_{c,\infty}$ is the saturation (equilibrium) value of the critical current, which is achieved for $t \rightarrow \infty$. This parameter can be associated with unrecoverable damage in the barrier region induced by He-FIB irradiation. The dimensionless parameter $b = (j_{c,\infty} - j_{c,0})/j_{c,\infty}$ [with $j_{c,0} \equiv j_c(t=0)$] describes the degree of nonequilibrium damage that was created by He-FIB irradiation and which can still be recovered with time (by annealing). $b = 0$ means that we are at equilibrium already at $t = 0$ and there is nothing to recover. $b = 1$ means that the He-FIB irradiation initially completely suppresses the critical current density, i.e., $j_{c,0} = 0$, but with time finite j_c will appear. The parameter τ describes the characteristic time scale (relaxation time) that governs relaxation of the system to the equilibrium state. The two formulas are similar, but Eq. (2) describes the changes in j_c due to a *constant flux* of oxygen atoms diffusing towards the barrier, while Eq. (3) describes the *diffusion* of a limited amount of oxygen atoms towards the barrier. Equation (2) assumes that the sample is placed in a oxygen atmosphere and the oxygen atoms diffuse into the barrier from the outside; instead Eq. (3) assumes that oxygen atoms that have been displaced during He-FIB irradiation diffuse back similar to Einstein diffusion. By using Eqs. (2) and (3) to fit the data shown in Fig. 4, we conclude that Eq. (3) allows to fit the experimental data more consistently at smaller times for devices irradiated with higher doses.

As a result of fitting with Eq. (3) we obtain the dose dependence of the fitting parameters $j_{c,\infty}$, b , and τ as shown in Fig. 5. For $j_{c,\infty}$ we find an exponential decay with increasing dose [see Fig. 5(a)], i.e.,

$$j_{c,\infty}(D) \approx j_{c,\infty}(0) \exp(-D/D_0), \quad (4)$$

with $j_{c,\infty}(0) = 3.2 \times 10^7$ A/cm² and $D_0 = 191$ ions/nm. The value for $j_{c,\infty}(0)$ corresponds to the critical current density of unirradiated YBCO films at 4.2 K; this

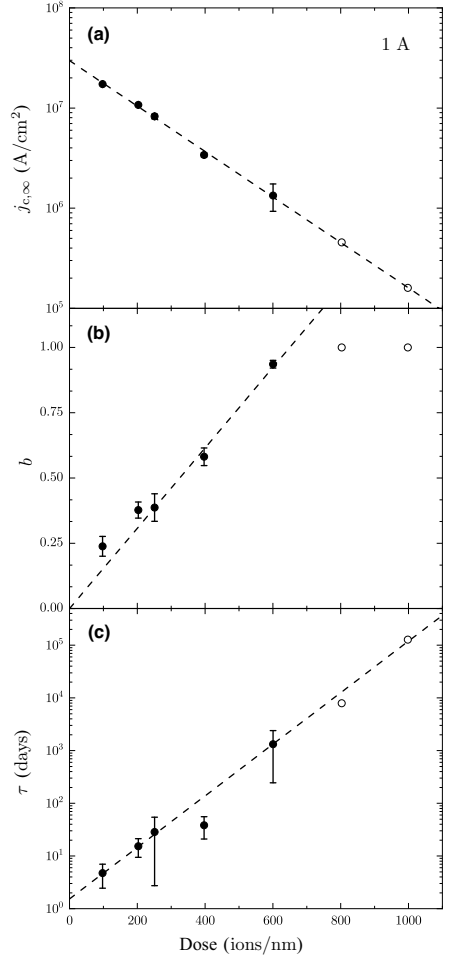


FIG. 5. Dose dependence of the parameters $j_{c,\infty}$ (a), b (b), and τ (c) extracted from the fits with Eq. (3) to $j_c(t)$ data shown in Fig. 4. For the two highest dose values, the $j_{c,\infty}$ values [open symbols in (a)] have been fixed for the fitting procedure to obtain b and τ [31]. The confidence intervals provided by the fitting algorithm are shown as error bars.

coincides quite well with the corresponding value given in Ref. [13]. The value for the characteristic dose D_0 obtained in the present study is slightly higher than the

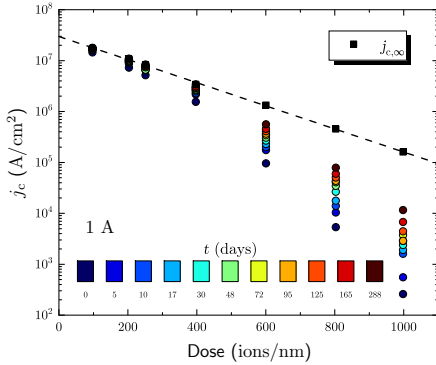


FIG. 6. Experimentally determined critical current density j_c versus irradiation dose D for junctions from 1A, measured at different times t after irradiation (indicated by the color scale). For comparison the fit parameter $j_{c,\infty}(D)$ is shown as black squares.

value $D_0 = 130$ ions/nm found for the exponential scaling of $j_c(D)$ (measured at some finite t) for YBCO He-FIB JJs on SrTiO₃ (STO) or MgO substrates and significantly higher than $D_0 = 38$ ions/nm found for YBCO He-FIB JJs on a LSAT substrate [13]. The reason for the low value of $D_0 = 38$ ions/nm on LSAT in Ref. [13] has not yet been clarified. We note that we observe the tendency that for our YBCO He-FIB JJs produced on the same chip (typically on LSAT substrates), we always find an exponential decay of $j_c(D)$ with a well-defined D_0 . However, the value of D_0 can vary significantly from chip to chip. Currently, it is not clear whether D_0 is related to and affected by the YBCO film quality or by the conditions in the helium ion microscope. What is obvious from the study presented here is the fact that D_0 is also affected by the time t (samples stored at room temperature) after He-FIB irradiation. This is illustrated in Fig. 6, which shows the same experimental data (dots) as in Fig. 4, but now plotted as $j_c(D)$ for different values of t , together with $j_{c,\infty}(D)$ (squares) from Fig. 5(a). Clearly, with increasing t the slope $|\partial \log j_c / \partial D|$ decreases, i.e., D_0 increases, approaching asymptotically the scaling of $j_{c,\infty}(D)$. Thus, experimentally measured $j_c(D)$ tends to decrease the slope with time and becomes more straight.

The scaling of $b(D)$, shown in Fig. 5(b), is approximately linear for $D \lesssim 600$ ions/nm and saturates to $b \approx 1$ for larger D . In the latter case, the permanent and nonequilibrium damage make $j_{c,0} = 0$. However, if one removes nonequilibrium damage by storing at room temperature, j_c recovers to some finite value, which is caused by permanent damage only.

Obviously, the characteristic time for recovery increases with D . This is illustrated in Fig. 5(c), which shows that

the time constant τ increases exponentially with dose and can be described by

$$\tau(D) \approx \tau_0 \exp(D/D_{0,\tau}), \quad (5)$$

with $\tau_0 = 1$ day and $D_{0,\tau} = 89$ ions/nm. Interestingly, the value of $D_{0,\tau}$ is not far from half of the value of D_0 . However, it is not clear whether or not this is just a coincidence. Still, it is worthwhile to note that for typical doses required to create RCSJ-like Josephson junctions without an excess current, i.e., $D \gtrsim 500$ ions/nm, the value of $\tau \gtrsim 100$ days. This means that the properties of junctions produced with such doses change over significant time scales of up to a year, if they are stored at room temperature.

In addition to $j_c(t)$ shown in Fig. 4, we also measured the time evolution $R_n(t)$ and calculated $\rho_n(t)$ (not shown). This allows us to calculate $V_c(t) = j_c(t)\rho_n(t)$ and its evolution during annealing, see Fig. 7. In Ref. [13] we showed that the exponential scaling of characteristic He-FIB JJ properties (j_c , $\rho_n = R_n w d$ and the characteristic voltage $V_c \equiv I_c R_n \equiv j_c \rho_n$) with D can be described by the same values of D_0 , indicating a universal scaling of V_c with either j_c or ρ_n , and we found an approximate scaling $V_c \approx V_{c,1}(j_c/j_{c,1})^{1/2}$. Now, for the He-FIB JJs described here, we find the same scaling $V_c \propto j_c^{1/2}$, as shown in Fig. 7. Note that this is not only true for the junctions measured directly after irradiation, but also for junctions stored at room temperature and remeasured over the whole time of the experiment (up to $t = 288$ days), i.e., for the same junction, the data points move with t along the $V_c \propto j_c^{1/2}$ line. The data points for the He-FIB JJs 1A-400, 1A-600, and 1A-800 follow the

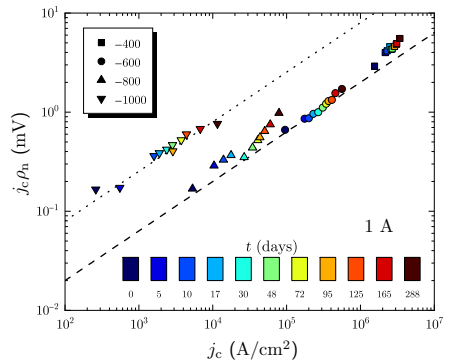


FIG. 7. $j_c \rho_n$ versus j_c for He-FIB JJs (from 1A) stored at room temperature and measured at different times t after irradiation (indicated by the color scale). The dashed and dotted lines represent $j_c \rho_n = V_{c,1} \sqrt{j_c/j_{c,1}}$, with $V_{c,1} = 2$ and 8 mV, respectively ($j_{c,1} = 10^6$ A/cm²).

same scaling with $V_{c,1} = 2$ mV and $j_{c,1} = 10^6$ A/cm² as reported in Ref. [13]. However the data points for junction 1A-1000 with $D = 1000$ ions/nm show a significant offset, i.e., they also show the scaling $V_c \propto j_c^{1/2}$, but now with a factor of 4 larger $V_{c,1} = 8$ mV and $j_{c,1} = 10^6$ A/cm². In conclusion, we observed an increase in the critical current density, respectively, a decrease in the resistivity, over time when devices were stored at room temperature. With our diffusion-based model, a reasonable explanation is, that oxygen atoms displaced during irradiation to interstitial lattice sites are diffusing back to their original position, healing the barrier and thus the critical current density increases.

B. Temporal evolution of electric transport properties of He-FIB JJs that were annealed after irradiation

The temporal evolution of the critical current density of He-FIB JJs from structure 2D is presented in Fig. 8. Those junctions have been annealed twice (at 90 °C) in oxygen ($p_{O_2} = 950$ mbar) for 30 min at day 1 and day 41 (j_c measurements on day 1 and 41 have been performed after annealing). Annealing the junctions at day 1 caused an increase in j_c and a decrease in ρ_n , respectively, just after the annealing step. After 1 week the critical currents were reduced, but still maintained higher values than obtained directly after irradiation. In the following weeks j_c did not change significantly, indicating that the junctions have reached a quasistable state. On day 41 we repeated the same annealing procedure with the already annealed junctions. The temporal evolution of j_c showed qualitatively the same behavior as after the first annealing step, however j_c values are higher and there seems to appear now a short

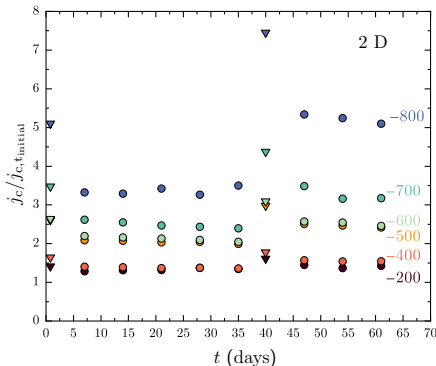


FIG. 8. Temporal evolution of the critical current density j_c (normalized to j_c at $t = t_{\text{initial}}$) of He-FIB JJs from 2D, which were annealed at 90 °C for 30 min in $p_{O_2} = 950$ mbar.

but finite relaxation time until another quasistable state has been reached.

In Fig. 9, the data from Fig. 8 are plotted against the dose D for substantial points in time, namely after irradiation ($t = t_{\text{initial}}$) and for both quasistable states after relaxation following the first and second annealing step ($t = 21$ and 61 days, respectively). We find, that with comparable initial critical current densities (right after He-FIB irradiation), the first annealing step increased j_c equivalently to roughly 100 days of storing at room temperature, while the second annealing step produced another increase in j_c , albeit at a moderate level. Moreover, the junctions after annealing do not exhibit a significant further change in j_c with time (cf. Fig. 8), which one would expect if following the time evolution shown in Fig. 4, but remained unchanged in their electric transport properties. This clearly indicates that moderate thermal annealing after He-FIB irradiation clearly stabilizes the irradiation-induced defect structure.

Similar to the graph in Fig. 7 the overall scaling $V_c(j_c)$ for the annealed junctions is shown in Fig. 10. As the junctions stored at room temperature, the annealed junctions follow the same $V_c \propto j_c^{1/2}$ scaling indicated by the dotted and dashed lines. In addition one can see that the higher-dose junctions are shifted towards higher characteristic voltages for the same critical current density.

For comparison, and to rule out the possibility that the increase in j_c shortly after annealing is caused by the high oxygen pressure in the annealing chamber during the

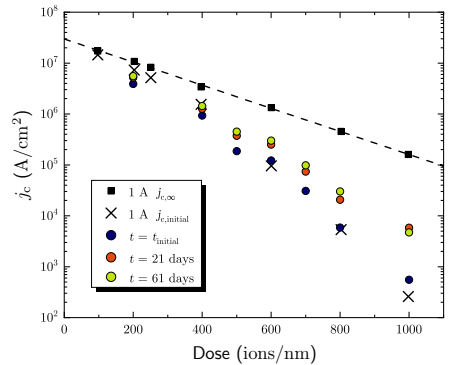


FIG. 9. Critical current density j_c versus irradiation dose D for He-FIB JJs from 2D (annealed at 90 °C for 30 min in $p_{O_2} = 950$ mbar), measured at substantial times ($t = t_{\text{initial}}$, 21 days and 61 days). For comparison, we show results from JJs from 1A—stored at room temperature—for the initial critical current density (black crosses) and $j_{c,\infty}(D)$ (dashed line and black squares).

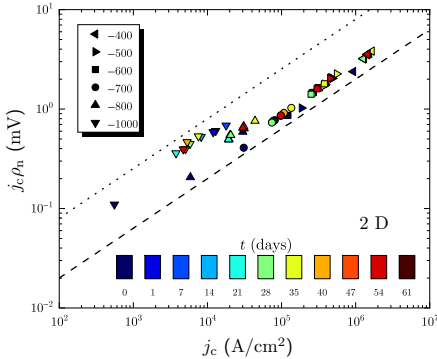


FIG. 10. $j_c \rho_n$ versus j_c for He-FIB JJs from 2D annealed at 90 °C for 30 min in $p_{O_2} = 950$ mbar. The dashed and dotted lines represent $j_c \rho_n = V_{c,1} \sqrt{j_c / j_{c,1}}$, with $V_{c,1} = 2$ and 8 mV, respectively ($j_{c,1} = 10^6$ A/cm²).

treatment, we performed annealing of He-FIB JJs from structure 2E at $p_{O_2} < 0.1$ mbar. Here, we could not observe a substantial difference of the temporal evolution of j_c as compared to junctions annealed at $p_{O_2} = 950$ mbar. This observation indicates, that the restoring of critical current density with annealing (or also simply by storing at room temperature) is due to the diffusion of oxygen atoms that have been displaced (probably to interstitial sites) by He-FIB irradiation and that are diffusing back to lattice sites. Obviously, the annealing process significantly speeds up the relaxation (back diffusion) to a quasistable state with stable electric transport properties.

V. CONCLUSIONS

We fabricated Josephson barriers in prepatterned 3- μ m-wide microbridges of epitaxially grown YBCO thin films by scanning a focused He ion beam across the bridges, which locally modifies the superconducting properties of the thin film. In detail, we studied the temporal evolution of characteristic junction properties for devices stored at room temperature and found that this process can be best described by a diffusion-based model, corresponding to a limited amount of oxygen diffusing back towards the barrier. Moreover, fitting of the experimentally observed temporal evolution of critical current density with time, allowed us to extract the dose dependence of the fitting parameters $j_{c,\infty}$, b and τ . For high-quality junctions, corresponding to doses in the range of 600–800 ions/nm, the relaxation time is typically $\tau \sim 100$ –1000 days, exceeding any feasible timescale to wait for the equilibrium state. The analysis of the characteristic voltages V_c of the fabricated

devices yield a scaling $V_c \propto \sqrt{j_c}$, also reported in previous work [13], but now this scaling holds true even for junctions stored at room temperature over the whole time of the experiment.

Furthermore, we examined the behavior of devices when treated with an annealing step at high oxygen pressures. Directly after the treatment the critical current density j_c increased before relaxing into a quasistable state within the first week. A repeated annealing step increased j_c only marginally, but indicated a slightly larger relaxation time of roughly 2 weeks. In comparison to junctions stored at room temperature, the annealing process accelerated the increase in j_c to roughly an equivalent of 100 days storing at room temperature. Additionally, for annealing at low oxygen pressures we did not observe any substantial differences in the behavior of the annealed devices annealed at high oxygen pressure. This indicates that predominantly the oxygen atoms displaced during He-FIB irradiation are diffusing back towards the original lattice sites.

Although some enigma remains to be examined in further studies, we revealed how characteristic properties of He-FIB JJs in YBCO evolve with time when stored at room temperature and confirmed a strategy to stabilize their properties. The stabilization of device parameters after annealing is expected to result in smaller spread (in particular, over time) and improved device uniformity. This in turn will significantly support the development of complex multijunction circuits (e.g., for digital applications) with different j_c (produced by different dose values) yielding e.g., better operation margins. So far, we have not systematically varied the annealing procedure, and there might still be room for improvements. In particular, one might implement an *in situ* annealing procedure with the He-FIB circuit fabrication process by utilizing the heating stage of the Orion NanoFab. We anticipate that such an *in situ* process might provide stable parameters immediately following the He-FIB irradiation, thus further increasing the feasibility of this technology.

ACKNOWLEDGMENTS

We gratefully acknowledge technical support by M. Turad, R. Löffler (LISA⁺), C. Back, and R. Schilling. This work was supported by the Deutsche Forschungsgemeinschaft (DFG) (GO 1106/6-1), by the European Commission under H2020 FET Open Grant “FIBsuperProbes” (Grant No. 892427) and by the COST actions FIT4NANO (CA19140) and SUPERQUMAP (CA21144).

[1] D. Koelle, R. Kleiner, F. Ludwig, E. Dantsker, and J. Clarke, High-transition-temperature superconducting quantum interference devices, *Rev. Mod. Phys.* **71**, 631 (1999).

- [2] F. Ludwig, D. Koelle, E. Dantsker, D. Nemeth, A. Miklich, J. Clarke, and R. Thomson, Low noise $\text{YBa}_2\text{Cu}_3\text{O}_{7-x}$ - SrTiO_3 - $\text{YBa}_2\text{Cu}_3\text{O}_{7-x}$ multilayers for improved magnetometers, *Appl. Phys. Lett.* **66**, 373 (1995).
- [3] H. Hilgenkamp and J. Mannhart, Grain boundaries in high- T_c superconductors, *Rev. Mod. Phys.* **74**, 485 (2002).
- [4] R. Gross, L. Alff, A. Beck, O. Froehlich, D. Koelle, and A. Marx, Physics and technology of high temperature superconducting Josephson junctions, *IEEE Trans. Appl. Supercond.* **7**, 2929 (1997).
- [5] S. S. Tinchev, Investigation of RF SQUIDS made from epitaxial YBCO films, *Supercond. Sci. Technol.* **3**, 500 (1990).
- [6] S. K. Tolpygo, S. Shokhor, B. Nadgorny, J.-Y. Lin, M. Gurvitch, A. Bourdillon, S. Y. Hou, and J. M. Phillips, High quality $\text{YBa}_2\text{Cu}_3\text{O}_7$ Josephson junctions made by direct electron beam writing, *Appl. Phys. Lett.* **63**, 1696 (1993).
- [7] W. E. Booij, A. J. Pauza, E. J. Tarte, D. F. Moore, and M. G. Blamire, Proximity coupling in high- T_c Josephson junctions produced by focused electron beam irradiation, *Phys. Rev. B* **55**, 14600 (1997).
- [8] D.-J. Kang, G. Burnell, S. J. Lloyd, R. S. Speaks, N. H. Peng, C. Jaynes, R. Webb, J. H. Yun, S. H. Moon, B. Oh, E. J. Tarte, D. F. Moore, and M. G. Blamire, Realization and properties of $\text{YBa}_2\text{Cu}_3\text{O}_{7-\delta}$ Josephson junctions by metal masked ion damage technique, *Appl. Phys. Lett.* **80**, 814 (2002).
- [9] N. Bergeal, J. Lesueur, M. Sirena, G. Faini, M. Aprili, J. P. Contour, and B. Leridon, Using ion irradiation to make high- T_c Josephson junctions, *J. Appl. Phys.* **102**, 083903 (2007).
- [10] B. W. Ward, J. A. Notte, N. P. Economou, and Helium ion microscope, A new tool for nanoscale microscopy and metrology, *J. Vac. Sci. Technol. B: Microelectron. Nanometer Struct.* **24**, 2871 (2006).
- [11] S. A. Cybart, E. Y. Cho, J. T. Wong, B. H. Wehlin, M. K. Ma, C. Huynh, and R. C. Dynes, Nano Josephson superconducting tunnel junctions in $\text{YBa}_2\text{Cu}_3\text{O}_{7-\delta}$ directly patterned with a focused helium ion beam, *Nat. Nano* **10**, 598 (2015).
- [12] E. Y. Cho, Y. W. Zhou, J. Y. Cho, and S. A. Cybart, Superconducting nano Josephson junctions patterned with a focused helium ion beam, *Appl. Phys. Lett.* **113**, 022604 (2018).
- [13] B. Müller, M. Karrer, F. Limberger, M. Becker, B. Schröppel, C. J. Burkhardt, R. Kleiner, E. Goldobin, and D. Koelle, Josephson junctions and SQUIDS created by focused helium-ion-beam irradiation of $\text{YBa}_2\text{Cu}_3\text{O}_7$, *Phys. Rev. Appl.* **11**, 044082 (2019).
- [14] F. Couëdo, P. Amari, C. Feuillet-Palma, C. Ulysse, Y. K. Srivastava, R. Singh, N. Bergeal, and J. Lesueur, Dynamic properties of high- T_c superconducting nano-junctions made with a focused helium ion beam, *Sci. Rep.* **10**, 021001 (2020).
- [15] Z. Chen, Y. Li, R. Zhu, J. Xu, D. Y. T. Xu, X. Cai, Y. Wang, J. Lu, Y. Zhang, and P. Ma, High-temperature superconducting $\text{YBa}_2\text{Cu}_3\text{O}_{7-\delta}$ Josephson junction fabricated with a focused helium ion beam, *Chin. Phys. Lett.* **39**, 077402 (2022).
- [16] R. L. Merino, P. Seifert, J. D. Retamal, R. K. Mech, T. Taniguchi, K. Watanabe, K. Kadowaki, R. H. Hadfield, and D. Efetov, Two-dimensional cuprate nanodetector with single telecom photon sensitivity at $T = 20$ K, *2D Mater.* **10**, 10256 (2023).
- [17] J. F. Ziegler, M. D. Ziegler, and J. P. Biersack, SRIM—the stopping power and range of ions in matter, *Instrum. Methods Phys. Res., Sect. B* **268**, 1818 (2010).
- [18] F. Z. Cui, J. Xie, and H. D. Li, Preferential radiation damage of the oxygen sublattice in $\text{YBa}_2\text{Cu}_3\text{O}_7$: A molecular-dynamics simulation, *Phys. Rev. B* **46**, 11182 (1992).
- [19] W. Lang, M. Marksteiner, M. A. Bodea, K. Siraj, J. D. Pedarnig, R. Kolarova, P. Bauer, K. Haselgrübler, C. Hasenfuss, I. Beinik, and C. Teichert, Ion beam irradiation of cuprate high-temperature superconductors: Systematic modification of the electrical properties and fabrication of nanopatterns, *Nucl. Instr. Meth. Phys. B* **272**, 300 (2012).
- [20] K. L. Mletschnig and W. Lang, Nano-patterning of cuprate superconductors by masked He^+ ion irradiation: 3-dimensional profiles of the local critical temperature, *Microelectron. Eng.* **215**, 110982 (2019).
- [21] B. Aichner, K. L. Mletschnig, M. Dosmailov, V. R. Misko, F. Limberger, K. L. Mletschnig, M. Dosmailov, J. D. Pedarnig, F. Nori, R. Kleiner, D. Koelle, and W. Lang, Ultradense tailored vortex pinning arrays in superconducting $\text{YBa}_2\text{Cu}_3\text{O}_{7-\delta}$ thin films created by focused he ion beam irradiation for fluxonics applications, *ACS Appl. Nano Mater.* **2**, 5108 (2019).
- [22] B. Aichner, K. L. Mletschnig, B. Müller, M. Karrer, M. Dosmailov, J. D. Pedarnig, R. Kleiner, D. Koelle, and W. Lang, Angular magnetic-field dependence of vortex matching in pinning lattices fabricated by focused or masked helium ion beam irradiation of superconducting $\text{YBa}_2\text{Cu}_3\text{O}_{7-\delta}$ thin films, *Low Temp. Phys.* **46**, 331 (2020).
- [23] E. Y. Cho, K. Kouperine, Y. Zhuo, R. C. Dynes, and S. A. Cybart, The effects of annealing a 2-dimensional array of ion-irradiated Josephson junctions, *Supercond. Sci. Technol.* **29**, 094004 (2016).
- [24] A. Katz, S. Woods, R. Dynes, and A. Sun, Stability and uniformity of planar high temperature Josephson junctions fabricated using nanolithography and ion damage, *IEEE Trans. Appl. Supercond.* **9**, 3005 (1999).
- [25] S. A. Cybart, P. Roediger, K. Chen, J. M. Parker, E. Y. Cho, T. J. Wong, and R. C. Dynes, Temporal stability of Y–Ba–Cu–O nano Josephson junctions from ion irradiation, *IEEE Trans. Appl. Supercond.* **23**, 1100103 (2013).
- [26] H. Hochmuth and M. Lorenz, Inductive determination of the critical current density of superconducting thin films without lateral structuring, *Physica C* **220**, 209 (1994).
- [27] A. M. Miller, M. Lemon, M. A. Choffel, S. R. Rich, F. Harvel, and D. C. Johnson, Extracting information from x-ray diffraction patterns containing Laue oscillations, *Z. Naturforsch. B* **77**, 313 (2022).
- [28] M. W. Hooker, S. A. Wise, I. A. Carlberg, R. M. Stephens, R. T. Simchick, and A. Farjami, Room temperature degradation of $\text{YBa}_2\text{Cu}_3\text{O}_{7-x}$ superconductors in varying relative humidity environments, Technical Paper number 3368 (NASA, 1993).
- [29] A. Mogro-Campero, K. W. Paik, and L. G. Turner, Degradation of thin films of $\text{YBa}_2\text{Cu}_3\text{O}_7$ by annealing in air and in vacuum, *J. Supercond.* **8**, 95 (1995).
- [30] B. Chesca, R. Kleiner, and D. Koelle, in *The SQUID Handbook*, Vol. 1, Fundamentals and Technology of SQUIDS

and SQUID systems, edited by J. Clarke and A. I. Braginski (Wiley-VCH, Weinheim, 2004) Chapter 2, p. 29.

- [31] For the two highest dose values $D = 800$ and 1000 ions/nm, the $j_c(t)$ data shown in Fig. 4 were at $t = 288$ days still far from saturation. Therefore, the values of $j_{c, \infty}$ determined from the fit have huge uncertainties, i.e., one can fit the

experimental data quite well with many combinations of $j_{c, \infty}$ and τ . Therefore, for the two highest doses the $j_{c, \infty}$ values [open symbols in Fig. 5(a)] have been fixed by hand so that they lay exactly on the line shown in Fig. 5(a) (open circles). After fixing $j_{c, \infty}$ for the highest two D values, the parameters b and τ were calculated from the fits of $j_c(t)$.

Publication 3

Reprinted with permission from
B. Aichner et al., ACS Applied Nano Materials **2**, 5108 (2019)
Copyright © 2019 American Chemical Society.

Ultradense Tailored Vortex Pinning Arrays in Superconducting $\text{YBa}_2\text{Cu}_3\text{O}_{7-\delta}$ Thin Films Created by Focused He Ion Beam Irradiation for Fluxonics Applications

Bernd Aichner,[†] Benedikt Müller,[‡] Max Karrer,[‡] Vyacheslav R. Misko,^{§,||,⊥} Fabienne Limberger,[‡] Kristijan L. Mletschnig,[†] Meirzhan Dosmailov,[#] Johannes D. Pedarnig,[#] Franco Nori,^{||,§} Reinhold Kleiner,[‡] Dieter Koelle,[‡] and Wolfgang Lang^{*,†,⊥}

[†]Faculty of Physics, University of Vienna, Wien, Austria

[‡]Physikalisches Institut und Center for Quantum Science (CQ) in LISA⁺, Universität Tübingen, Tübingen, Germany

[§]Department of Physics, Universiteit Antwerpen, Antwerpen, Belgium

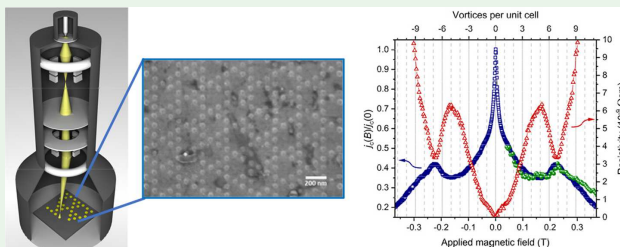
^{||}Theoretical Quantum Physics Laboratory, RIKEN Cluster for Pioneering Research, Wako-shi, Saitama, Japan

[⊥] μ Flow group, Department of Chemical Engineering, Vrije Universiteit Brussel, Brussels, Belgium

[#]Institute of Applied Physics, Johannes Kepler University Linz, Linz, Austria

^{*}Physics Department, University of Michigan, Ann Arbor, Michigan 48109, United States

Supporting Information



ABSTRACT: Magnetic fields penetrate a type II superconductor as magnetic flux quanta, called vortices. In a clean superconductor they arrange in a hexagonal lattice, while by addition of periodic artificial pinning centers many other arrangements can be realized. Using the focused beam of a helium ion microscope, we have fabricated periodic patterns of dense pinning centers with spacings as small as 70 nm in thin films of the cuprate superconductor $\text{YBa}_2\text{Cu}_3\text{O}_{7-\delta}$. In these ultradense kagomé-like patterns, the voids lead to magnetic caging of vortices, resulting in unconventional commensurability effects that manifest themselves as peaks in the critical current and minima in the resistance versus applied magnetic field up to ~ 0.4 T. The various vortex patterns at different magnetic fields are analyzed by molecular dynamics simulations of vortex motion, and the magnetic field dependence of the critical current is confirmed. These findings open the way for a controlled manipulation of vortices in cuprate superconductors by artificial sub-100 nm pinning landscapes.

KEYWORDS: helium ion microscope, cuprate superconductor, vortex pinning lattice, commensurability effects, critical current

1. INTRODUCTION

Superconductivity is one of the most intriguing phenomena in condensed matter physics, and in particular the cuprate superconductors pose a challenge to the understanding of their electron-pairing mechanism. Still, their high transition temperature T_c and their possible high operating temperature in the accessible range of reliable and easy-to-handle cryocooler technology make the cuprate superconductors primary candidates for emerging technologies. However, all superconductors are only marginally suitable for technical

applications in their pure and clean form. It is by the introduction of controlled defects that superconductors can be tailored for many important properties, e.g., by enhancing their ability to carry a lossless current, which requires to impede the dissipative motion of magnetic flux quanta, also called Abrikosov vortices or fluxons.¹

Received: May 28, 2019

Accepted: July 10, 2019

Published: July 10, 2019

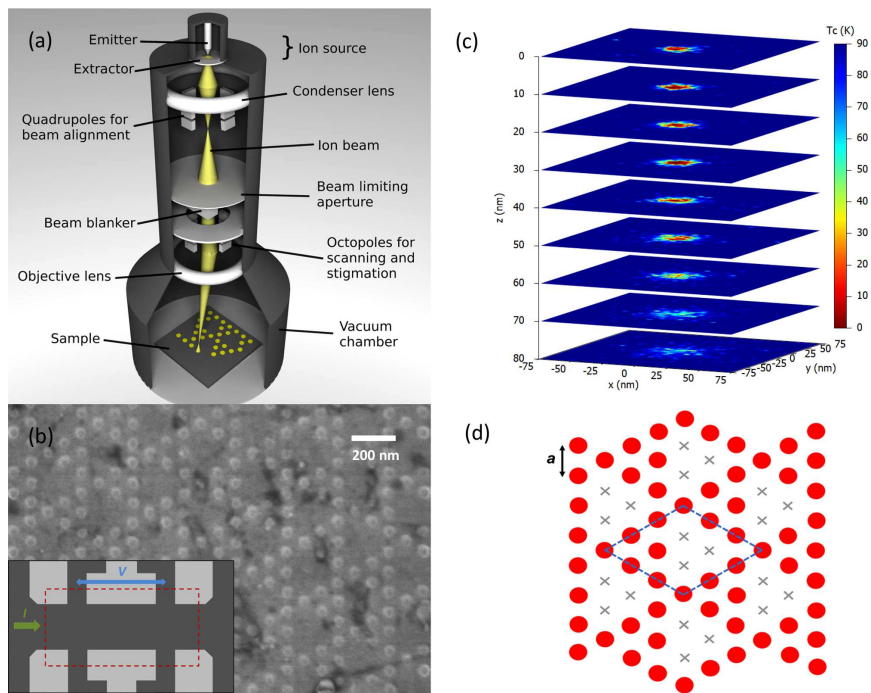


Figure 1. (a) Schematic drawing of direct modification of the local superconducting properties in a HIM. (b) HIM image of a quasi-kagomé test pattern of HIM-induced defects in a YBCO film, irradiated with a fully focused beam and with 5×10^6 ions/spot, i.e., with a 333 times larger number than in (c). The lattice spacing is $a = 90$ nm. Inset: sketch of the YBCO thin film samples (dark gray), the $200 \mu\text{m} \times 100 \mu\text{m}$ rectangular irradiated area (red broken lines), direction of the applied current I , and the voltage probes V . (c) Simulation of defect-induced spatial distribution of T_c of a YBCO film (within sheets at various depths z from the surface $z = 0$), upon irradiating one spot with a defocused 30 keV He^+ ion beam with a Gaussian normal distributed fluence of 20 nm fwhm diameter. The number of impacting ions (15000) is the same as in the experiments (per spot) and corresponds to an average fluence of $4.8 \times 10^{15} \text{cm}^{-2}$. (d) Sketch of the pinning lattice with lattice spacing a : red disks represent irradiated spots, the blue dashed lines indicate the unit cell of the quasi-kagomé tiling, and gray crosses mark those sites that were removed from the hexagonal lattice to form the quasi-kagomé tiling.

Whereas such enhanced vortex pinning in conventional metallic superconductors, typically used for medical applications and high-field magnets, has been achieved by metallurgical techniques, the brittle nature of cuprate high- T_c superconductors (HTSCs) requires different concepts. A successful approach is to create columnar amorphous regions with diameters of a few times the superconducting coherence length by irradiation with swift heavy ions.²

In contrast to these extended defects, point defects can be created by inclusion of tiny nonsuperconducting particles³ or by electron, proton, and light ion irradiation of HTSCs. For energies up to few mega-electronvolts the incident particles collide with a nucleus and displace it, eventually creating a collision cascade for high enough recoil energies. Several studies^{4–6} have revealed that irradiation with He^+ ions of moderate energy is well suitable to tailor the superconducting properties in thin films of the prototypical HTSC $\text{YBa}_2\text{Cu}_3\text{O}_{7-\delta}$ (YBCO) by displacing mainly oxygen atoms,

leading to a controllable reduction or even complete suppression of T_c . Arrays of cylindrical defect channels (CDs) that are populated with point defects provide a landscape in which superconductivity is locally suppressed. Recently, it has been demonstrated^{7–14} that such pinning potential landscapes allow one to accommodate vortices in a commensurate arrangement, leading to peaks in the critical current and minima of the resistance at well-defined matching magnetic fields.

In the field of vortex commensurability effects, a large body of research has been established for metallic superconductors, typically using an array of holes (antidots) or blind holes with about $1 \mu\text{m}$ spacings.¹⁵ Considerably narrower spacings have been achieved for thin Nb films grown on porous substrates.^{16,17} However, in these superconductors, the Ginzburg–Landau coherence length at zero temperature is on the order of $\xi(0) \sim 10$ nm and the London penetration depth on the order of $\lambda_L(0) \sim 100$ nm, the latter setting the

range of magnetic interaction between vortices. Commensurability effects could be explored only at temperatures T very close to T_c , taking advantage of the fact that $\lambda_L(T) = \lambda_L(0)[T_c/(T_c - T)]^{1/2}$ increases substantially when approaching T_c . But choosing a rather high operation temperature is not feasible for practical applications since it is on the expense of a reduced superconducting gap, weaker pinning potential, and enhanced thermodynamic fluctuations.

On the other hand, thin films of YBCO have an in-plane $\lambda_{L,ab}(0) \sim 250$ nm,^{18–21} and edge and screw dislocations, as one important type of intrinsic defects in YBCO films, have typical distances of about 300 nm.²² Still, commensurability effects could be demonstrated close to T_c in YBCO perforated with a square array of holes with $1 \mu\text{m}$ lattice spacing.²³ But since intrinsic defects compete with the artificially created pinning landscape, it is important to fabricate and investigate pinning arrays with lattice spacings significantly below these two characteristic lengths. Here, we report on the electrical transport properties of ultradense unconventional pinning arrays in YBCO thin films with spacings down to 70 nm, fabricated with a helium ion microscope, and we demonstrate pronounced commensurability effects at strong magnetic fields well above 100 mT which persist down to at least ~ 50 K, i.e., far below T_c .

2. RESULTS AND DISCUSSION

2.1. Irradiation in the Helium Ion Microscope. The ZEISS ORION NanoFab²⁴ is a novel multifunctional platform combining focused ion beam sources for neon and helium ions and a scanning helium ion microscope (HIM) with a spatial resolution better than 0.5 nm and unprecedented depth of focus.^{25–27} The HIM consists of a gas-field He^+ ion source that emits ions from an ultrasharp tip, electrostatic ion optics to focus and trim the beam, and a deflection system to raster the beam over the sample stage as it is outlined in Figure 1a. The advantage of using a He beam over the conventional Ga focused ion beam technique is its higher spatial resolution (fabrication of nanopores down to 1.3 nm has been demonstrated²⁸) and the prevention of contamination of the HTSC by Ga ions. As a first application in YBCO, the fabrication of Josephson junctions and superconducting quantum interference devices has been demonstrated via forming thin barriers of insulating material with the focused ion beam across prepatterned microbridges.^{29–32}

However, for the fabrication of vortex pinning defects, the HIM in its original operation mode is less suitable. On the one hand, it is known that the diameter of defects suitable for vortex pinning must not be smaller than the superconducting coherence length, which is $\xi_{ab}(0) \simeq 1.2$ nm in YBCO.³³ On the other hand, the inherent deflection of the ion trajectories by scattering at the target atoms when traversing the material will cause a blurring of the focus with increasing depth. In this situation the fluence of the He^+ ions decreases strongly from the surface to the back of the YBCO film. To achieve a high enough ion fluence for suppression of T_c throughout the entire film thickness, the intensity of the focused ion beam must then be set to such a high value that amorphization of the YBCO crystal lattice^{7,32} and mechanical destruction near the sample's surface result. This is illustrated in Figure 1b which was recorded in the HIM after irradiation of a test pattern with an optimally focused He^+ ion beam with a much larger number of ions/spot than normally used in our experiments. Around the impact point of the focused ion beam the YBCO structure is

completely destroyed and blisters with about 50 nm diameter bulge out of the surface, while under the regular conditions for fabrication of pinning lattices, the irradiated areas are invisible in both the HIM and with scanning electron microscopy.

To avoid these shortcomings and irradiate a well-defined area, our approach uses an intentionally defocused ion beam. This is achieved by first adjusting the HIM settings to highest resolution and afterward changing the working distance (beam focus plane) by $8 \mu\text{m}$. The aperture angle of the ion beam is $\pm 0.07^\circ$; hence, the ion beam hits the sample surface almost orthogonally with a nearly Gaussian fluence profile²⁸ with a full width at half-maximum (fwhm) of about 20 nm.

The resulting three-dimensional shape of CDs with suppressed T_c is inferred from simulations of ion–matter interaction and collision cascades with the program SRIM³⁴ and calibrated to experimental data of T_c suppression as a function of defect density. Details of such calculations are reported elsewhere.³⁵ A defocused 30 keV He^+ beam of 20 nm fwhm diameter creates well-defined cylindrical channels with diameters ~ 25 nm in a YBCO film within which T_c is suppressed or reduced up to a depth of 80 nm, as evidenced in Figure 1c. In thicker YBCO films, however, the collision cascades are prone to substantial straggling which leads to blurring of the profile and insufficient reduction of T_c due to a lower defect density as it has been observed in heavy-ion-irradiated YBCO single crystals.³⁶

2.2. Vortex Commensurability Effects in Quasi-Kagomé Vortex Pinning Arrays. As a proof-of-concept experiment we have fabricated a square array of columnar defect cylinders with a defocused ion beam of fwhm = 50 nm and with a lattice spacing (nearest-neighbor distance) $a = 200$ nm in a 80 nm thick YBCO film and measured the critical current $I_c(B_d)$ in the superconducting state and the magnetoresistance $R(B_d)$ in the voltage state as a function of the applied magnetic field B_d . The parameters were chosen similarly to previous experiments performed with masked ion beam irradiation.^{10–13} Consistently, a clear peak of $I_c(B_d)$ corresponding to a minimum of $R(B_d)$ is found when each CD is filled by one vortex, and a tiny feature can be noticed for filling of each CD by two vortices (see the Supporting Information).

Pinning lattices can be designed not only with common hexagonal³⁷ or square tilings¹⁸ but also as more complex periodic or even quasi-periodic tilings that exhibit a number of unusual phenomena. Some examples of such arrays have been studied theoretically^{38–41} and experimentally in metallic superconductors with holes^{42–44} and magnetic dots,^{45–48} like Penrose,^{42,43} honeycomb,^{16,49} and kagomé⁵⁰ lattices and artificial vortex ice arrangements in geometrically frustrated pinning lattices.^{51–53} In HTSCs, such studies have been scarce⁵⁴ due to the much more demanding nanopatterning.

The particular advantage of irradiation in the HIM over other nanopatterning techniques is the higher spatial resolution and the ability to easily produce any desired pattern. We demonstrate this by the fabrication of quasi-kagomé pinning lattices with ultrasmall lattice spacing $a = 90$ nm (sample QK90) and 70 nm (sample QK70). The quasi-kagomé lattice is formed from a hexagonal lattice, where three neighboring sites are not occupied,⁴⁸ as sketched in Figure 1d. The quasi-kagomé lattice consists of vertex triangles with six sites per unit cell and large voids. It provides a unique platform to investigate the competition between pinning potentials and elastic energy of the vortex lattice. The quasi-kagomé lattice is a more extreme variant of the genuine kagomé tiling, which is formed

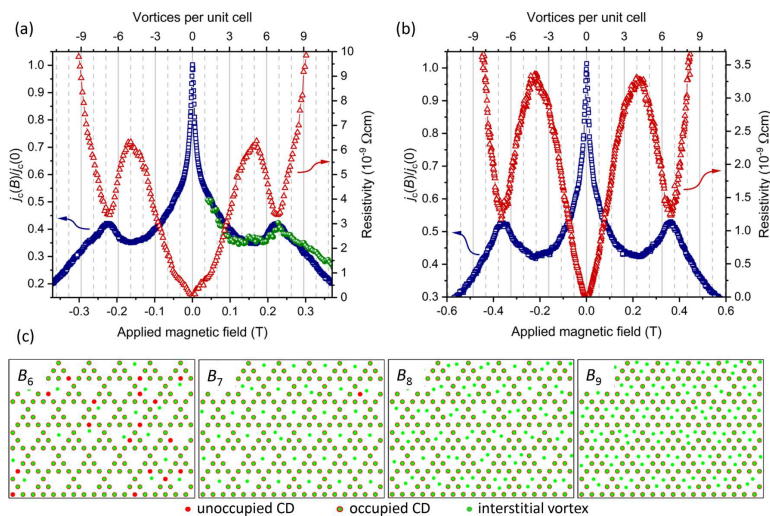


Figure 2. (a) Magnetic field dependence of the normalized critical current at 83 K (blue squares) and resistivity at 83.5 K (red triangles) of a 75 nm thick YBCO film, irradiated with a quasi-kagomé pattern of beam spots (20 nm fwhm) in a HIM (sample QK90). The upper horizontal scale indicates the matching fields B_k calculated from eq 1, for a filling of the unit cell with k vortices. The peak in the critical current and the minimum in the resistivity correspond to $k = 7$. The green bullets represent the results from molecular dynamics simulations. Only the positive branch of the mirror symmetric results is shown for clarity. (b) Normalized critical current at 52 K (blue squares) and resistivity at 55 K (red triangles) for sample QK70. (c) Simulation of vortex arrangements in the quasi-kagomé lattice of sample QK90 for several applied magnetic fields that correspond to various commensurability conditions as labeled in the graphs. Red circles represent artificial pinning centers and green dots the vortices.

from the hexagonal lattice by eliminating every other site from every other row.

In periodic pinning lattices commensurability effects are expected to occur at applied magnetic fields that fulfill the matching condition

$$B_k = \frac{k\Phi_0}{A} \quad (1)$$

where k is the number of pinning sites (or vortices) in the unit cell of area A and $\Phi_0 = h/(2e)$ is the magnetic flux quantum.

The electrical transport properties of the YBCO films patterned with the quasi-kagomé pinning lattice show intriguing features. Those can be attributed to the fact that HIM nanopatterning enables the realization of ultradense pinning arrays. Accordingly, pronounced vortex commensurability effects in the critical current density $j_c(B_k)$ and the magnetoresistivity $\rho(B_k)$ appear at very high matching fields, at $B_6 = 0.23$ T for sample QK90 and at $B_6 = 0.38$ T for sample QK70, as shown in Figures 2a and 2b, respectively. The observed effects are well reproducible after storing the samples at room temperature for several weeks.

In the case of strong interactions between vortices and the pinning potential of the CDs, significant vortex commensurability effects are expected at B_6 , when each CD is filled with one vortex. Conversely, with strong vortex–vortex interactions and marginal influence of the pinning landscape, the elastic energy of the vortex ensemble should favor a hexagonal lattice, and the voids are expected to be filled with three interstitial

vortices, leading to commensurability signatures at B_9 . The former, for instance, was observed in a quasi-kagomé lattice of magnetic Ni dots embedded in a Nb superconducting film.⁴⁸

Surprisingly, none of these features are found here; instead, a prominent matching peak in $j_c(B_k)$ and a corresponding minimum in $\rho(B_k)$ appear at B_7 , as can be seen in Figure 2a,b. Presumably, all CDs are occupied by vortices, and one interstitial vortex per unit cell is “caged” inside the voids of the lattice due to repulsion forces from the trapped vortices. On the other hand, the absence of a matching feature at B_1 indicates that the six closely packed sites of the kagomé triangle do not merge into a single pinning site. This confirms that despite the rather narrow distance of CDs they act as separate pinning potentials.

Molecular dynamics simulations shed more light on the vortex distribution in the quasi-kagomé lattice. A rectangular cell with periodic boundary conditions is used for the calculations. The vortex–vortex interaction, the pinning force on the vortices at the CDs, an external driving force, and a thermal stochastic force are taken into account, as detailed elsewhere for previous simulations.^{39,40,55,56} The ground state of the static vortex arrangement (zero driving force) is obtained by starting the simulation at some elevated “temperature” and gradually decreasing it to zero, thus performing a simulated thermal annealing. Note that this corresponds to magnetic-field-cooled experiments. However, since in our measurements no hysteresis was observed between

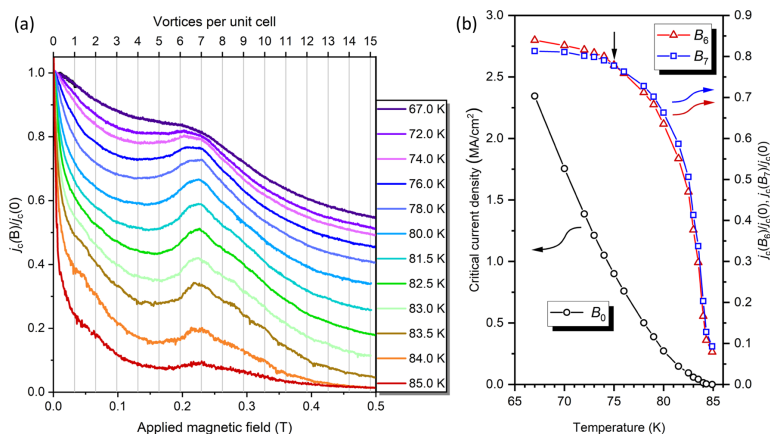


Figure 3. (a) Normalized critical current density of sample QK90 as a function of the applied magnetic field at various temperatures. The branches at reversed polarity of the magnetic field are mirror symmetric and are not shown. The upper horizontal scale displays the commensurability fields for k vortices in the unit cell of the quasi-kagomé pattern. (b) Temperature variation of the critical current density at B_0 (black circles) and the normalized critical current densities at B_6 (red triangles) and B_7 (blue squares). At lower temperatures, starting from the crossover at 75 K marked by the arrow, the critical current at the B_6 commensurability field exceeds the critical current at B_7 .

up- and down-ramping of the magnetic field, these results are equally valid for magnetic-field-ramped experiments.

In the simulations, the critical current density j_c is determined to be the minimum current density that depins the vortices; in the experiments the common electric field criterion of $10 \mu\text{V}/\text{cm}$ is used. The simulated values for the critical current density are then scaled to the experimental results (for sample QK90) at $B_0 = 50 \text{ mT}$.

The results of the simulations of static vortex configurations at different magnetic fields B_k and for temperatures adapted to the experimental situation are displayed in Figure 2c. For B_6 , where the average density of vortices matches the density of CDs, most of the pinning centers are filled with vortices, but several empty pins and, in turn, interstitial vortices can be noticed. This is explained by the strong repulsion between the vortices located on the closely packed pinning sites such that some of these vortices can depin and move in the voids, thus minimizing the energy. For B_7 almost all pins are filled, and typically one excess vortex sits in the centers of the voids of the quasi-kagomé lattice. If the magnetic field is further increased, all pins are occupied, and the voids host two (B_8) or three (B_9) vortices with minor fluctuations ± 1 in this number. In the latter case, the hexagonal vortex lattice is mostly recovered. Note that an experimental visualization of the vortex arrangements in ultradense pinning lattices is challenging. Because $\lambda_{L, \text{orb}}(T) \gg a$ in our samples, the magnetic fields of the vortices overlap strongly and magnetic force microscopy might not provide enough contrast.

A simulation of the critical current density $j_c(B_0)$ is displayed in Figure 2a. Indeed, there is no peak in $j_c(B_0)$ visible at B_6 , and peaks of $j_c(B_0)$ at B_8 and B_9 are hardly noticeable, whereas a pronounced peak at B_7 is found, in excellent agreement with the experimental results. This unconventional commensurability effect can be explained by the competition of the elastic vortex lattice energy, which favors a hexagonal lattice and the

semiregular quasi-kagomé pinning potential. At B_6 filling of all CDs with vortices would lead to a maximized pinning force density, but the repulsion between the trapped vortices leads to a significant number of vacancies at the pinning sites and, in turn, mobile interstitial vortices in the kagomé voids that reduce j_c . On the other hand, for B_9 , the elastic energy of the vortex lattice is minimized, but pinning is not so efficient due to the larger number of interstitial vortices. Thus, a commensurate arrangement in which all pinning sites are occupied and one interstitial vortex is caged in the center of the voids appears to be the most stable structure at temperatures near T_c .

The balance between the pinning forces at the CDs and the vortex caging potential can be tuned with temperature. While both increase at lower temperature, the pinning forces at the artificial defect lattice increase more rapidly.⁵⁷ To study this behavior on our samples, we performed electric transport measurements at variable T . Figure 3a shows normalized j_c vs B_k curves for sample QK90 at $67 \text{ K} \leq T \leq 85 \text{ K}$. We find that at temperatures $T < 80 \text{ K}$ a second peak of j_c around B_6 emerges, coalescing with the peak at B_7 into a broader feature with $j_c(B_6) > j_c(B_7)$ at even lower temperatures. This is a formidable demonstration of how the vortices “crystallize” into the quasi-kagomé lattice at lower temperatures when the artificial pinning landscape becomes dominant. Figure 3b displays the critical current density j_c at $B = 0$, calculated from the sample’s cross section. However, it has to be cautioned that the irradiated sample contains many CDs, and hence a significant volume in the sample does not contribute to the supercurrent, making a comparison to pristine YBCO films inappropriate. The normalized $j_c(B_6)/j_c(0)$ and $j_c(B_7)/j_c(0)$ curves reveal the crossover at $T = 75 \text{ K}$, where pinning at a matching field of six vortices/unit cell becomes more efficient.

Our findings may be compared to somewhat related simulation results. For a honeycomb pinning lattice it has

been demonstrated⁴¹ that j_c of a commensurate vortex arrangement with an additional caged vortex can be larger than that with the pinning sites occupied only. However, this only applies to shallow pinning potentials, whereas the situation is reversed for strong pinning, in excellent accordance with our observation of the crossover to $j_c(B_0) > j_c(B_T)$ at lower temperatures. Note, however, that one caged vortex in a honeycomb lattice restores the ideal hexagonal vortex lattice, while in our quasi-kagomé lattice one interstitial vortex is still associated with elastic energy of the vortex lattice. Thus, additional simulations with varying pinning potentials in the quasi-kagomé lattice are envisaged.

3. CONCLUSIONS

In summary, we have demonstrated the fabrication of periodic arrays of pinning centers in thin YBCO films with ultranarrow lattice spacings down to 70 nm by irradiation with the defocused beam of a HIM. This technique opens the route to create large arrays of pinning sites with user-defined positions and with a resolution superior to the lithographic techniques. As an example of a complex pinning landscape, the quasi-kagomé pinning lattice exhibits an unconventional commensurability effect, when all pins are occupied by vortices and one interstitial vortex is magnetically caged in each void of the lattice. It has been suggested that such caged vortices can be more easily manipulated along predetermined paths,⁵⁸ and hence, our findings can pave the way toward “Fluxonic” applications^{59–61} of cuprate superconductors.

4. MATERIALS AND METHODS

Superconducting Film Growth. Thin films of $\text{YBa}_2\text{Cu}_3\text{O}_{7-\delta}$ were grown epitaxially on (100) MgO single-crystal substrates by pulsed-laser deposition using 248 nm KrF excimer laser radiation at a fluence of 3.2 J/cm^2 . The thicknesses of the films are $t_s = 75 \pm 5 \text{ nm}$ (sample QK90) and $t_s = 50 \pm 5 \text{ nm}$ (sample QK70) as determined by atomic force microscopy. Bridges with dimensions $240 \times 60 \mu\text{m}^2$ are lithographically patterned for the electrical transport measurements. Two longitudinal voltage probes with a distance of $100 \mu\text{m}$ are applied on side arms of the bridges. The as-prepared samples had critical temperatures $T_c \sim 90 \text{ K}$ and transition widths $\Delta T_c \sim 1 \text{ K}$.

Ion Beam Irradiation. The prepatterned YBCO microbridges are introduced into the Zeiss Orion NanoFab He ion microscope and with low ion fluence the proper alignment of the sample surface to the focus plane of the ion optics is checked. Controlled defocus is achieved by changing the working distance by $8 \mu\text{m}$ from the focus plane, resulting in irradiation spots of about 20 nm diameter. Every point of the lattice, defined by a deflection list loaded into the Nano Patterning and Visualization Engine (NPVE), is irradiated with 30 keV He^+ ions with a dwell time of 1.2 ms (0.83 ms) and a beam current of 2.0 pA (2.9 pA) for sample QK90 (QK70), corresponding to 15000 He^+ ions/point. The average fluence hitting the sample's surface in the focus spot of about 20 nm fwhm is $4.8 \times 10^{15} \text{ cm}^{-2}$. The irradiated area is approximately $200 \mu\text{m} \times 100 \mu\text{m}$.

Electrical Transport Measurements. The electrical measurements are performed in a closed-cycle cryocooler mounted between the pole pieces of an electromagnet. A Cernox resistor⁶² together with a LakeShore 336 temperature controller is used for in-field temperature control to a stability of about 1 mK. The magnetic field, oriented perpendicular to the sample surface, is tuned by a programmable constant current source and measured with a LakeShore 475 gaussmeter with a resolution of 0.1 μT , a zero offset $<10 \mu\text{T}$, and a reading accuracy $<0.1\%$. The resistivity measurements are performed with a current of 0.8 mA, generated by a Keithley 6221 constant-current source in both polarities to exclude thermoelectric signals, and the voltage is measured with a Keithley 2182A nanovoltmeter. The critical current is determined from isothermal

current–voltage (I – V) measurements with a voltage criterion of 100 nV, corresponding to $10 \mu\text{V/cm}$. The I – V curves do not exhibit features that could be used to discriminate between the depinning of the vortices trapped in the CDs and the interstitial vortices, respectively.

Numerical Simulations. The simulations are performed in a 2D (in the xy -plane) simulation cell with periodic boundary conditions that models an infinite superconducting film characterized by the penetration depth λ , which is set to $\lambda_{L,ab}(T)$ at finite T . The cell is chosen large enough to avoid finite-size effects. Simulated annealing calculations are performed by numerically integrating the overdamped equations of motion:^{39,40,55} $\eta \mathbf{v}_i = \mathbf{f}_i = \mathbf{f}_i^{\text{vv}} + \mathbf{f}_i^{\text{fp}} + \mathbf{f}_i^{\text{p}} + \mathbf{f}_i^{\text{t}}$. Here \mathbf{f}_i is the total force per unit length acting on vortex i , \mathbf{f}_i^{vv} and \mathbf{f}_i^{fp} are the forces due to vortex–vortex and vortex–pin interactions, respectively, \mathbf{f}_i^{t} is the thermal stochastic force, and \mathbf{f}_i^{p} is the driving force; η is the viscosity, which is set to unity. The force due to the vortex–vortex interaction is $\mathbf{f}_i^{\text{vv}} = \sum_{j \neq i}^N f_{ij} K_1(|\mathbf{r}_i - \mathbf{r}_j|/\lambda) \hat{\mathbf{e}}_{ij}$ where N_i is the number of vortices, K_1 is a modified Bessel function, $\hat{\mathbf{e}}_{ij} = (\mathbf{r}_i - \mathbf{r}_j)/|\mathbf{r}_i - \mathbf{r}_j|$, and $f_{ij} = \Phi_0^2 / 8 \pi^2 \lambda^3$. The pinning force is $\mathbf{f}_i^{\text{fp}} = \sum_{j \neq i}^N f_{ij} \cdot (|\mathbf{r}_i - \mathbf{r}_j^{\text{fp}}|/r_p) \Theta(|r_p - |\mathbf{r}_i - \mathbf{r}_j^{\text{fp}}||) / \lambda \hat{\mathbf{r}}_{ik}^{\text{fp}}$ where N_p is the number of pinning sites, f_p (expressed in f_0) is the maximum pinning force of each short-range parabolic potential well located at \mathbf{r}_k^{fp} , r_p is the range of the pinning potential, Θ is the Heaviside step function, and $\hat{\mathbf{r}}_{ik}^{\text{fp}} = (\mathbf{r}_i - \mathbf{r}_k^{\text{fp}})/|\mathbf{r}_i - \mathbf{r}_k^{\text{fp}}|$. All the lengths (fields) are expressed in units of λ (Φ_0/λ^2). The ground state of a system of moving vortices is obtained by simulating field-cooled experiments. In this approximation of deep short-range (δ -like) potential wells, the critical current can be defined as follows^{39,40,45,44,55} (giving essentially the same results as those obtained using the threshold criterion in dynamical simulations^{39,40}): $j_c(\Phi) = j_0 N_{\text{fp}}^{(p)}(\Phi) / N_c(\Phi)$, where j_0 is a constant, and study the dimensionless value $J_c = j_c / j_0$.

■ ASSOCIATED CONTENT

Supporting Information

The Supporting Information is available free of charge on the ACS Publications website at DOI: 10.1021/acsnano.9b01006.

Critical current and resistance data of a square array of vortex pinning centers fabricated by irradiation in the helium ion microscope (PDF)

■ AUTHOR INFORMATION

Corresponding Author

*E-mail: wolfgang.lang@univie.ac.at

ORCID

Vyacheslav R. Misko: 0000-0002-5290-412X

Meirzhan Dosmaliev: 0000-0003-3672-0619

Johannes D. Pedarnig: 0000-0002-7842-3922

Wolfgang Lang: 0000-0001-8722-2674

Present Address

M.D.: Al-Farabi Kazakh National University, Almaty, Kazakhstan.

Notes

The authors declare no competing financial interest.

■ ACKNOWLEDGMENTS

The authors thank John Notte and Jason Huang for enlightening discussions on helium ion microscopy and for initial test irradiations in the HIM at Carl Zeiss Ion Microscopy Innovation Center in Peabody, USA, and Georg Zechner for experimental support. B.M. acknowledges funding by the German Academic Scholarship Foundation. V.R.M. and F.N. acknowledge support by the Research Foundation-

Flanders (FWO-VI) and Japan Society for the Promotion of Science (JSPS) (JSPS-FWO Grant VS.059.18N). F.N. is supported in part by the MURI Center for Dynamic Magneto-Optics via the Air Force Office of Scientific Research (AFOSR) (FA9550-14-1-0040), Army Research Office (ARO) (Grant 7331SPH), Asian Office of Aerospace Research and Development (AOARD) (Grant FA2386-18-1-4045), Japan Science and Technology Agency (JST) (the Q-LEAP program and CREST Grant JPMJCR1676), Japan Society for the Promotion of Science (JSPS) (JSPS-RFBR Grant 17-52-50023), RIKEN-AIST Challenge Research Fund. Research was conducted within the framework of the COST Action CA16218 (NANOCOHBRY) of the European Cooperation in Science and Technology.

REFERENCES

- (1) Kleiner, R.; Buckel, W. *Superconductivity*, 3rd ed.; Wiley-VCH: Weinheim, 2016.
- (2) Civale, L. Vortex pinning and creep in high-temperature superconductors with columnar defects. *Supercond. Sci. Technol.* **1997**, *10*, A11–A28.
- (3) Haugan, T.; Barnes, P. N.; Wheeler, R.; Meisenkothen, F.; Sumption, M. Addition of nanoparticle dispersions to enhance flux pinning of the $\text{YBa}_2\text{Cu}_3\text{O}_{7-x}$ superconductor. *Nature* **2004**, *430*, 867.
- (4) Sefrioui, Z.; Arias, D.; González, E. M.; León, C.; Santamaria, J.; Vicent, J. L. Vortex liquid entanglement in irradiated $\text{YBa}_2\text{Cu}_3\text{O}_{7-\delta}$ thin films. *Phys. Rev. B: Condens. Matter Mater. Phys.* **2001**, *63*, 064503.
- (5) Lang, W.; Enzenhofer, T.; Peruzzi, M.; Pedarnig, J. D.; Bäuerle, D.; Horner, C.; Cekan, E.; Platzgummer, E.; Loeschner, H. Tailoring the transport properties of $\text{YBa}_2\text{Cu}_3\text{O}_{7-x}$ thin films by light-ion irradiation. *Inst. Phys. Conf. Ser.* **2004**, *181*, 1549–1555.
- (6) Cybart, S. A.; Yen, P. X. T.; Cho, E. Y.; Huh, J. U.; Glyantsev, V. N.; Yung, C. S.; Moeckly, B.; Beeman, J. W.; Dynes, R. C. Comparison of Y–Ba–Cu–O Films Irradiated With Helium and Neon Ions for the Fabrication of Josephson Devices. *IEEE Trans. Appl. Supercond.* **2014**, *24*, 1–5.
- (7) Lang, W.; Dineva, M.; Marksteiner, M.; Enzenhofer, T.; Siraj, K.; Peruzzi, M.; Pedarnig, J. D.; Bäuerle, D.; Korntner, R.; Cekan, E.; Platzgummer, E.; Loeschner, H. Ion-beam direct-structuring of high-temperature superconductors. *Microelectron. Eng.* **2006**, *83*, 1495–1498.
- (8) Lang, W.; Richter, H.; Marksteiner, M.; Siraj, K.; Bodea, M. A.; Pedarnig, J. D.; Grigoropoulos, C.; Bäuerle, D.; Hasenfuss, C.; Palmethofer, L.; Kolarova, R.; Bauer, P. Masked ion beam irradiation of high-temperature superconductors: patterning of nano-size regions with high point-defect density. *Int. J. Nanotechnol.* **2009**, *6*, 104–14.
- (9) Pedarnig, J. D.; Siraj, K.; Bodea, M. A.; Puica, I.; Lang, W.; Kolarova, R.; Bauer, P.; Haselgrübler, K.; Hasenfuss, C.; Beinik, I.; Teichert, C. Surface planarization and masked ion-beam structuring of $\text{YBa}_2\text{Cu}_3\text{O}_7$ thin films. *Thin Solid Films* **2010**, *518*, 7075–80.
- (10) Swieciński, I.; Ulysse, C.; Wolf, T.; Bernard, R.; Bergeal, N.; Briatico, J.; Faini, G.; Lesueur, J.; Villegas, J. E. Strong field-matching effects in superconducting $\text{YBa}_2\text{Cu}_3\text{O}_{7-\delta}$ films with vortex energy landscapes engineered via masked ion irradiation. *Phys. Rev. B: Condens. Matter Mater. Phys.* **2012**, *85*, 224502.
- (11) Trastoy, J.; Rouco, V.; Ulysse, C.; Bernard, R.; Palau, A.; Puig, T.; Faini, G.; Lesueur, J.; Briatico, J.; Villegas, J. E. Unusual magneto-transport of $\text{YBa}_2\text{Cu}_3\text{O}_{7-\delta}$ films due to the interplay of anisotropy, random disorder and nanoscale periodic pinning. *New J. Phys.* **2013**, *15*, 103022.
- (12) Haag, L. T.; Zechner, G.; Lang, W.; Domsailov, M.; Bodea, M. A.; Pedarnig, J. D. Strong vortex matching effects in YBCO films with periodic modulations of the superconducting order parameter fabricated by masked ion irradiation. *Physica C* **2014**, *503*, 75–81.
- (13) Zechner, G.; Jausner, F.; Haag, L. T.; Lang, W.; Domsailov, M.; Bodea, M. A.; Pedarnig, J. D. Hysteretic Vortex-Matching Effects in High- T_c Superconductors with Nanoscale Periodic Pinning Landscapes Fabricated by He Ion-Beam Projection. *Phys. Rev. Appl.* **2017**, *8*, 014021.
- (14) Yang, C. et al. Quantum coherence across bosonic superconductor-anomalous metal-insulator transitions. arXiv:1901.07706 [cond-mat.supr-con], 2019.
- (15) Moshchalkov, V. V.; Fritzsche, J. *Nanostructured Superconductors*; World Scientific: Singapore, 2011.
- (16) Welp, U.; Xiao, Z. L.; Jiang, J. S.; Vlasko-Vlasov, V. K.; Bader, S. D.; Crabtree, G. W.; Liang, J.; Chik, H.; Xu, J. M. Superconducting transition and vortex pinning in Nb films patterned with nanoscale hole arrays. *Phys. Rev. B: Condens. Matter Mater. Phys.* **2002**, *66*, 212507.
- (17) Hallet, X.; Mátéfi-Tempfli, M.; Michotte, S.; Piraux, L.; Vanacken, J.; Moshchalkov, V. V.; Mátéfi-Tempfli, S. Quasi-Hexagonal Vortex-Pinning Lattice Using Anodized Aluminum Oxide Nanotemplates. *Small* **2009**, *5*, 2413–2416.
- (18) Wölbling, R.; Schwarz, T.; Müller, B.; Nagel, J.; Kemmler, M.; Kleiner, R.; Koelle, D. Optimizing the spin sensitivity of grain boundary junction nanoSQUIDS – towards detection of small spin systems with single-spin resolution. *Supercond. Sci. Technol.* **2014**, *27*, 125007.
- (19) Thiel, L.; Rohner, D.; Ganzhorn, M.; Appel, P.; Neu, E.; Müller, B.; Kleiner, R.; Koelle, D.; Maletinsky, P. Quantitative nanoscale vortex imaging using a cryogenic quantum magnetometer. *Nat. Nanotechnol.* **2016**, *11*, 677–681.
- (20) Martínez-Pérez, M. J.; Müller, B.; Schwebius, D.; Korinski, D.; Kleiner, R.; Sesé, J.; Koelle, D. NanoSQUID magnetometry of individual cobalt nanoparticles grown by focused electron beam induced deposition. *Supercond. Sci. Technol.* **2017**, *30*, 024003.
- (21) Rohner, D.; Thiel, L.; Müller, B.; Kasperczyk, M.; Kleiner, R.; Koelle, D.; Maletinsky, P. Real-space probing of the local magnetic response of thin-film superconductors using single spin magnetometry. *Sensors* **2018**, *18*, 3790.
- (22) Dam, B.; Huijbregtse, J. M.; Klaassen, F. C.; van-der Geest, R. C. F.; Doornbos, G.; Rector, J. H.; Testa, A. M.; Freisem, S.; Martínez, J. C.; Stäubli-Pümpin, B.; Griessen, R. Origin of high critical currents in $\text{YBa}_2\text{Cu}_3\text{O}_{7-x}$ superconducting thin films. *Nature* **1999**, *399*, 439–442.
- (23) Castellanos, A.; Wördenweber, R.; Ockenfuss, G.; Hart, A. v. d.; Keck, K. Preparation of regular arrays of antidots in $\text{YBa}_2\text{Cu}_3\text{O}_7$ thin films and observation of vortex lattice matching effects. *Appl. Phys. Lett.* **1997**, *71*, 962–964.
- (24) <https://www.zeiss.com/microscopy/int/products/multiple-ion-beam/orion-nanofab-for-materials.html.2019-05-17>.
- (25) Ward, B. W.; Notte, T. A.; Economou, N. P. Helium ion microscope: A new tool for nanoscale microscopy and metrology. *J. Vac. Sci. Technol. B* **2006**, *24*, 2871–2874.
- (26) Hlawacek, G.; Götzhäuser, A., Eds.; *Helium Ion Microscopy*; Springer International Publishing: Switzerland, 2016.
- (27) Flatbø, R.; Agarwal, A.; Hobbs, R.; Greve, M. M.; Holst, B.; Berggren, K. K. Exploring proximity effects and large depth of field in helium ion beam lithography: large-area dense patterns and tilted surface exposure. *Nanotechnology* **2018**, *29*, 275301.
- (28) Emmrich, D.; Beyer, A.; Nadezdyka, A.; Bauerdick, S.; Meyer, J. C.; Kotakoski, J.; Götzhäuser, A. Nanopore fabrication and characterization by helium ion microscopy. *Appl. Phys. Lett.* **2016**, *108*, 163103.
- (29) Cybart, S. A.; Cho, E. Y.; Wong, T. J.; Wehlin, B. H.; Ma, M. K.; Huynh, C.; Dynes, R. C. Nano Josephson superconducting tunnel junctions in $\text{YBa}_2\text{Cu}_3\text{O}_{7-x}$ directly patterned with a focused helium ion beam. *Nat. Nanotechnol.* **2015**, *10*, 598.
- (30) Cho, E. Y.; Ma, M. K.; Huynh, C.; Pratt, K.; Paulson, D. N.; Glyantsev, V. N.; Dynes, R. C.; Cybart, S. A. $\text{YBa}_2\text{Cu}_3\text{O}_{7-\delta}$ superconducting quantum interference devices with metallic to insulating barriers written with a focused helium ion beam. *Appl. Phys. Lett.* **2015**, *106*, 252601.
- (31) Cho, E. Y.; Zhou, Y. W.; Cho, J. Y.; Cybart, S. A. Superconducting nano Josephson junctions patterned with a focused helium ion beam. *Appl. Phys. Lett.* **2018**, *113*, 022604.

- (32) Müller, B.; Karrer, M.; Limberger, F.; Becker, M.; Schröppel, B.; Burkhardt, C. J.; Kleiner, R.; Goldobin, E.; Koelle, D. Josephson Junctions and SQUIDs Created by Focused Helium-Ion-Beam Irradiation of $\text{YBa}_2\text{Cu}_3\text{O}_7$. *Phys. Rev. Appl.* **2019**, *11*, 044082.
- (33) Sekirnjak, C.; Lang, W.; Proyer, S.; Schwab, P. Novel approach for the analysis of the fluctuation magnetoconductivity in $\text{YBa}_2\text{Cu}_3\text{O}_7$ thin films. *Physica C* **1995**, *243*, 60–68.
- (34) Ziegler, J. F.; Ziegler, M. D.; Biersack, J. P. SRIM – The stopping and range of ions in matter (2010). *Nucl. Instrum. Methods Phys. Res., Sect. B* **2010**, *268*, 1818–23.
- (35) Mletschnig, K. L.; Lang, W. Nano-patterning of cuprate superconductors by masked He^+ ion irradiation: 3-dimensional profiles of the local critical temperature. *Microelectron. Eng.* **2019**, *215*, 110982.
- (36) Niebieskikwiat, D.; Silhanek, A.; Civalo, L.; Nieva, G.; Levy, P.; Krusin-Elbaum, L. Suppression of matching field effects by splay and pinning energy dispersion in $\text{YBa}_2\text{Cu}_3\text{O}_7$ with columnar defects. *Phys. Rev. B: Condens. Matter Mater. Phys.* **2001**, *63*, 144504.
- (37) Ooi, S.; Mochiku, T.; Yu, S.; Sasaki, E. S.; Hirata, K. Matching effect of vortex lattice in $\text{Bi}_2\text{Sr}_2\text{CaCu}_2\text{O}_{8+y}$ with artificial periodic defects. *Physica C* **2005**, *426*, 113–117.
- (38) Laguna, M. F.; Balseiro, C. A.; Domínguez, D.; Nori, F. Vortex structure and dynamics in kagomé and triangular pinning potentials. *Phys. Rev. B: Condens. Matter Mater. Phys.* **2001**, *64*, 104505.
- (39) Misko, V.; Savel'ev, S.; Nori, F. Critical Currents in Quasiperiodic Pinning Arrays: Chains and Penrose Lattices. *Phys. Rev. Lett.* **2005**, *95*, 177007.
- (40) Misko, V. R.; Savel'ev, S.; Nori, F. Critical currents in superconductors with quasiperiodic pinning arrays: One-dimensional chains and two-dimensional Penrose lattices. *Phys. Rev. B: Condens. Matter Mater. Phys.* **2006**, *74*, 024522.
- (41) Reichhardt, C.; Olson Reichhardt, C. J. Vortex molecular crystal and vortex plastic crystal states in honeycomb and kagomé pinning arrays. *Phys. Rev. B: Condens. Matter Mater. Phys.* **2007**, *76*, 064523.
- (42) Kemmler, M.; Gürlich, C.; Sterck, A.; Pöhler, H.; Neuhaus, M.; Siegel, M.; Kleiner, R.; Koelle, D. Commensurability effects in superconducting Nb films with quasiperiodic pinning arrays. *Phys. Rev. Lett.* **2006**, *97*, 147003.
- (43) Misko, V. R.; Bothner, D.; Kemmler, M.; Kleiner, R.; Koelle, D.; Peeters, F. M.; Nori, F. Enhancing the critical current in quasiperiodic pinning arrays below and above the matching magnetic flux. *Phys. Rev. B: Condens. Matter Mater. Phys.* **2010**, *82*, 184512.
- (44) Bothner, D.; Seidl, R.; Misko, V. R.; Kleiner, R.; Koelle, D.; Kemmler, M. Unusual commensurability effects in quasiperiodic pinning arrays induced by local inhomogeneities of the pinning site density. *Supercond. Sci. Technol.* **2014**, *27*, 065002.
- (45) Villegas, J. E.; Montero, M. L.; Li, C.-P.; Schuller, I. K. Correlation length of quasiperiodic vortex lattices. *Phys. Rev. Lett.* **2006**, *97*, 027002.
- (46) Silhanek, A. V.; Gillijns, W.; Moshchalkov, V. V.; Zhu, B. Y.; Moonens, J.; Leunissen, L. H. A. Enhanced pinning and proliferation of matching effects in a superconducting film with a Penrose array of magnetic dots. *Appl. Phys. Lett.* **2006**, *89*, 152507.
- (47) Kramer, R. B. G.; Silhanek, A. V.; Van de Vondel, J.; Raes, B.; Moshchalkov, V. V. Symmetry-Induced Giant Vortex State in a Superconducting Pb Film with a Fivefold Penrose Array of Magnetic Pinning Centers. *Phys. Rev. Lett.* **2009**, *103*, 067007.
- (48) Perez de Lara, D.; Alija, A.; Gonzalez, E. M.; Velez, M.; Martin, J. I.; Vicent, J. L. Vortex ratchet reversal at fractional matching fields in kagomélike array with symmetric pinning centers. *Phys. Rev. B: Condens. Matter Mater. Phys.* **2010**, *82*, 174503.
- (49) Latimer, M. L.; Berdiyrov, G. R.; Xiao, Z. L.; Kwok, W. K.; Peeters, F. M. Vortex interaction enhanced saturation number and caging effect in a superconducting film with a honeycomb array of nanoscale holes. *Phys. Rev. B: Condens. Matter Mater. Phys.* **2012**, *85*, 012505.
- (50) Cuppens, J.; Ataklti, G. W.; Gillijns, W.; Van de Vondel, J.; Moshchalkov, V. V.; Silhanek, A. V. Vortex Dynamics in a Superconducting Film with a Kagome and a Honeycomb Pinning Landscape. *J. Supercond. Novel Magn.* **2011**, *24*, 7–11.
- (51) Libal, A.; Olson Reichhardt, C. J.; Reichhardt, C. Creating artificial ice states using vortices in nanostructured superconductors. *Phys. Rev. Lett.* **2009**, *102*, 237004.
- (52) Latimer, M. L.; Berdiyrov, G. R.; Xiao, Z. L.; Peeters, F. M.; Kwok, W. K. Realization of Artificial Ice Systems for Magnetic Vortices in a Superconducting MoGe Thin Film with Patterned Nanostructures. *Phys. Rev. Lett.* **2013**, *111*, 067001.
- (53) Xue, C.; Ge, J.-Y.; He, A.; Zharinov, V. S.; Moshchalkov, V. V.; Zhou, Y. H.; Silhanek, A. V.; Van de Vondel, J. Tunable artificial vortex ice in nanostructured superconductors with a frustrated kagome lattice of paired antidots. *Phys. Rev. B: Condens. Matter Mater. Phys.* **2018**, *97*, 134506.
- (54) Trastoy, J.; Malnou, M.; Ulysse, C.; Bernard, R.; Bergeal, N.; Faini, G.; Lesueur, J.; Briatico, J.; Villegas, J. E. Freezing and thawing of artificial ice by thermal switching of geometric frustration in magnetic flux lattices. *Nat. Nanotechnol.* **2014**, *9*, 710–715.
- (55) Reichhardt, C.; Olson, C. J.; Nori, F. Commensurate and incommensurate vortex states in superconductors with periodic pinning arrays. *Phys. Rev. B: Condens. Matter Mater. Phys.* **1998**, *57*, 7937–7943.
- (56) Misko, V. R.; Nori, F. Magnetic flux pinning in superconductors with hyperbolic-tessellation arrays of pinning sites. *Phys. Rev. B: Condens. Matter Mater. Phys.* **2012**, *85*, 184506.
- (57) Khalifa, I. B.; Shapiro, B. Y. Relaxation of magnetic flux in a superconductor with a system of columnar defects. *Physica C* **1993**, *207*, 359–365.
- (58) Togawa, Y.; Harada, K.; Akashi, T.; Kasai, H.; Matsuda, T.; Nori, F.; Maeda, A.; Tonomura, A. Direct Observation of Rectified Motion of Vortices in a Niobium Superconductor. *Phys. Rev. Lett.* **2005**, *95*, 087002.
- (59) Wambaugh, J. F.; Reichhardt, C.; Olson, C. J.; Marchesoni, F.; Nori, F. Superconducting fluxon pumps and lenses. *Phys. Rev. Lett.* **1999**, *83*, 5106–5109.
- (60) Hastings, M. B.; Olson Reichhardt, C. J.; Reichhardt, C. Ratchet cellular automata. *Phys. Rev. Lett.* **2003**, *90*, 247004.
- (61) Milošević, M. V.; Berdiyrov, G. R.; Peeters, F. M. Fluxonic cellular automata. *Appl. Phys. Lett.* **2007**, *91*, 212501.
- (62) Heine, G.; Lang, W. Magnetoresistance of the new ceramic 'Cermox' thermometer from 4.2 to 300 K in magnetic fields up to 13 T. *Cryogenics* **1998**, *38*, 377–379.

Ultradense Tailored Vortex Pinning Arrays in Superconducting $\text{YBa}_2\text{Cu}_3\text{O}_{7-\delta}$ Thin Films Created by Focused He Ion-Beam Irradiation for Fluxonics Applications

Bernd Aichner,[†] Benedikt Müller,[‡] Max Karrer,[‡] Vyacheslav R. Misko,^{¶,§,||}
Fabienne Limberger,[‡] Kristijan L. Mletschnig,[†] Meirzhan Dosmailov,^{⊥, #} Johannes
D. Pedarnig,[⊥] Franco Nori,^{§, @} Reinhold Kleiner,[‡] Dieter Koelle,[‡] and Wolfgang
Lang^{*, †}

[†]*Faculty of Physics, University of Vienna, Wien, Austria*

[‡]*Physikalisches Institut and Center for Quantum Science (CQ) in LISA⁺, Universität
Tübingen, Tübingen, Germany*

[¶]*Department of Physics, Universiteit Antwerpen, Antwerpen, Belgium*

[§]*Theoretical Quantum Physics Laboratory, RIKEN Cluster for Pioneering Research,
Wako-shi, Saitama, Japan*

^{||}*μFlow group, Department of Chemical Engineering, Vrije Universiteit Brussel, Brussels,
Belgium*

[⊥]*Institute of Applied Physics, Johannes Kepler University Linz, Linz, Austria*

[#]*Current address: Al-Farabi Kazakh National University, Almaty, Kazakhstan*

[@]*Physics Department, University of Michigan, Ann Arbor, USA*

E-mail: wolfgang.lang@univie.ac.at

Supporting Information

Critical current and resistance data of a square array of vortex pinning centers fabricated by irradiation in the helium ion microscope

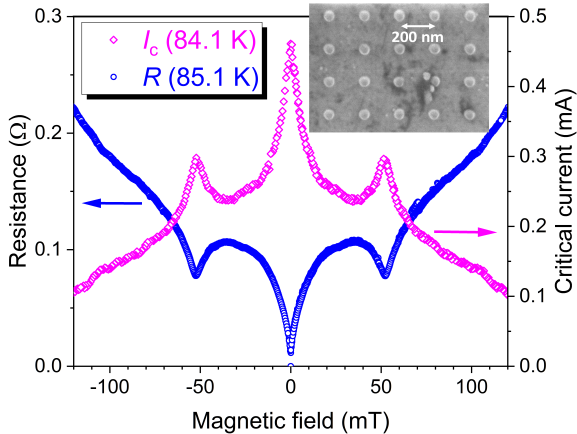


Figure S1: Critical current I_c and resistance R of a 80-nm thick YBCO film, irradiated in a HIM with a square pattern of beam spots (50 nm FWHM) with a lattice constant of 200 nm. The matching field determined from the geometric parameters is $B_m = 52$ mT and leads to a peak in the critical current and a minimum of the resistance. Inset: HIM image of a square array of defects induced by the focused ion beam of the HIM. Irradiation was performed with 5×10^6 ions/spot to visualize the pattern, a much larger fluence than it was used for preparation of the actual sample.

A square array of columnar defect cylinders (CDs) has been fabricated in the helium ion microscope with an intentionally defocused ion beam of FWHM = 50 nm and point-to-point distance $a = 200$ nm in a 80-nm thick YBCO film. The parameters were chosen similar to previous experiments performed with masked ion beam irradiation.¹⁻⁴ The critical current $I_c(B_a)$ shows a distinct peak and the magnetoresistance $R(B_a)$ a minimum when each defect is filled with one vortex at an applied magnetic field B_a that fulfils the matching condition for single-vortex occupation of every CD, $B_1 = \Phi_0/a^2$, where Φ_0 is the magnetic

flux quantum and $a = 200$ nm the lattice constant of the square pinning array. The vortex commensurability effects displayed in Fig. S1 appear exactly at the calculated matching field $B_1 = 52$ mT.

References

- (1) Swiecicki, I.; Ulysse, C.; Wolf, T.; Bernard, R.; Bergeal, N.; Briatico, J.; Faini, G.; Lesueur, J.; Villegas, J. E. Strong field-matching effects in superconducting $\text{YBa}_2\text{Cu}_3\text{O}_{7-\delta}$ films with vortex energy landscapes engineered via masked ion irradiation. *Phys. Rev. B* **2012**, *85*, 224502.
- (2) Trastoy, J.; Rouco, V.; Ulysse, C.; Bernard, R.; Palau, A.; Puig, T.; Faini, G.; Lesueur, J.; Briatico, J.; Villegas, J. E. Unusual magneto-transport of $\text{YBa}_2\text{Cu}_3\text{O}_{7-\delta}$ films due to the interplay of anisotropy, random disorder and nanoscale periodic pinning. *New J. Phys.* **2013**, *15*, 103022.
- (3) Haag, L. T.; Zechner, G.; Lang, W.; Dosmailov, M.; Bodea, M. A.; Pedarnig, J. D. Strong vortex matching effects in YBCO films with periodic modulations of the superconducting order parameter fabricated by masked ion irradiation. *Physica C* **2014**, *503*, 75–81.
- (4) Zechner, G.; Jausner, F.; Haag, L. T.; Lang, W.; Dosmailov, M.; Bodea, M. A.; Pedarnig, J. D. Hysteretic Vortex-Matching Effects in High- T_c Superconductors with Nanoscale Periodic Pinning Landscapes Fabricated by He Ion-Beam Projection. *Phys. Rev. Applied* **2017**, *8*, 014021.







Publication 4

Reprinted with permission from
B. Aichner et al., *Low Temperature Physics* **46**, 331 (2020)
Copyright © 2020 by the Authors.

Angular magnetic-field dependence of vortex matching in pinning lattices fabricated by focused or masked helium ion beam irradiation of superconducting $\text{YBa}_2\text{Cu}_3\text{O}_{7-\delta}$ thin films

Cite as: Low Temp. Phys. 46, 331 (2020); <https://doi.org/10.1063/10.0000863>

Submitted: 20 February 2020 . Published Online: 24 April 2020

B. Aichner , K. L. Mletschnig, B. Müller, M. Karrer, M. Dosmailov , J. D. Pedarnig , R. Kleiner , D. Koelle , and W. Lang 



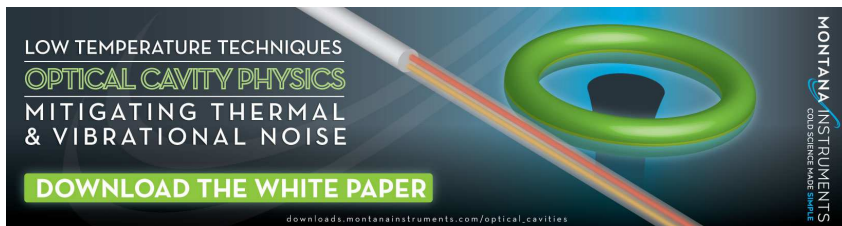
View Online



Export Citation



CrossMark



LOW TEMPERATURE TECHNIQUES
OPTICAL CAVITY PHYSICS
MITIGATING THERMAL
& VIBRATIONAL NOISE

DOWNLOAD THE WHITE PAPER

downloads.montanainstruments.com/optical_cavities

MONTANA INSTRUMENTS
COLD SCIENCE MADE SIMPLE



Angular magnetic-field dependence of vortex matching in pinning lattices fabricated by focused or masked helium ion beam irradiation of superconducting $\text{YBa}_2\text{Cu}_3\text{O}_{7-\delta}$ thin films

Cite as: Fiz. Nizk. Temp. 46, 402–409 (April 2020); doi: 10.1063/10.0000863

Submitted: 20 February 2020



B. Aichner,¹ K. L. Mletschnig,¹ B. Müller,² M. Karrer,² M. Dosmailov,^{3,4} J. D. Pedarnig,⁵ R. Kleiner,² D. Koelle,² and W. Lang^{1,a)}

AFFILIATIONS

¹University of Vienna, Faculty of Physics, Electronic Properties of Materials, Boltzmanngasse 5, A-1090 Wien, Austria

²Physikalisches Institut and Center for Quantum Science (CQ) in LISA+, Universität Tübingen, Auf der Morgenstelle 14, D-72076 Tübingen, Germany

³Johannes-Kepler-University Linz, Institute of Applied Physics, Altenbergerstrasse 69, A-4040 Linz, Austria

⁴Al-Farabi Kazakh National University, Almaty, Kazakhstan

^{a)}Author to whom correspondence should be addressed: wolfgang.lang@univie.ac.at

ABSTRACT

The angular dependence of magnetic-field commensurability effects in thin films of the cuprate high-critical-temperature superconductor $\text{YBa}_2\text{Cu}_3\text{O}_{7-\delta}$ (YBCO) with an artificial pinning landscape is investigated. Columns of point defects are fabricated by two different methods of ion irradiation — scanning the focused 30 keV ion beam in a helium ion microscope or employing the wide-field 75 keV He^+ beam of an ion implanter through a stencil mask. Simulations of the ion-target interactions and the resulting collision cascades reveal that with both methods square arrays of defect columns with sub- μm spacings can be created. They consist of dense point-defect clusters, which act as pinning centers for Abrikosov vortices. This is verified by the measurement of commensurable peaks of the critical current and related minima of the flux-flow resistance vs magnetic field at the matching fields. In oblique magnetic fields, the matching features are exclusively governed by the component of the magnetic field parallel to the axes of the columnar defects, which confirms that the magnetic flux is penetrated along the defect columns. We demonstrate that the latter dominate the pinning landscape despite of the strong intrinsic pinning in thin YBCO films.

Published under license by AIP Publishing. <https://doi.org/10.1063/10.0000863>

1. INTRODUCTION

Most of the superconducting materials belong to the type II class, into which a magnetic field can penetrate as flux quanta $\Phi_0 = h/(2e)$, where h is Planck's constant and e the elementary charge. These flux quanta are known as Abrikosov vortices, whirls of the supercurrent that confine the magnetic flux into the cylindrical vortex core, a region with vanishing density of superconducting charge carrier pairs. In clean and isotropic bulk superconductors these vortices arrange themselves in a two-dimensional hexagonal lattice with the axes of the vortex cores oriented parallel to the external magnetic field.

In the cuprate high-temperature superconductors (HTSCs) the situation is more complex and vortices can exist in a large range of magnetic fields between a tiny lower critical field $B_{c1}(85\text{ K}) \sim 2\text{ mT}$ and a high upper critical field $B_{c2}(85\text{ K}) \sim 20\text{ T}$ at temperatures relevant for the present study and for magnetic fields orthogonal to the CuO_2 atomic layers.¹ The high anisotropy of the HTSCs favors a decomposition of the cylindrical vortices into a stack of coupled “pancake” vortices,² which can be visualized, e.g., in $\text{Bi}_2\text{Sr}_2\text{CaCu}_2\text{O}_8$.³

The arrangement of vortices in type-II superconductors can be tailored by the introduction of artificial defects as pinning sites for vortices. Those defects can be classified by their dimensionality

and can severely disturb the native hexagonal vortex arrangement. Zero-dimensional (0D) point defects can be introduced as tiny non-superconducting impurities *in situ* during fabrication⁴ or by postprocessing with electron⁵ or light-ion irradiation of HTSCs.⁶ One-dimensional (1D) defects are commonly created by irradiation with swift heavy ions that produce amorphous channels with diameters of several nm, i.e., a few times the in-plane coherence length. They have been extensively investigated as a tool to enhance the critical current density.⁷ Finally, grain boundaries and, in the prototypical HTSC $\text{YBa}_2\text{Cu}_3\text{O}_{7-\delta}$ (YBCO) also twin planes, can form two-dimensional (2D) defects that can pin vortices.

The dimensionality of the artificial defects is revealed by different angle-dependent behavior in tilted magnetic fields of superconducting properties like the critical current I_c , the vortex-flow resistance R , and B_{c2} . While point defects lead to a marginal angular dependence, randomly distributed yet parallel oriented 1D columnar defects cause narrow features in I_c , R , and magnetization vs field direction, centered around the magnetic field direction parallel to their symmetry axes.^{8–10} Similar observations hold for 2D defect planes in YBCO when the magnetic field is rotated through a direction that is oriented parallel to these planes.¹¹

In this work, we investigate artificial pinning lattices that are different in two aspects. First, they are neither strictly 0D or 1D, since they consist of dense point defects that form columnar defect clusters (CDs) with diameters at least one order of magnitude larger than the in-plane coherence length $\xi_{ab}(0) = 1.2$ nm in YBCO.¹² Second, these CDs are arranged in a periodic pattern that gives rise to commensurability effects at matching vortex and defect densities. Such commensurability effects have been primarily studied in metallic superconductors using arrays of holes (antidots)^{13–19} or magnetic dots²⁰ in the material, nanogrooves,^{21–23} and superlattices²⁴ but are also found in YBCO perforated with holes.²⁵

The fabrication techniques of pinning arrays in our samples are based on the observation that irradiation of YBCO thin films with He^+ ions of moderate energy introduces point defects by displacing mainly oxygen atoms. This leads to a reduction of the transition temperature T_c ,²⁶ which can be well controlled by the ion fluence.^{6,27–29} By ion irradiation through a shadow mask^{30–38} or using the focused ion beam of a He ion microscope (HIM)³⁹ an array of CDs can be created that acts as a pinning landscape for vortices.

Only few investigations have addressed the angular dependence of vortex commensurability effects in metallic superconductors with antidots^{16,40} and in YBCO thin films patterned with periodic CDs by ion irradiation.^{34,37}

The purpose of this study is to explore whether the pinning landscapes created in YBCO by focused He^+ ion irradiation in a HIM act as 1D line-like pinning centers despite of consisting of 0D point defect clusters with inhomogeneous density.

2. EXPERIMENTAL METHODS

Epitaxial thin films of $\text{YBa}_2\text{Cu}_3\text{O}_{7-\delta}$ are grown on (100) MgO single-crystal substrates by pulsed-laser deposition using 248 nm KrF-excimer-laser radiation at a fluence of 3.2 J/cm². The thicknesses of the films used in this work are $t_s = (80 \pm 5)$ nm (sample SQ200) and $t_s = (210 \pm 10)$ nm (sample SQ500). The critical temperatures of the as-prepared films are $T_c \sim 90$ K with transition

widths $\Delta T_c \sim 1$ K. The films are patterned by photolithography and wet chemical etching to form bridges with a length of 240 μm and a width of $w = 60$ μm . Electrical contacts in a four-probe geometry are established on side arms of the bridges using sputtered Au pads with a voltage probe distance of 100 μm .

In both samples, a tailored vortex pinning landscape was created by different methods of He^+ ion irradiation. Sample SQ200 was irradiated with an intentionally defocused ion beam in a HIM. The setup starts with adjusting the HIM settings to the highest resolution and then changing the working distance (beam focus plane) so that the beam hits the sample surface with a nearly Gaussian fluence profile⁴¹ with a full width at half maximum (FWHM) of about 50 nm. Since the aperture angle of the ion beam is very small the ion beam hits the sample surface almost orthogonally. The method is described in detail elsewhere.³⁹

By sequentially scanning the ion beam over the sample surface, a square lattice of columnar defects with $d = 200$ nm spacings is created in the thin YBCO film in an overall area of approximately $200 \mu\text{m} \times 100 \mu\text{m}$. Every point is irradiated with 30 keV He^+ ions with a dwell time of 2.7 ms and a beam current of 3 pA, corresponding to ~ 51000 He^+ ions/point. The method is sketched in Fig. 1(a).

Sample SQ500 is patterned by masked ion beam structuring (MIBS)³⁰ as sketched in Fig. 1(b). A 2 μm -thick Si stencil mask is placed on top of the YBCO film and adjusted in an optical microscope with the help of marker holes. The mask is separated from the surface of the YBCO film by a circumferential spacer layer made of 1.5 μm -thick photoresist. The stencil mask is perforated with holes with diameters $D = (180 \pm 5)$ nm, arranged in a square array of $d = (500 \pm 2)$ nm pitch, which covers the entire bridge. The stencil pattern is shadow projected onto the YBCO surface by irradiating the arrangement with a collinear 75 keV He^+ ion beam, oriented orthogonal to the sample surface, in a commercial ion implanter (High Voltage Engineering Europa B. V.).

Electrical transport measurements are performed in a closed-cycle cryocooler with temperature control by a Cernox resistor, which has a negligible temperature reading error in moderate magnetic fields.⁴² The applied magnetic field \mathbf{B}_a is supplied by a revolvable electromagnet with $\pm 1^\circ$ angular resolution and $B_a = |\mathbf{B}_a|$ is measured by a calibrated Hall probe mounted between the magnet's pole pieces. The Hall probe is connected to a LakeShore 475 gaussmeter, allowing for measurements of \mathbf{B}_a with a zero offset < 10 μT , and a reading accuracy $< 0.1\%$. The tilt angle α is defined as the angle between the surface normal of the YBCO film and the direction of \mathbf{B}_a . The angle-dependent magneto-resistance measurements are performed in constant Lorentz force geometry, i. e., the magnetic field is always perpendicular to the current direction. For all measurements, the current I through the sample is generated by a constant-current source in both polarities to eliminate thermoelectric signals and the voltage V is measured by a Keithley 2182A nano-voltmeter. The critical current $I_c(B_a)$ is determined from isothermal current-voltage (I - V) measurements with a voltage criterion of 100 nV, corresponding to 10 $\mu\text{V}/\text{cm}$. Since the I - V characteristics of a superconductor are nonlinear the resistance curves presented below are defined as $R(B_a) = V(B_a)/I$ at a fixed I . Note that the absolute value of $R(B_a)$ is not important for our analyses.

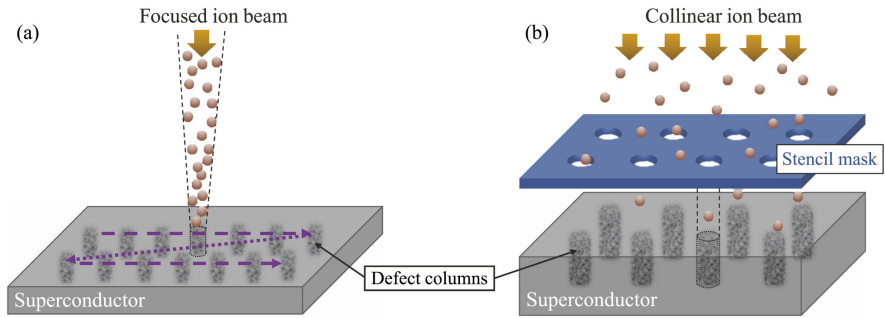


FIG. 1. Two different methods for patterning a YBCO film by He^+ ion irradiation: (a) Irradiation with a slightly defocused beam of a helium-ion microscope produces tailored columnar defect patterns by scanning the beam over the sample surface. The dark regions indicate the defect-rich, nonsuperconducting nanocylinders. (b) Ion beam direct patterning by irradiating through a stencil mask creates a large number of columnar defects in a single step.

3. RESULTS AND DISCUSSION

To compare the shapes of the artificial CD lattices, prepared by the two different irradiation methods, simulations of the defect distributions with the program package SRIM/TRIM^{43,44} are performed. It computes the impact of ions on solids using a binary collision approximation of ion-atom and atom-atom collisions, and delivers the full collision cascades. However, ion channeling, thermal effects, diffusion, and recrystallization are not considered.

Details of the crystallographic structure are not considered in SRIM/TRIM as it uses a Monte Carlo method and assumes amorphous targets. For the spatial modulation of superconductivity, the Ginzburg–Landau coherence length is the relevant length parameter and therefore we have determined the average defect density within calculation cells of $2 \times 2 \times 2 \text{ nm}^3$ —a length scale of the order of the in-plane coherence length of YBCO. Note that the investigated point defect densities are below the amorphization limit and a comparison to an experimental visualization is hardly possible. Only by using a larger ion fluence, amorphous channels can be created and detected in cross-section scanning transmission electron microscopy images.⁴⁵

The pinning potential for vortices is provided by a local suppression of T_c , which can be calculated from the defect density on the grounds of the pair-breaking theory of Abrikosov and Gor'kov.⁴⁶ Since annealing effects are not considered in SRIM/TRIM and various other effects may lead to substantial uncertainty, a “calibration” curve relating the experimentally observed T_c to the defect density from the simulations is established, using previous experimental T_c values from full-area irradiation of thin YBCO films.²⁸ Details of this procedure are described elsewhere.⁴⁷

The resulting simulated cross-sectional T_c profiles for the two samples SQ200 and SQ500 are presented in Fig. 2 at the same scale for comparison. Note that sample SQ200 (top panel) was irradiated with a slightly defocused He^+ ion beam with approximately Gaussian normal distributed fluence of FWHM = 50 nm, whereas

the fluence was homogeneous in the irradiated parts of sample SQ500. Another important difference is the ion energy of 30 keV for sample SQ200 and 75 keV for sample SQ500.

In thin films with $t_z \leq 80 \text{ nm}$, 30 keV He^+ ion irradiation creates columns, within which T_c is suppressed, that are clearly separated from each other at 200 nm lattice spacing (Fig. 2, top panel). The suppression of T_c at the fringes of the CDs decays more gradually than for sample SQ500, which was irradiated by MIBS (Fig. 2, bottom panel). Still, the cylindrical envelope of clusters with suppressed T_c provides an efficient pinning landscape as will be discussed below.

Due to the larger penetration depth of the 75 keV He^+ ions, CDs can be patterned into thicker YBCO films with MIBS, as demonstrated in Fig. 2, bottom panel. However, the achievable lateral resolution for CD diameters degrades with increasing thickness of the film, as it can be noticed by the increasing diameter of the CD for film thicknesses larger than 120 nm. We note that increasing the ion energy would improve the resolution on the cost of a lower ion scattering cross-section, which would demand a higher ion fluence.

Although a few dispersed defects are created also outside the CDs by lateral straggling of the incident ions and the secondary collision cascades, their impact on the zero-field electrical transport properties is marginal as demonstrated by the experimentally determined small reduction of the critical temperature $\Delta T_c = 2.6 \text{ K}$ ($\Delta T_c = 4 \text{ K}$) in sample SQ200 (SQ500) after irradiation.

In electric transport measurements, the commensurability effects evoked by regular pinning lattices are demonstrated in Fig. 3 as peaks in the critical current I_c and corresponding minima of the resistance vs applied field B_a (at $\alpha = 0^\circ$) that appear exactly at the matching fields

$$B_n = n \frac{\Phi_0}{d^2}, \quad (1)$$

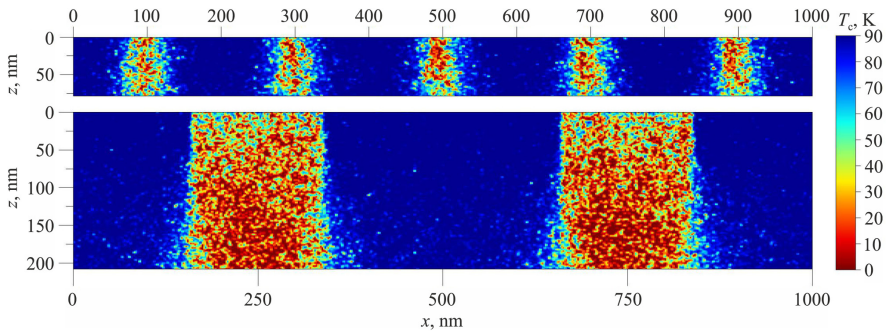


FIG. 2. Cross-sectional view of calculated local T_c profiles within and around the defect columns produced by 50900 ions per dot with 30 keV energy and a Gaussian normal distribution with 50 nm FWHM (sample SQ200, top panel) and 75 keV He^+ ion irradiation of YBCO with a fluence of $3 \cdot 10^{15} \text{ cm}^{-2}$ (sample SQ500, bottom panel). Both panels are displayed at the same scale for a comparison between the two samples.

where n is a rational number. We use $n=0$ to denote the absence of vortices and $n < 0$ for the reversed vortex orientation. When the diameters of the CDs are larger than the Ginzburg-Landau coherence length, an integer number $n > 1$ of fluxons can be accommodated per CD.⁴⁸ Note the tiny humps of I_c around $\pm 26 \text{ mT}$ that indicate a fractional matching pattern with $n = \pm(1/2)$.

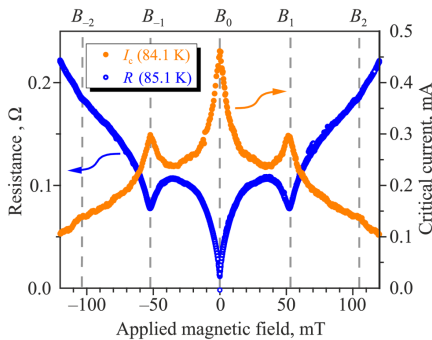


FIG. 3. Resistance $R(I=50 \mu\text{A})$ and critical current I_c vs applied magnetic field at $\alpha = 0^\circ$ of an 80-nm thick YBCO film (sample SQ200), irradiated with a slightly defocused He^+ ion beam of 50 nm FWHM to form a square pattern of defect cylinders with a lattice constant of 200 nm. Data were taken after zero-field cooling and then sweeping the field through a full cycle, revealing no hysteresis. The matching field determined from the geometric parameters is $B_1 = 52 \text{ mT}$ and leads to a minimum of the resistance and a peak in the critical current.

The commensurability effects result from two different vortex pinning mechanisms in our samples. On the one hand, n flux quanta can be trapped in the normal-conducting core of a CD, which we will call fluxons to discriminate them from the regular Abrikosov vortices in a plain superconductor. These fluxons remain pinned at the CDs even if a moderate current is applied to the sample. However, by changing the applied magnetic field, the Lorentz force due to increased shielding current exceeds the pinning potential and the fluxons can hop between neighboring CDs.⁴⁹

On the other hand, vortices at interstitial positions between the CDs are pinned mainly by twin boundaries and growth defects in the YBCO films, most of them oriented parallel to the c axis.⁵⁰ Their pinning potentials are usually weaker than those of the fluxons trapped in the CDs. At a certain applied magnetic field B_a the critical current shows a peak when the magnetic flux through the sample is penetrating the sample via single fluxons trapped in each CD, which happens exactly at the matching field B_1 of Eq. (1). In this situation, the number of weakly-pinned interstitial vortices is minimized. An equivalent consideration leads to the explanation of the resistance minima observed at the same B_n . Typically, our samples patterned by masked or focused He ion irradiation show clear matching effects in a temperature range from $\sim 0.7T_c$ up to $\sim 0.9T_c$.^{36,39} For our further considerations, it is important that the matching fields can be equally well determined from either I_c peaks or resistance minima, the latter allowing for much faster measurements.

An investigation of the angular dependence of the magnetoresistance can shed light on the nature and relative strength of the pinning of fluxons at the CDs and the pinning of interstitial vortices, respectively.

For dominant pinning at CDs, the magnetic flux should be preferentially trapped within the CDs irrespectively of the angle α

by which the applied magnetic field B_a is tilted off the axes of the CDs. Then, the commensurability peaks in $I_c(B_a)$ and dips in $R(B_a)$ should appear if the component of B_a that is parallel to the axes of the CDs,

$$B_{\parallel} = B_a \cos \alpha, \tag{2}$$

fulfills the matching condition of Eq. (1).

Figure 4 shows the magnetoresistance of sample SQ200 for various tilt angles α at a temperature near the onset of dissipation. When the magnetic field B_a is oriented orthogonal to the sample surface and parallel to the axes of the CDs ($\alpha = 0^\circ$) a distinct minimum at $B_1 = 52$ mT and a marginal one at $B_2 = 104$ mT confirms the commensurability effects. With increasing tilt angle α the magnetoresistance curves exhibit very similar matching resistance minima and change their shapes only slightly if data are plotted with the abscissa scaled to B_{\parallel} . Even at $\alpha = 70^\circ$ the commensurability effect can be detected.

In sample SQ500 the situation is more complicated due to a hysteresis observed in the magnetic field sweeps. It originates from an unconventional terraced critical state⁵¹ with domains in the sample⁵² inside which the pinning centers are occupied by the same number n of fluxons and neighboring domains by $n \pm 1$. Such a hysteretic behavior has been investigated previously⁵⁶ and is beyond the scope of this work. Still, the considerations leading to Eq. (2) should hold. Indeed, Fig. 5 demonstrates that all the features observed in the $\alpha = 0^\circ$ orientation of B_a appear at the same positions when the magnetic field is tilted and scaling to B_{\parallel} is used. This not only applies to the first matching fields in up-sweep (B_{-1}^{\uparrow}) and down-sweep (B_1^{\downarrow}) conditions, but also to the hysteretic displacement of the minima with zero fluxon occupation of the relevant

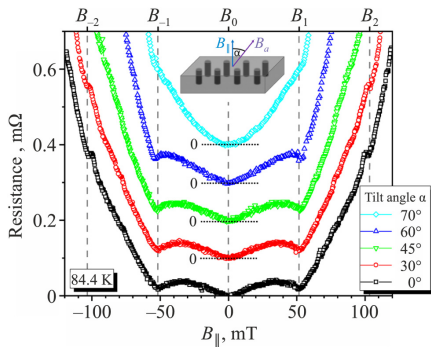


FIG. 4. Resistance ($I = 400 \mu\text{A}$) vs applied field component along the normal of the film surface B_{\parallel} of sample SQ200 for different values of α . Since no hysteresis is observed, only the down sweep branches of the cycle after zero-field cooling are displayed. For $\alpha > 0^\circ$ the curves are shifted by multiples of $0.1 \text{ m}\Omega$ to enhance visibility. The inset shows a sketch of the experimental situation.

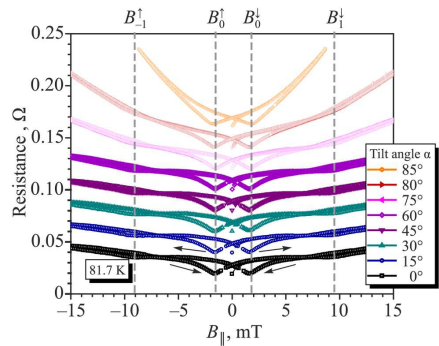


FIG. 5. Resistance ($I = 200 \mu\text{A}$) vs applied field component along the normal of the film surface B_{\parallel} of sample SQ500 for different values of α . Data were taken after zero-field cooling and comprise the virgin curves starting from $B = 0$ and the up and down sweeps as representatively indicated by arrows in the bottom curve. Data for $\alpha > 0^\circ$ are shifted by multiples of 0.02Ω .

CDs (B_{-1}^{\uparrow} and B_0^{\downarrow}). Despite of the more complex fluxon arrangements in this sample, all commensurability effects are governed by B_{\parallel} , which confirms that only the component of the magnetic field is relevant that is parallel to the axes of the CDs.

In Fig. 6 the magnetic field components B_{\parallel} at which the resistance dips for single fluxon matching are observed in sample

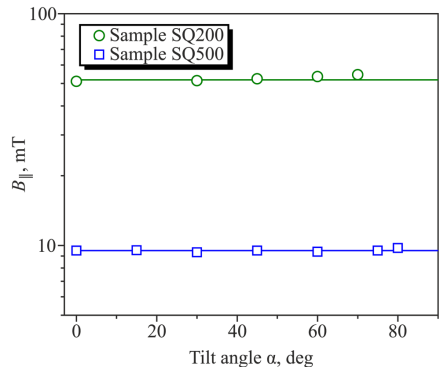


FIG. 6. Angular dependencies of the magnetic field components B_{\parallel} at which the resistance dips for single fluxon matching (sample SQ200) and B_{\parallel} (sample SQ500) are observed. The horizontal lines indicate that B_{\parallel} determines the matching effect, irrespective of the tilt angle α .

SQ200 (B_1) and SQ500 (B_1^*) are shown as a function of the tilt angle α . In remarkable agreement with Eq. (2) the experimental values are independent of α as indicated by the horizontal lines. This confirms that at all angles shown in the graph the magnetic flux is penetrated along the CDs. In addition, the adherence to Eq. (2) up to large tilt angles indicates that pinning at the CDs is much stronger than the intrinsic pinning of interstitial vortices in the intermediate regions between the CDs.

Some deviations from the behavior presented in Fig. 6 have been reported in denser pinning lattices. Due to lateral straggling of the collision cascades, a significant number of irradiation defects are created in the spaces between the CDs. This is indicated by $\Delta T_c = 43$ K after MIBS irradiation. In this case the scaling according to Eq. (2) gradually breaks down for $\alpha > 45^\circ$.²⁷ In thin YBCO films patterned via 110 keV O^+ ion irradiation ($\Delta T_c \approx 40$ K) a strong modification of the vortex-glass transition and a weakening of the vortex correlations along the c axis has been observed.³⁴

Finally, in unirradiated YBCO, due to its anisotropy, the cylindrical vortices change to an elliptical cross-section in oblique magnetic fields $\alpha \neq 0^\circ$ and decompose into a tilted stack of pancake vortices at tilt angles $\alpha \lesssim 54^\circ$.⁵³ This is reflected by a broad maximum in the critical current extending over a range $\alpha \lesssim 60^\circ$.¹¹ The feature evolves at temperatures closer to T_c and in moderate magnetic fields. In contrast to the observations in those unirradiated YBCO films, the matching fields B_1 in our samples strictly scale with Eq. (2) up to $\alpha = 72^\circ$ ($\alpha = 80^\circ$) for sample SQ200 (SQ500). Naturally, no pinning of fluxons by the CDs is expected when the CDs and B_1 are oriented orthogonally, i.e., near $\alpha = 90^\circ$.

4. CONCLUSIONS

Vortex pinning landscapes in YBCO thin films can be conveniently fabricated by employing He^+ ion irradiation, either by a focused beam in a HIM or by shadow-masking of a wide-field ion beam. As demonstrated by simulations of the defect distributions created in YBCO by the ion impact, the methods are complementary. HIM irradiation is a sequential method and allows for mask-less operation and higher resolution of at least 10 nm,⁴⁵ but the penetration depth is limited to about 80 nm due to the maximum ion energy of 30 keV. With MIBS the entire pattern can be prepared at the same time and also in thicker films when using higher ion energies, but the lateral resolution is currently limited by a hole diameter of ~ 180 nm of the available stencil masks.

Both methods, despite of their different length scales, produce well-defined CDs that provide strong pinning of fluxons, which is supported by the observation that at arbitrary angles of an applied magnetic field only the component parallel to the CDs governs the commensurability effects. Both irradiation methods appear suitable for the creation of well-defined tailored pinning landscapes in cuprate superconductors, which are an important prerequisite for proposed concepts of fluxon manipulation leading to fast and low-dissipation devices.^{54–56}

ACKNOWLEDGMENTS

Research was conducted within the framework of the COST Action CA16218 (NANOCOHYBRI) of the European Cooperation in Science and Technology. B.M. acknowledges funding by the

German Academic Scholarship Foundation. M.D. acknowledges the European Erasmus Mundus (Target II) program for financial support.

REFERENCES

- ¹N. Kobayashi, H. Iwasaki, S. Terada, K. Noto, A. Tokiwa, M. Kikuchi, Y. Syono, and Y. Muto, *Phys. Rev. B* **43**, 7837 (1991).
- ²J. R. Clem, *Phys. Rev. B* **43**, 7837 (1991).
- ³A. Correa, F. Mompéan, I. Guillamón, E. Herrera, M. García-Hernández, T. Yamamoto, T. Kashiwagi, K. Kadowaki, A. I. Buzdin, H. Suderow, and C. Munuera, *Commun. Phys.* **2**, 31 (2019).
- ⁴T. Haugan, P. N. Barnes, R. Wheeler, F. Meisenkothen, and M. Sumption, *Nature* **430**, 867 (2004).
- ⁵R. V. Vovk, G. Y. Khadzhai, and O. V. Dobrovolskiy, *J. Mater. Sci. Mater. Electron.* **30**, 241 (2019).
- ⁶W. Lang and J. D. Pedarnig, "Ion irradiation of high-temperature superconductors and its application for nanopatterning," in *Nanoscience and Engineering in Superconductivity*, edited by V. V. Moshchalkov, R. Wördenweber, and W. Lang (Springer, Heidelberg, 2010), p. 81.
- ⁷L. Civale, *Supercond. Sci. Technol.* **10**, A11 (1997).
- ⁸B. Holzapfel, G. Kreiselmeyer, M. Kraus, S. Bouffard, S. Klauumenzler, L. Schultz, and G. Saemann-Ischenko, *Phys. Rev. B* **48**, 600 (1993).
- ⁹R. Prozorov, A. T. Fiory, A. F. Hebard, and S. Somekh, *Appl. Phys. Lett.* **32**, 73 (1978).
- ¹⁰A. N. Lykov, *Solid State Commun.* **86**, 531 (1993).
- ¹¹V. V. Metlushko, M. Baert, R. Jonckheere, V. V. Moshchalkov, and Y. Bruynseraede, *Solid State Commun.* **91**, 331 (1994).
- ¹²V. V. Metlushko, L. E. DeLong, M. Baert, E. Rosseel, M. J. Van Bael, K. Temst, V. V. Moshchalkov, and Y. Bruynseraede, *Europhys. Lett.* **41**, 333 (1998).
- ¹³M. Kemmler, C. Gürlich, A. Sterck, H. Pöhlner, M. Neuhaus, M. Siegel, R. Kleiner, and D. Koelle, *Phys. Rev. Lett.* **97**, 147003 (2006).
- ¹⁴V. R. Misko, D. Bothner, M. Kemmler, R. Kleiner, D. Koelle, F. M. Peeters, and F. Nori, *Phys. Rev. B* **82**, 184512 (2010).
- ¹⁵V. V. Moshchalkov and J. Fritzsche, *Nanostructured Superconductors* (World Scientific, Singapore, 2011).
- ¹⁶M. Vélez, J. I. Martin, J. E. Villegas, A. Hoffmann, E. M. González, J. L. Vicent, and I. K. Schuller, *J. Magn. Magn. Mater.* **320**, 2547 (2008), and references therein.
- ¹⁷V. A. Shklovskij and O. V. Dobrovolskiy, *Phys. Rev. B* **74**, 104511 (2006).
- ¹⁸V. A. Shklovskij and O. V. Dobrovolskiy, *Phys. Rev. B* **78**, 104526 (2008).
- ¹⁹O. V. Dobrovolskiy, E. Begun, M. Huth, and V. A. Shklovskij, *New J. Phys.* **14**, 113027 (2012).
- ²⁰O. V. Dobrovolskiy, V. M. Bevs, M. Y. Mikhailov, O. L. Yuzepovich, V. A. Shklovskij, R. V. Vovk, M. I. Tsidikht, R. Sachser, and M. Huth, *Nat. Commun.* **9**, 4927 (2018).
- ²¹A. Castellanos, R. Wördenweber, G. Ockenfuss, A. v. d. Hart, and K. Keck, *Appl. Phys. Lett.* **71**, 962 (1997).
- ²²X. Z. Wang, B. Hellebrand, D. Bäuerle, M. Strecker, G. Wortmann, and W. Lang, *Physica C* **242**, 55 (1995).
- ²³Z. Sefrioui, D. Arias, E. M. González, C. León, J. Santamaría, and J. L. Vicent, *Phys. Rev. B* **63**, 064503 (2001).
- ²⁴W. Lang, T. Enzenhofer, M. Peruzzi, J. D. Pedarnig, D. Bäuerle, C. Horner, E. Cekan, E. Platzgummer, and H. Loeschner, *Inst. Phys. Conf. Ser.* **181**, 1549 (2004).
- ²⁵S. A. Cybart, P. X. T. Yen, E. Y. Cho, J. U. Huh, V. N. Glyantsev, C. S. Yung, B. Moeckly, J. W. Beeman, and R. C. Dynes, *IEEE Trans. Appl. Supercond.* **24**, 1 (2014).

- ³⁰W. Lang, M. Dineva, M. Marksteiner, T. Enzenhofer, K. Siraj, M. Peruzzi, J. D. Pedarnig, D. Bäuerle, R. Korntner, E. Cekan, E. Platzgummer, and H. Loeschner, *Microelectron. Eng.* **83**, 1495 (2006).
- ³¹W. Lang, H. Richter, M. Marksteiner, K. Siraj, M. A. Bodea, J. D. Pedarnig, C. Grigoropoulos, D. Bäuerle, C. Hasenfuss, L. Palmethofer, R. Kolarova, and P. Bauer, *Int. J. Nanotechnol.* **6**, 704 (2009).
- ³²J. D. Pedarnig, K. Siraj, M. A. Bodea, I. Puica, W. Lang, R. Kolarova, P. Bauer, K. Haselgrübler, C. Hasenfuss, I. Beinik, and C. Teichert, *Thin Solid Films* **518**, 7075 (2010).
- ³³I. Swiecicki, C. Ulysse, T. Wolf, R. Bernard, N. Bergeal, J. Briatico, G. Faini, J. Lesueur, and J. E. Villegas, *Phys. Rev. B* **85**, 224502 (2012).
- ³⁴J. Trastoy, V. Rouco, C. Ulysse, R. Bernard, A. Palau, T. Puig, G. Faini, J. Lesueur, J. Briatico, and J. E. Villegas, *New J. Phys.* **15**, 103022 (2013).
- ³⁵L. T. Haag, G. Zechner, W. Lang, M. Dosmailov, M. A. Bodea, and J. D. Pedarnig, *Physica C* **503**, 75 (2014).
- ³⁶G. Zechner, F. Jausner, L. T. Haag, W. Lang, M. Dosmailov, M. A. Bodea, and J. D. Pedarnig, *Phys. Rev. Appl.* **8**, 014021 (2017).
- ³⁷G. Zechner, K. L. Mletschnig, W. Lang, M. Dosmailov, M. A. Bodea, and J. D. Pedarnig, *Supercond. Sci. Technol.* **31**, 044002 (2018).
- ³⁸G. Zechner, W. Lang, M. Dosmailov, M. A. Bodea, and J. D. Pedarnig, *Phys. Rev. B* **98**, 104508 (2018).
- ³⁹B. Aichner, B. Müller, M. Karrer, V. R. Misko, F. Limberger, K. L. Mletschnig, M. Dosmailov, J. D. Pedarnig, F. Nori, R. Kleiner, D. Koelle, and W. Lang, *ACS Appl. Nano Mater.* **2**, 5108 (2019).
- ⁴⁰E. N. Womack, P. W. Adams, J. M. Valles, and G. Catelani, *Phys. Rev. B* **100**, 174505 (2019).
- ⁴¹D. Emmrich, A. Beyer, A. Nadzeyka, S. Bauerdick, J. C. Meyer, J. Kotakoski, and A. Götzhäuser, *Appl. Phys. Lett.* **108**, 163103 (2016).
- ⁴²G. Heine and W. Lang, *Cryogenics* **38**, 377 (1998).
- ⁴³J. F. Ziegler, U. Littmark, and J. P. Biersack, *The Stopping and Range of Ions in Solids* (Pergamon, New York, 1985).
- ⁴⁴J. F. Ziegler, M. D. Ziegler, and J. P. Biersack, *Nucl. Instrum. Methods Phys. Res., Sect. B* **268**, 1818 (2010).
- ⁴⁵B. Müller, M. Karrer, F. Limberger, M. Becker, B. Schröppel, C. J. Burkhardt, R. Kleiner, E. Goldobin, and D. Koelle, *Phys. Rev. Appl.* **11**, 044082 (2019).
- ⁴⁶A. A. Abrikosov and L. P. Gor'kov, *Zh. Eksp. Teor. Fiz.* **39**, 1781 (1960) [*Sov. Phys. JETP* **12**, 1243 (1961)].
- ⁴⁷K. L. Mletschnig and W. Lang, *Microelectron. Eng.* **215**, 110982 (2019).
- ⁴⁸A. I. Buzdin, *Phys. Rev. B* **47**, 11416 (1993).
- ⁴⁹M. P. Sørensen, N. F. Pedersen, and M. Ögren, *Physica C* **533**, 40 (2017).
- ⁵⁰B. Dam, J. M. Huijbregtse, F. C. Klaassen, R. C. F. van-der Geest, G. Doornbos, J. H. Rector, A. M. Testa, S. Freisem, J. C. Martinez, B. Stäuble-Pümpin, and R. Griessen, *Nature* **399**, 439 (1999).
- ⁵¹L. D. Cooley and A. M. Grishin, *Phys. Rev. Lett.* **74**, 2788 (1995).
- ⁵²C. Reichhardt, J. Groth, C. J. Olson, S. B. Field, and F. Nori, *Phys. Rev. B* **54**, 16108 (1996); *Erratum: Phys. Rev. B* **56**, 14196 (1997).
- ⁵³G. Blatter, M. Feigel'man, V. Geshkenbein, A. Larkin, and V. Vinokur, *Rev. Mod. Phys.* **66**, 1125 (1994).
- ⁵⁴J. F. Wambaugh, C. Reichhardt, C. J. Olson, F. Marchesoni, and F. Nori, *Phys. Rev. Lett.* **83**, 5106 (1999).
- ⁵⁵M. B. Hastings, C. J. Olson Reichhardt, and C. Reichhardt, *Phys. Rev. Lett.* **90**, 247004 (2003).
- ⁵⁶M. V. Milošević, G. R. Berdiyrov, and F. M. Peeters, *Appl. Phys. Lett.* **91**, 212501 (2007).

Translated by [AIP Author Services](#)

Publication 5

Reprinted with permission from
L. Backmeister et al., *Nanomaterials* **12**, 3491 (2022)
Copyright © 2022 by the Authors.



Article

Ordered Bose Glass of Vortices in Superconducting $\text{YBa}_2\text{Cu}_3\text{O}_{7-\delta}$ Thin Films with a Periodic Pin Lattice Created by Focused Helium Ion Irradiation

Lucas Backmeister ¹, Bernd Aichner ¹, Max Karrer ², Katja Wurster ², Reinhold Kleiner ², Edward Goldobin ², Dieter Koelle ², Wolfgang Lang ^{1,*}

¹ Faculty of Physics, University of Vienna, A-1090 Wien, Austria

² Physikalisches Institut, Center for Quantum Science (CQ) and LISA⁺, Universität Tübingen, D-72076 Tübingen, Germany

* Correspondence: wolfgang.lang@univie.ac.at

Abstract: The defect-rich morphology of $\text{YBa}_2\text{Cu}_3\text{O}_{7-\delta}$ (YBCO) thin films leads to a glass-like arrangement of Abrikosov vortices which causes the resistance to disappear in vanishing current densities. This vortex glass consists of entangled vortex lines and is identified by a characteristic scaling of the voltage–current isotherms. Randomly distributed columnar defects stratify the vortex lines and lead to a Bose glass. Here, we report on the observation of an *ordered Bose glass* in a YBCO thin film with a hexagonal array of columnar defects with 30 nm spacings. The periodic pinning landscape was engineered by a focused beam of 30 keV He^+ ions in a helium-ion microscope.

Keywords: copper-oxide superconductors; vortex glass; *ordered Bose glass*; vortex matching; voltage–current isotherms; helium-ion microscope



Citation: Backmeister, L.; Aichner, B.; Karrer, M.; Wurster, K.; Kleiner, R.; Goldobin, E.; Koelle, D.; Lang, W. Ordered Bose Glass of Vortices in Superconducting $\text{YBa}_2\text{Cu}_3\text{O}_{7-\delta}$ Thin Films with a Periodic Pin Lattice Created by Focused Helium Ion Irradiation. *Nanomaterials* **2022**, *12*, 3491. <https://doi.org/10.3390/nano12193491>

Academic Editor: M.V. Ramallo

Received: 14 September 2022

Accepted: 2 October 2022

Published: 6 October 2022

Publisher's Note: MDPI stays neutral with regard to jurisdictional claims in published maps and institutional affiliations.



Copyright: © 2022 by the authors. Licensee MDPI, Basel, Switzerland. This article is an open access article distributed under the terms and conditions of the Creative Commons Attribution (CC BY) license (<https://creativecommons.org/licenses/by/4.0/>).

1. Introduction

The copper oxide high-temperature superconductors (HTS) are in the extreme type-II limit, with a minor lower critical field B_{c1} and a high upper critical field B_{c2} . The large difference in the critical fields spans a vast area in the phase diagram, the mixed state. The magnetic flux enters as Abrikosov vortices, quantized portions of flux $\Phi_0 = h/2e$, where h is the Planck constant and e is the elementary charge. The mixed state in HTS exhibits qualitatively new phenomenology [1] and is the predominant operating condition for most applications of these materials. Therefore, it is of utmost importance under which experimental conditions zero resistance, the hallmark of superconductivity, can be achieved. Moreover, the parameter space for utilizing superconductivity is limited by the critical temperature T_c , the upper critical field B_{c2} , and the critical current density j_c . The latter can be enhanced by various pinning mechanisms that block the dissipative motion of the vortices [2,3]. In HTS, the boundaries of this simple picture are substantially blurred by strong thermodynamic fluctuations of the superconducting order parameter.

In particular, the question of whether one can observe a genuine zero-resistance state at a finite temperature or only at zero temperature has raised much interest. Following the flux-creep theory of Anderson and Kim [4,5], or the thermally-assisted flux-flow model (TAFF) [6], one has to conclude that the resistance remains finite, even when the current density $j \rightarrow 0$. Indeed, voltage–current (V - I) isotherms in the mixed state of many HTS reveal an ohmic behavior down to the lowest experimentally accessible voltages at temperatures not too far below T_c . This observation is attributed to TAFF. Numerical simulations reveal a rich variety of different dynamic phases when a vortex ensemble is driven over a background of correlated or random pinning defects [7].

The minuscule coherence lengths in HTS and the importance of intrinsic randomly distributed defects have triggered theoretical proposals of a thermodynamic equilibrium

phase with a glass-like arrangement of vortices. Different theories have been proposed for randomly distributed pinning defects, depending on their dimensionality: the vortex-glass (VG) model for point-like defects [8,9] and the Bose-glass (BG) model for columnar defects penetrating the entire sample thickness [10,11].

The VG model has been confirmed by scaling of DC-current V - I isotherms in a variety of HTS, among them $\text{YBa}_2\text{Cu}_3\text{O}_{7-\delta}$ (YBCO) in the shape of optimally doped thin films [12], oxygen-deficient films [13], ultrathin films [14], and single crystals [15]. In addition, in the highly anisotropic compound $\text{Bi}_2\text{Sr}_2\text{CaCu}_2\text{O}_8$ (BSCCO-2212), an agreement with the VG theory was found in single crystals [16] and thin films [17]. A transition from $D = 3$ to $D = 2$ VG scaling was reported in oxygen-depleted YBCO films [18]. In addition, phase-resolved AC impedance measurements have provided another route to estimate the dynamic VG parameter z_{VG} [19].

The above considerations relate to defects in HTS that are not correlated along the crystallographic c axis. In contrast, columnar defects (CDs) change the underlying physics, leading to a Bose glass [10,11]. For instance, irradiation with swift heavy ions produces cylindrical channels of amorphous material that act as c -axis correlated pinning sites and evoke a BG behavior [20]. The fact that planar defects oriented parallel to the c axis are ubiquitous in thin YBCO films can lead to inconsistent observations of VG [21] or BG [22] behavior, depending on the details of the material's morphology. Moreover, earlier investigations of engineered nano-inclusions of different dimensionality have reported a crossover between VG and BG behavior [23]. For example, the latter was found for disordered BaZrO_3 nanorods in YBCO.

The transitions between these various vortex phases, governed by temperature, magnetic field, and disorder, are long-standing issues. One aspect of the problem is that in earlier experiments, no periodic engineered pinning sites were available with spacings smaller than the London penetration depth and pronounced vortex pinning effects down to low temperatures.

Recent advances in nanopatterning of HTS by masked or focused light-ion irradiation [24–27] allow for the engineering of CDs with a periodic arrangement [27–33]. Using YBCO thin films with an unprecedented dense hexagonal lattice of CDs, created by focused He^+ -ion-beam irradiation, allows us to observe a novel kind of glassy vortex correlations, which we will call an *ordered Bose glass* (OBG). This paper explores the OBG phase by measuring the V - I isotherms at various temperatures and magnetic fields.

2. Theoretical Background

Both vortex and Bose glasses form below a magnetic-field-dependent glass temperature $T_g(B) < T_c$ that marks a bifurcation between two essentially different domains of voltage-current (V - I) isotherms. While at $T > T_g(B)$ ohmic characteristics prevail down to vanishing j , the zero-resistance state emerges at $T < T_g(B)$ already at finite j . More importantly, the theories predict a critical scaling of several physical parameters at the continuous second-order phase transition between vortex or Bose glass and vortex liquid. In a VG, the central parameter is the glass correlation length $\xi_{VG} \propto |T - T_g|^{-\nu}$, which is determined by the size of glassy islands and of fluctuating vortex liquid droplets above and below $T_g(B)$. The lifetime of these fluctuations is $\tau \propto \xi_{VG}^z \propto |T - T_g|^{-\nu z}$.

The theoretical predictions can be experimentally verified by measuring V - I isotherms near the VG transition and by comparing the data to the relation

$$\frac{V}{I} \propto \tilde{\xi}_{VG}^{D-2-z} \tilde{\mathfrak{F}}_{\pm} \left(\frac{I \tilde{\xi}_{VG}^{D-1} \Phi_0}{k_B T} \right), \quad (1)$$

where $\tilde{\mathfrak{F}}_{\pm}$ are two universal, yet unknown, characteristic functions of a specific VG system above ($\tilde{\mathfrak{F}}_+$) and below ($\tilde{\mathfrak{F}}_-$) $T_g(B)$, respectively, D is the dimensionality of the vortex

ensemble, and k_B is the Boltzmann constant. By appropriately scaling a set of V - I isotherms according to

$$(V/I)|1 - T/T_g|^{v_{VG}(D-2-z_{VG})} = \mathfrak{F}_{\pm}[(I/T)|1 - T/T_g|^{v_{VG}(1-D)}], \quad (2)$$

collected at various temperatures and at fixed B , all curves collapse onto the two universal \mathfrak{F}_{\pm} branches. The scaling is achieved by a proper choice of the parameters T_g , v_{VG} , and z_{VG} . The bifurcation line right at T_g not only separates the branches \mathfrak{F}_{\pm} but also obeys a power law.

$$(V/I)|_{T=T_g} \propto I^{(z_{VG}+2-D)/(D-1)}. \quad (3)$$

Note that the BG theory predicts a similar scaling of the V - I isotherms that can be cast into the same Equation (2). Since a BG requires 3D correlations, the respective critical exponents of a 3D-VG can be transformed to those of a BG by [21]

$$v_{BG} = \frac{2v_{VG}}{3} \quad \text{and} \quad z_{BG} = \frac{3z_{VG} + 1}{2}. \quad (4)$$

The VG and BG theories were developed for randomly arranged point and columnar defects, respectively. A new and unique situation arises when the CDs are periodically arranged. In an external magnetic field, applied parallel to the CDs, one or more magnetic flux quanta penetrate the CDs. The resulting magnetic commensurability (matching) fields are

$$B_m = m \frac{2\Phi_0}{\sqrt{3}a^2}, \quad (5)$$

where m is a rational number, and a denotes the lattice constant of a hexagonal CD lattice. At the matching fields B_m , when each CD can be filled on average by m flux quanta, a significant change in the vortex dynamics can be expected. The most prominent effects are observed when m is a natural number. At these matching fields, we observe the *ordered Bose glass* phase discussed below.

Tuning the magnetic field allows one to switch the vortex ensemble between VG and OBG. However, in the case of YBCO thin films with their strong intrinsic pinning by twin boundaries and screw dislocations, the VG, the BG, and the OBG are competing phases of increasingly frustrated disorder. At lower temperatures, the VG might evolve into a Bragg glass [34], where vortex dislocations are absent, and quasi-long-range translational order is preserved. Similarly, with vanishing disorder and at low temperatures, the OBG can transform into a vortex Mott insulator [11], where the vortices condense in a commensurate arrangement with the CDs. Both Bragg glass and vortex Mott insulator differ from VG, BG, and OBG as they melt through a first-order transition.

3. Materials and Methods

3.1. Sample Preparation

Thin YBCO films were epitaxially grown on $(\text{LaAlO}_3)_{0.3}(\text{Sr}_2\text{AlTaO}_6)_{0.7}$ (LSAT) substrates by pulsed laser deposition (PLD). The thickness of the film $t = (26.0 \pm 2.4)$ nm used in this study was determined via Laue oscillations at the YBCO (001) Bragg peak. X-ray diffraction confirmed the excellent c -axis orientation of the film via the rocking curve of the YBCO (005) peak with a full width at half maximum (FWHM) of 0.08° .

Electrical contacts were established by first depositing a 20 nm-thick Au film employing in situ electron beam evaporation after the PLD process. Then, both the Au and the YBCO films were partially removed using Ar ion milling to form a bridge structure and the electrical contact pads. Afterward, parts of the Au layer were removed with Lugol's iodine to open a window for irradiating the bridge. The dimensions of the YBCO microstrip are 8 μm width and 40 μm length with voltage probes separated by 20 μm . The contact pads were connected by 50 μm -thick Au wire and Ag paste to the cryostat's sample holder.

3.2. Focused Ion-Beam Irradiation

The prepatterned YBCO microbridges were introduced into the Zeiss Orion NanoFab He-ion microscope (HIM) and aligned under low ion fluence. The focused He⁺ ion beam is adjusted to an estimated average diameter of He⁺ ion trajectories within the film of 9 nm FWHM to avoid amorphization at the YBCO film's surface. An area of $36 \times 16 \mu\text{m}^2$ was irradiated with a triangular spot lattice with distances $a = (30 \pm 0.6) \text{ nm}$, using 30 keV He⁺ ions. The number of ions per spot is 10^4 , according to the dwell time of 3.2 ms and a beam current of 0.5 pA. With this number of ions, T_c can be locally suppressed, while only at higher ion fluence can an amorphization of the crystal structure be seen in high-resolution transmission electron microscopy [35]. More details about the formation of CDs by focused ion beam irradiation can be found elsewhere [27,33].

3.3. Electrical Measurements

The electrical measurements were performed in a Physical Properties Measurement System (PPMS), equipped with a 9 T superconducting solenoid and a variable temperature insert (Quantum Design). The magnetic field was oriented perpendicular to the sample surface, and a Cernox resistor [36] is used for in-field temperature control. The resistivity measurements were performed with a constant excitation current of 1 μA in both polarities to exclude thermoelectric signals. The critical current is determined from isothermal V - I measurements using a voltage criterion of 200 nV. In addition, multiple V - I curves were collected at fixed temperatures and stable magnetic fields, which were limited to 100 μV to avoid heating effects. All data were collected by computer-controlled data acquisition.

4. Results and Discussion

The temperature dependence of the resistance R of a YBCO microbridge after patterning with a hexagonal array of 30 nm spaced CDs is shown in Figure 1a, together with the $R(T)$ curve for an unirradiated microbridge, as a reference sample. The inset displays an optical microscopy picture of the YBCO bridge taken after irradiation in the HIM. The red dotted rectangle marks the irradiated area, extending over the entire bridge between the voltage probes and containing about 7.4×10^5 CDs according to the irradiation protocol. Even at much higher magnification in the HIM, we cannot identify the signatures of the CDs. Actually, ion fluence was deliberately chosen such that mainly oxygen atoms are displaced, but amorphization of the material is avoided. It is only at more than an order of magnitude higher fluence that we can visualize local destruction of the crystal structure [27,35].

The non-irradiated YBCO bridge, prepared as a reference on the same substrate, has a $T_c = 88.4 \text{ K}$ (defined as the inflection point). The T_c in very thin films is generally slightly lower than in single crystals due to the strain imposed by the substrate. Focused ion beam irradiation in the HIM causes a reduction to $T_c = 76.0 \text{ K}$. The T_c suppression is much less than previously reported for masked He⁺ ion irradiation of CDs with larger diameters and spacings [28,30]. We suspect that the scattering of individual ions away from the CDs creates a small number of point defects between the CDs, which are known to reduce T_c . The similar slopes of the pristine and nanopatterned bridges indicate that irradiation does not affect the charge carrier density in the inter-CD regions. On the other hand, the offset of a linear extrapolation of the normal state resistance at zero temperature is much higher in the irradiated sample, which is attributed to enhanced defect scattering [37,38].

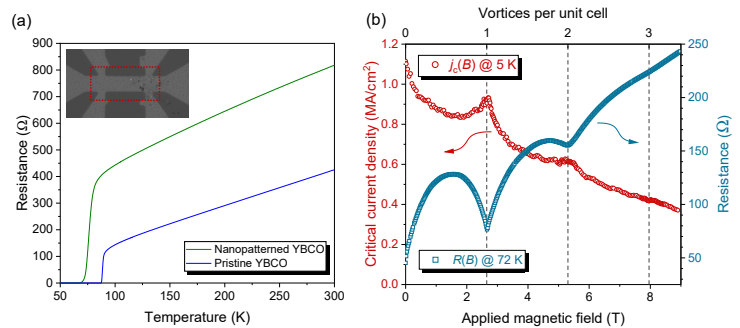


Figure 1. (a) Resistances of a YBCO thin film with a hexagonal array of 30 nm spaced columnar defects and an unirradiated reference bridge fabricated on the same substrate. Inset: Optical microscopy picture of the bridge taken after irradiation. The red dotted rectangle marks the irradiated area of $36 \times 16 \mu\text{m}^2$. (b) Critical current density at 5 K and resistance at 72 K of the irradiated bridge. The broken lines indicate the number of vortices per unit cell of the hexagonal CD lattice, corresponding to the matching fields $B_m = m \times 2.653$ T, which were calculated from Equation (5) using the nominal geometry of the irradiation pattern.

Figure 1b presents the pronounced vortex commensurability effects in j_c at 5 K and R at 72 K of the nanopatterned YBCO bridge as a function of the magnetic field applied orthogonal to the sample surface. The critical current density serves as a static probe, and a well-developed peak is centered around the matching field $B_1 = 2.653$ T. It perfectly agrees with B_1 calculated from Equation (5) inserting the $a = 30$ nm of the irradiation protocol in the HIM. The noticeable dip in the flux-flow resistance indicates that commensurability is not lost in approaching the vortex liquid regime and might indicate a plastic-flow phase [39]. It was established previously by the angular dependence of B_m in tilted magnetic fields [29,33] that the CDs indeed act as one-dimensional pinning lines in such systems. In addition, a less prominent peak of the critical current density and a corresponding dip in the resistance is present at $B_2 = 5.31$ T, i.e., with an arrangement of two vortices per unit cell of the CD lattice. These observations justify studying V - I curves further to explore the critical scaling mentioned earlier.

The V - I characteristics were recorded in static magnetic fields ranging from 1.0 to 8.0 T and with temperatures in the vicinity of the glass temperature as the variable parameter. For example, the isotherms for the matching field $B_1 = 2.653$ T are presented in Figure 2a. At 66 K (red lines) and above (not shown), an ohmic behavior is observed in the low-current limit and attributed to TAFF. At lower temperatures, non-linearity emerges, and a power-law behavior can be observed over the entire current range. The V - I characteristics at $T < T_g$ (to the right of the green line) have negative curvatures that hint at a vanishing resistance for a particular critical current. All these observations match the predictions of both the VG and BG theories and Equation (1).

Following the scaling theories, Figure 2b shows the collapse of the V/I vs. I data deduced from panel (a) according to Equation (2). Two branches, corresponding to the universal functions \mathfrak{F}_+ and \mathfrak{F}_- are built up from the various isotherms. The results appear qualitatively similar to previous works, except for the dynamic parameter $z_{VG} = 9.0$ that falls outside the reasonable range predicted by the VG theory and also differs from previous experimental findings.

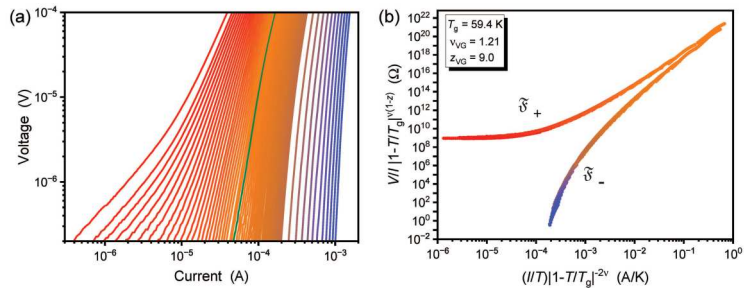


Figure 2. (a) V - I isotherms at 66 K (red), 65.5 to 52 K in 0.25 K steps, and 50 to 30 K (blue) in 2 K steps of the nanopatterned sample at the matching field $B_1 = 2.653$ T. The green line indicates the isotherm at 59.5 K, which is closest to the glass temperature $T_g = 59.4$ K. (b) V/I vs. I isotherms plotted according to the VG scaling of Equation (2). The isotherms collapse onto the two universal functions $\tilde{\gamma}_+$ above and $\tilde{\gamma}_-$ below T_g , respectively. The colors of the data points represent the temperature and are the same as in panel (a).

Figure 3a illustrates the systematic change of the glass temperature T_g with the applied magnetic field. Pristine YBCO shows an almost linear decrease of T_g with the magnetic field [12]. This trend, indicated by the dotted line, can also be observed in the nanopatterned sample, as long as the applied magnetic field is not commensurate. However, at B_1 and, to a lesser extent, B_2 , peaks of T_g are visible.

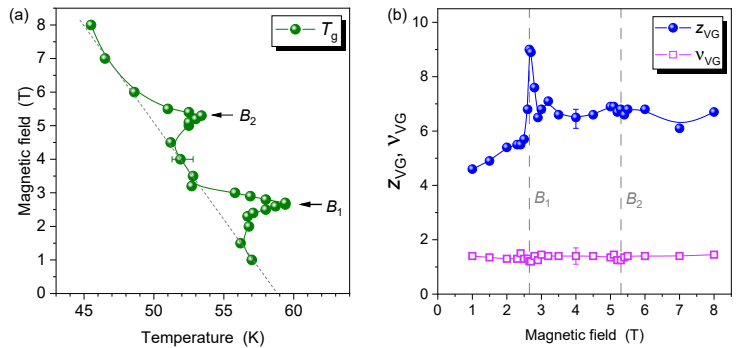


Figure 3. Scaling parameters of the nanopatterned YBCO film. The representative error bars indicate the uncertainty caused by interdependence between the fit parameters T_g , z_{VG} , and ν_{VG} . The size of the symbols represents the uncertainty of the parameter when the other two parameters are kept fixed. Solid lines are guides to the eye. (a) The phase boundary between the vortex liquid and the glass phase is represented by the glass temperature T_g as a function of the external magnetic field. The gray dotted line symbolizes a linear trend of T_g . (b) Parameters from the scaling analyses according to Equation (2).

The scaling parameters ν_{VG} and z_{VG} in different magnetic fields behave very diverse, as demonstrated in Figure 3b. On the one hand, the parameter ν_{VG} is independent of the magnetic field and has the typical value $\nu_{VG} = 1.3 \pm 0.2$, which is also reported for pristine YBCO [19]. On the other hand, $z_{VG} = 6.5 \pm 0.5$ at 3 T $< B < 8$ T but exhibits a narrow peak at B_1 with a maximum $z_{VG} = 9.0$. This value of z_{VG} lies clearly outside the 3-dimensional (3D) VG scaling range. Interestingly, z_{VG} does not peak at B_2 , and the minor broad hump

is within error limits. We can imagine two possible reasons: either the pinning force of the second vortex in a CD is rather small so that it can easily escape, or the second vortex is already magnetically caged at an interstitial position. In both scenarios, the dynamics of moving vortices will be dominated by the disordered defects that are present between the CDs and result in a similar z_{VG} as in off-matching fields.

In Figure 3, we have introduced two different error estimates. The size of the symbols indicates the respective uncertainty of T_g , ν_{VG} , and z_{VG} when the other two parameters are kept fixed. There is, however, interdependence between the choice of parameters, mainly between T_g and z_{VG} . An increase of T_g relates to a decrease of z_{VG} , and vice versa. The range in which reasonable scaling collapses can be achieved is marked by error bars. It is crucial that the significant matching effect at B_1 is represented by an increase of *both* T_g and z_{VG} . Hence, despite any uncertainties with the collapsing V/I vs. I curves, a marked change in the vortex dynamics is evident.

When converting the critical exponents to those of the BG theory by Equation (4), we find $\nu_{BG} = 0.81$ and $z_{BG} = 14$ at B_1 . Note that both theories predict comparable values for ν , and, as discussed above, we do not observe any features of ν_{VG} at the matching fields in the nanopatterned sample. Conversely, the value for $z_{BG} = 14$ is significantly above previous results ($z_{BG} \sim 9$) in YBCO with incommensurate BaZrO₃ (BZO) nanorods [23]. We attribute this enhancement of z_{BG} to the periodic arrangement of the CDs in our samples and thus to the OBG phase. A theoretical analysis reported [34] that in the quasi-long-range ordered Bragg glass, the $V-I$ isotherms are steeper than in the VG. According to Equation (3), steeper isotherms are connected with a larger z , which also points to an increase of z by the frustration of disorder and is in accordance with our observations.

In Figure 4, the collapsed curves at the commensurability field B_1 and an off-matching field of 4 T are compared. The dotted lines indicate the bifurcation between the universal functions \mathfrak{F}_{\pm} . Remarkably, these bifurcation lines have significantly different slopes, which are, according to Equation (3), determined solely by the dynamic scaling parameter z_{VG} (or z_{BG}). Thus, steeper V/I vs. I isotherms at B_1 and, at the same time, z_{BG} above the typical values for a *disordered Bose glass* strongly support our proposal of an *ordered Bose glass* phase.

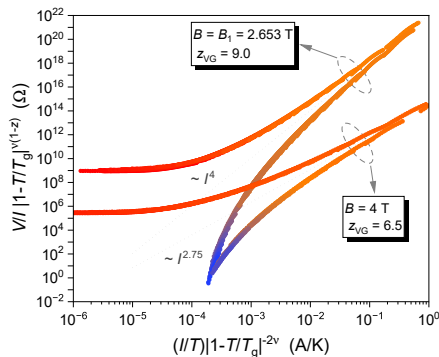


Figure 4. Comparison of the collapsed V/I vs. I curves at the first matching field $B_1 = 2.653$ T and at an off-matching field $B = 4$ T. The dotted lines indicate the bifurcation and have different exponents. Color coding is the same as in Figure 2.

One might raise concerns about a ‘true’ 3D nature of vortices in very thin films rendering 2D scaling theories more appropriate [14]. Taking the distance of vortices $l \simeq \sqrt{\Phi_0/B}$, a 3D vortex glass is expected when $l \lesssim t$. For our film with $t = 26$ nm, the condition for 3D is fulfilled for $B \gtrsim B_1$.

As a cross-check, we can evaluate the critical parameters for 2D scaling. It follows from Equation (2) that $v_{VG}^{2D} = 2v_{VG}^{3D}$ and $z_{VG}^{2D} = (z_{VG}^{3D} - 1)/2$. Thus, the same collapse of the V - I isotherms can be achieved with the adapted parameters of the 2D model. However, $v_{VG}^{2D} = 2.6 \pm 0.4$ would be outside the expected range between 1 and 2, and, moreover, $z_{VG}^{2D} = 2.75 \pm 0.25$ at $3\text{ T} < B < 8\text{ T}$ is too low for a VG. Only at B_1 , $z_{VG}^{2D} = 4.0$ would be an acceptable value. A typical 2D vortex ensemble is weakly coupled pancake vortices. Assuming that such a 2D situation arises by introducing columnar pinning defects would be counterintuitive. We thus conclude that a 2D glass scaling theory is incompatible with our observations.

Our results can be compared with previous findings. In pristine YBCO thin films at a magnetic field $B = 2\text{ T}$, 3D scalings with $v_{VG} = 1.7$, $z_{VG} = 4.9$ [12] and $v_{VG} = 1.3 \pm 0.1$, $z_{VG} = 4.8 \pm 0.3$ [19], respectively, have been reported. These values correspond well to our present results for $B < B_1$. Theoretically, the two critical parameters are expected to be independent of the applied magnetic field. However, at $B > B_1$, we observe an increase to $z_{VG} \simeq 6.5$, which is slightly above the typical bandwidth for VG scaling.

A possible reason is that a fraction B_1/B of vortices are bound in the CDs, whereas additional flux penetrates as interstitial vortices. Such a landscape of correlated quenched disorder by the CDs and various disordered pinning sites (twin boundaries and screw dislocations) between them could lead to more complex vortex dynamics and thus to z_{VG} values between those at low fields and the high one observed at B_1 .

Similar considerations lead to the difference between a vortex Mott insulator and the present situation of an OBG. A vortex Mott insulator should show no glassy behavior since vortex lines can equidistantly hop from one CD to the next [40]. In an OBG, however, the disordered intrinsic defects between the CDs can also trap vortices and induce glassiness.

In YBCO thin films that were large-area irradiated (i.e., without lateral modulation of the fluence) with 80 keV He^+ ions, $v_{VG} = 1.4$, $z_{VG} = 4.75$ have been reported, and no difference was found between irradiated and pristine films [37]. Hence, we conclude that it must be the defect pattern created by focused He^+ ion beam irradiation in our sample that leads to the present observations.

Remarkably, a study of thin YBCO films after irradiation with 100 keV O^+ ions through a masking layer penetrated by a square lattice of holes with 120 nm spacings found 2D scaling of the V - I isotherms, indicating reduced vortex-glass correlations along the vortex line [29]. In addition, no significant change of the critical exponents v_{VG} and z_{VG} has been found at the matching field, yet there is a slight enhancement of the vortex glass temperature. Although there are several differences in our study, such as hexagonal versus square CD patterns and the different nature and diameters of the CDs, we believe that the main reason is the CD's density. The condition $l \lesssim t$ discussed above is not met, which might indeed lead to a 2D-VG behavior.

5. Conclusions

Thin films of the copper-oxide superconductor YBCO contain many intrinsic defects, such as point defects, twinning phase boundaries, and screw dislocations, that act as randomly distributed pinning sites. An ultradense hexagonal arrangement of columnar defects created by focused He^+ ion irradiation can overcome the uncorrelated pinning in YBCO thin films. We have found that in such a sample, the vortex dynamics and the relative strength of periodic and uncorrelated pinning sites can be tuned by the applied magnetic field. Furthermore, critical scaling relations of the voltage-current isotherms in constant magnetic fields yield parameters that distinguish between vortex glass and an *ordered Bose glass* behavior. The latter can emerge from a vortex Mott insulator when thermal energy and disorder weaken the vortex correlations, as is the case in our experiments. Accordingly, we observe the *ordered Bose glass* phase exactly at the matching field, where every columnar defect can be filled by one flux quantum.

Still, many intriguing issues exist in the vortex physics of copper-oxide superconductors. The fabrication of engineered pinning landscapes in copper-oxide superconductors

with controlled geometry and tens of nm spacings may raise the investigations of vortex systems and their various phases originating from the competition of pinning and elastic vortex forces, disorder, and fluctuations to a higher level.

Author Contributions: W.L., D.K., R.K. and E.G. conceived and supervised the experiments, K.W. grew the film, M.K. patterned the film and performed the focused ion beam irradiation, L.B., B.A. and W.L. performed the transport measurements, L.B. and W.L. analyzed the data, all authors discussed the results and contributed to writing the paper. All authors have read and agreed to the published version of the manuscript.

Funding: Open Access Funding by the Austrian Science Fund (FWF). The research was funded by a joint project of the Austrian Science Fund (FWF), grant I4865-N, and the German Research Foundation (DFG), grant KO 1303/16-1, and it is based upon work from COST Actions CA16218 (NANOCOXY-BRI), CA19108 (Hi-SCALE), and CA19140 (FIT4NANO), supported by COST (European Cooperation in Science and Technology).

Data Availability Statement: The data presented in this study are available on reasonable request from the corresponding author.

Conflicts of Interest: The authors declare no conflict of interest.

References

1. Blatter, G.; Feigel'man, M.V.; Geshkenbein, V.B.; Larkin, A.I.; Vinokur, V.M. Vortices in high-temperature superconductors. *Rev. Mod. Phys.* **1994**, *66*, 1125–1388. [[CrossRef](#)]
2. Wördenweber, R.; Moshchalkov, V.; Bending, S.; Tafuri, F. (Eds.) *Superconductors at the Nanoscale: From Basic Research to Applications*; de Gruyter: Berlin, Germany, 2017. [[CrossRef](#)]
3. Vallès, F.; Palau, A.; Abrahimov, D.; Jaroszynski, J.; Constantinescu, A.M.; Mundet, B.; Obradors, X.; Larbalesstier, D.; Puig, T. Optimizing vortex pinning in $\text{YBa}_2\text{Cu}_3\text{O}_{7-x}$ superconducting films up to high magnetic fields. *Commun. Mater.* **2022**, *3*, 45. [[CrossRef](#)]
4. Anderson, P.W. Theory of Flux Creep in Hard Superconductors. *Phys. Rev. Lett.* **1962**, *9*, 309–311. [[CrossRef](#)]
5. Kim, Y.B.; Hempstead, C.F.; Strnad, A.R. Critical Persistent Currents in Hard Superconductors. *Phys. Rev. Lett.* **1962**, *9*, 306–309. [[CrossRef](#)]
6. Kes, P.H.; Aarts, J.; van den Berg, J.; van der Beek, J.C.; Mydosh, J.A. Thermally Assisted Flux Flow at Small Driving Forces. *Supercond. Sci. Technol.* **1989**, *1*, 242–248. [[CrossRef](#)]
7. Reichhardt, C.; Olson Reichhardt, C.J. Depinning and nonequilibrium dynamic phases of particle assemblies driven over random and ordered substrates: A review. *Rep. Prog. Phys.* **2017**, *80*, 026501. [[CrossRef](#)]
8. Fisher, M. Vortex Glass Superconductivity: A Possible New Phase in Bulk High- T_c Oxides. *Phys. Rev. Lett.* **1989**, *62*, 1415. [[CrossRef](#)] [[PubMed](#)]
9. Fisher, D.S.; Fisher, M.P.A.; Huse, D.A. Thermal Fluctuations, Quenched Disorder, Phase Transitions, and Transport in Type-II Superconductors. *Phys. Rev.* **1991**, *43*, 130–159. [[CrossRef](#)] [[PubMed](#)]
10. Nelson, D.R.; Vinokur, V.M. Boson Localization and Pinning by Correlated Disorder in High-Temperature Superconductors. *Phys. Rev. Lett.* **1992**, *68*, 2398–2401. [[CrossRef](#)]
11. Nelson, D.R.; Vinokur, V.M. Boson Localization and Correlated Pinning of Superconducting Vortex Arrays. *Phys. Rev. B* **1993**, *48*, 13060–13097. [[CrossRef](#)]
12. Koch, R.; Foglietti, V.; Gallagher, W.; Koren, G.; Gupta, A.; Fisher, M. Experimental Evidence for Vortex-Glass Superconductivity in Y-Ba-Cu-O. *Phys. Rev. Lett.* **1989**, *63*, 1511. [[CrossRef](#)] [[PubMed](#)]
13. Hou, L.F.; Deak, J.; Metcalf, P.; Mcelfresh, M. Effect of Oxygen Stoichiometry on the Vortex-Glass Phase Transition in $\text{YBa}_2\text{Cu}_3\text{O}_{7-\delta}$ Thin Films. *Phys. Rev. B* **1994**, *50*, 7226–7229. [[CrossRef](#)] [[PubMed](#)]
14. Dekker, C.; Wöltgens, P.J.M.; Koch, R.H.; Hussey, B.W.; Gupta, A. Absence of a finite-temperature vortex-glass phase transition in two-dimensional $\text{YBa}_2\text{Cu}_3\text{O}_{7-\delta}$ films. *Phys. Rev. Lett.* **1992**, *69*, 2717–2720. [[CrossRef](#)] [[PubMed](#)]
15. Gammel, P.L.; Schneemeyer, L.F.; Bishop, D.J. SQUID Picovoltometry of $\text{YBa}_2\text{Cu}_3\text{O}_7$ Single Crystals: Evidence for a Finite-Temperature Phase Transition in the High-Field Vortex State. *Phys. Rev. Lett.* **1991**, *66*, 953–956. [[CrossRef](#)]
16. Safar, H.; Gammel, P.L.; Bishop, D.J.; Mitzi, D.B.; Kapitulnik, A. SQUID Picovoltometry of Single Crystal $\text{Bi}_2\text{Sr}_2\text{CaCu}_2\text{O}_{8+\delta}$: Observation of the Crossover from High-Temperature Arrhenius to Low-Temperature Vortex-Glass Behavior. *Phys. Rev. Lett.* **1992**, *68*, 2672–2675. [[CrossRef](#)]
17. Yamasaki, H.; Endo, K.; Kosaka, S.; Umeda, M.; Yoshida, S.; Kajimura, K. Quasi-two-dimensional vortex-glass transition observed in epitaxial $\text{Bi}_2\text{Sr}_2\text{CaCu}_2\text{O}_x$ thin films. *Phys. Rev. B* **1994**, *50*, 12959–12965. [[CrossRef](#)]
18. Sefrioui, Z.; Arias, D.; Varela, M.; Villegas, J.E.; de la Torre, M.A.L.; León, C.; Loos, G.D.; Santamaría, J. Crossover from a three-dimensional to purely two-dimensional vortex-glass transition in deoxygenated $\text{YBa}_2\text{Cu}_3\text{O}_{7-\delta}$ thin films. *Phys. Rev. B* **1999**, *60*, 15423–15429. [[CrossRef](#)]

19. Lang, W.; Fussenegger, C.; Proyer, S.; Stangl, E.; Bäuerle, D. Observation of the vortex-glass transition in $\text{YBa}_2\text{Cu}_3\text{O}_7$ by phase-resolved current-voltage measurements. *Z. Phys. B* **1996**, *100*, 13–18. [[CrossRef](#)]
20. Krusin-Elbaum, L.; Civale, L.; Blatter, G.; Marwick, A.D.; Holtzberg, F.; Feild, C. Bose-glass melting in YBaCuO crystals with correlated disorder. *Phys. Rev. Lett.* **1994**, *72*, 1914–1917. [[CrossRef](#)]
21. Wöltgens, P.J.M.; Dekker, C.; Swüste, J.; de Wijn, H.W. Superconducting Phase of $\text{YBa}_2\text{Cu}_3\text{O}_{7-\delta}$ Films in High Magnetic Fields: Vortex Glass or Bose Glass. *Phys. Rev. B* **1993**, *48*, 16826–16829. [[CrossRef](#)]
22. Safar, H.; Foltyn, S.R.; Jia, Q.X.; Maley, M.P. Bose glass vortex phase transition in twinned $\text{YBa}_2\text{Cu}_3\text{O}_{7-\delta}$ superconductors. *Philos. Mag. B* **1996**, *74*, 647–654. [[CrossRef](#)]
23. Horide, T.; Matsumoto, K.; Mele, P.; Ichinose, A.; Kita, R.; Mukaida, M.; Yoshida, Y.; Horii, S. The crossover from the vortex glass to the Bose glass in nanostructured $\text{YBa}_2\text{Cu}_3\text{O}_{7-x}$ films. *Appl. Phys. Lett.* **2008**, *92*, 182511. [[CrossRef](#)]
24. Lang, W.; Dineva, M.; Marksteiner, M.; Enzenhofer, T.; Siraj, K.; Peruzzi, M.; Pedarnig, J.D.; Bäuerle, D.; Korntner, R.; Cekan, E.; et al. Ion-beam direct-structuring of high-temperature superconductors. *Microelectron. Eng.* **2006**, *83*, 1495–1498. [[CrossRef](#)]
25. Lang, W.; Richter, H.; Marksteiner, M.; Siraj, K.; Bodea, M.A.; Pedarnig, J.D.; Grigoropoulos, C.; Bäuerle, D.; Hasenfuss, C.; Palmethofer, L.; et al. Masked ion beam irradiation of high-temperature superconductors: Patterning of nano-size regions with high point-defect density. *Int. J. Nanotechnol.* **2009**, *6*, 704–714. [[CrossRef](#)]
26. Pedarnig, J.D.; Siraj, K.; Bodea, M.A.; Puica, I.; Lang, W.; Kolarova, R.; Bauer, P.; Haselgrübler, K.; Hasenfuss, C.; Beinik, I.; et al. Surface planarization and masked ion-beam structuring of $\text{YBa}_2\text{Cu}_3\text{O}_7$ thin films. *Thin Solid Film.* **2010**, *518*, 7075–7080. [[CrossRef](#)]
27. Aichner, B.; Müller, B.; Karrer, M.; Misko, V.R.; Limberger, F.; Mletschnig, K.L.; Dosmailov, M.; Pedarnig, J.D.; Nori, F.; Kleiner, R.; et al. Ultradense Tailored Vortex Pinning Arrays in Superconducting $\text{YBa}_2\text{Cu}_3\text{O}_{7-\delta}$ Thin Films Created by Focused He Ion Beam Irradiation for Fluxonics Applications. *ACS Appl. Nano Mater.* **2019**, *2*, 5108–5115. [[CrossRef](#)]
28. Swiecicki, I.; Ulysse, C.; Wolf, T.; Bernard, R.; Bergeal, N.; Briatico, J.; Faini, G.; Lesueur, J.; Villegas, J.E. Strong field-matching effects in superconducting $\text{YBa}_2\text{Cu}_3\text{O}_{7-\delta}$ films with vortex energy landscapes engineered via masked ion irradiation. *Phys. Rev. B* **2012**, *85*, 224502. [[CrossRef](#)]
29. Trastoy, J.; Rouco, V.; Ulysse, C.; Bernard, R.; Palau, A.; Puig, T.; Faini, G.; Lesueur, J.; Briatico, J.; Villegas, J.E. Unusual magneto-transport of $\text{YBa}_2\text{Cu}_3\text{O}_{7-\delta}$ films due to the interplay of anisotropy, random disorder and nanoscale periodic pinning. *New J. Phys.* **2013**, *15*, 103022. [[CrossRef](#)]
30. Haag, L.T.; Zechner, G.; Lang, W.; Dosmailov, M.; Bodea, M.A.; Pedarnig, J.D. Strong vortex matching effects in YBCO films with periodic modulations of the superconducting order parameter fabricated by masked ion irradiation. *Physica C* **2014**, *503*, 75–81. [[CrossRef](#)]
31. Trastoy, J.; Malnou, M.; Ulysse, C.; Bernard, R.; Bergeal, N.; Faini, G.; Lesueur, J.; Briatico, J.; Villegas, J.E. Freezing and thawing of artificial ice by thermal switching of geometric frustration in magnetic flux lattices. *Nat. Nanotechnol.* **2014**, *9*, 710–715. [[CrossRef](#)]
32. Zechner, G.; Lang, W.; Dosmailov, M.; Bodea, M.A.; Pedarnig, J.D. Transverse vortex commensurability effect and sign change of the Hall voltage in superconducting $\text{YBa}_2\text{Cu}_3\text{O}_{7-\delta}$ thin films with a nanoscale periodic pinning landscape. *Phys. Rev. B* **2018**, *98*, 104508. [[CrossRef](#)]
33. Aichner, B.; Mletschnig, K.L.; Müller, B.; Karrer, M.; Dosmailov, M.; Pedarnig, J.D.; Kleiner, R.; Koelle, D.; Lang, W. Angular magnetic-field dependence of vortex matching in pinning lattices fabricated by focused or masked helium ion beam irradiation of superconducting $\text{YBa}_2\text{Cu}_3\text{O}_{7-\delta}$ thin films. *Low Temp. Phys.* **2020**, *46*, 331–337. [[CrossRef](#)]
34. Giamarchi, T.; Le Doussal, P. Phase diagrams of flux lattices with disorder. *Phys. Rev. B* **1997**, *55*, 6577–6583. [[CrossRef](#)]
35. Müller, B.; Karrer, M.; Limberger, F.; Becker, M.; Schröppel, B.; Burkhardt, C.J.; Kleiner, R.; Goldobin, E.; Koelle, D. Josephson Junctions and SQUIDS Created by Focused Helium-Ion-Beam Irradiation of $\text{YBa}_2\text{Cu}_3\text{O}_7$. *Phys. Rev. Appl.* **2019**, *11*, 044082. [[CrossRef](#)]
36. Heine, G.; Lang, W. Magnetoresistance of the new ceramic ‘Cernox’ thermometer from 4.2 K to 300 K in magnetic fields up to 13 T. *Cryogenics* **1998**, *38*, 377–379. [[CrossRef](#)]
37. Sefrioui, Z.; Arias, D.; González, E.M.; León, C.; Santamaría, J.; Vicent, J.L. Vortex liquid entanglement in irradiated $\text{YBa}_2\text{Cu}_3\text{O}_{7-\delta}$ thin films. *Phys. Rev. B* **2001**, *63*, 064503. [[CrossRef](#)]
38. Lang, W.; Pedarnig, J.D. Ion Irradiation of High-Temperature Superconductors and Its Application for Nanopatterning. In *Nanoscience and Engineering in Superconductivity*; Moshchalkov, V.V., Wördenweber, R., Lang, W., Eds.; Springer: Berlin/Heidelberg, Germany, 2010; pp. 81–104. [[CrossRef](#)]
39. Reichhardt, C.; Olson, C.J.; Nori, F. Dynamic phases of vortices in superconductors with periodic pinning. *Phys. Rev. Lett.* **1997**, *78*, 2648–2651. [[CrossRef](#)]
40. Sørensen, M.P.; Pedersen, N.F.; Ögren, M. The dynamics of magnetic vortices in type II superconductors with pinning sites studied by the time dependent Ginzburg–Landau model. *Physica C* **2017**, *533*, 40–43. [[CrossRef](#)]

Publication 6

Reprinted with permission from
M. Karrer et al., *Physical Review Applied* **22**, 014043 (2024)
available under the terms of the Creative Commons Attribution
4.0 International license.

Vortex matching at 6 T in $\text{YBa}_2\text{Cu}_3\text{O}_{7-\delta}$ thin films by imprinting a 20-nm periodic pinning array with a focused helium-ion beam

Max Karrer¹, Bernd Aichner², Katja Wurster¹, César Magén³, Christoph Schmid¹, Robin Hutt¹, Barbora Budinská^{2,4}, Oleksandr V. Dobrovolskiy⁵, Reinhold Kleiner¹, Wolfgang Lang^{2,*}, Edward Goldobin³, and Dieter Koelle^{1,†}


¹Physikalisches Institut, Center for Quantum Science (CQ) and LISA⁺, University of Tübingen, Auf der Morgenstelle 14, 72076 Tübingen, Germany

²Faculty of Physics, University of Vienna, Boltzmanngasse 5, 1090 Vienna, Austria

³Instituto de Nanociencia y Materiales de Aragón (INMA), CSIC-Universidad de Zaragoza, 50009 Zaragoza, Spain

⁴Vienna Doctoral School in Physics, University of Vienna, Boltzmanngasse 5, 1090 Vienna, Austria

⁵Cryogenic Quantum Electronics, Institut für Elektrische Messtechnik und Grundlagen der Elektrotechnik, Technische Universität Braunschweig, Hans-Sommer-Str. 66, 38106 Braunschweig, Germany and Laboratory for Emerging Nanometrology, Technische Universität Braunschweig, Langer Kamp 6a/b, 38106 Braunschweig, Germany

 (Received 8 April 2024; accepted 25 June 2024; published 17 July 2024)

Controlled engineering of vortex pinning sites in copper-oxide superconductors is a critical issue in manufacturing devices based on magnetic flux quanta. To address this, we employed a focused He-ion beam (He-FIB) to irradiate thin $\text{YBa}_2\text{Cu}_3\text{O}_{7-\delta}$ films and create ultradense hexagonal arrays of defects with lattice spacings as small as 20 nm. Critical current and magnetoresistance measurements demonstrate efficient pinning by a matching field of 6 T visible in a huge temperature range from the critical temperature T_c down to 2 K. These results show that He-FIB irradiation provides excellent opportunities for the development and application of superconducting fluxonic devices based on Abrikosov vortices. In particular, our findings suggest that such devices can operate at temperatures far below T_c , where superconductivity is robust.

DOI: [10.1103/PhysRevApplied.22.014043](https://doi.org/10.1103/PhysRevApplied.22.014043)

I. INTRODUCTION

Superconductivity is a macroscopic quantum phenomenon characterized by the long-range coherence of charge carriers that make up the superconducting condensate. Most technically viable superconductors, including copper-oxide superconductors (HTS) with high critical temperature T_c , belong to the class of type-II superconductors. These materials allow the magnetic field to penetrate in the form of Abrikosov vortices of supercurrent, which carry the quantized magnetic flux $\Phi_0 = h/(2e)$, where h is Planck's constant and e is the elementary charge.

The properties and the interaction of Abrikosov vortices are controlled by two characteristic lengths: the Ginzburg-Landau coherence length ξ and the London penetration depth λ [1]. In the vortex center, the superconducting order parameter is suppressed to zero on the length scale ξ , thus creating a normal-conducting vortex core of approximately 2ξ diameter. As the formation of this normal-conducting core (i.e., the suppression of superconductivity) requires energy, the vortex will be preferentially pinned to a non-superconducting defect.

The magnetic field and the supercurrents circulating around the vortex core decay exponentially on a characteristic scale given by the London penetration depth $\lambda > \xi$, which determines the magnetic vortex-vortex interaction range. For thin superconducting films with thickness $t_z \lesssim \lambda$, the so-called Pearl length [2] $\Lambda = 2\lambda^2/t_z$ replaces λ .

Importantly, Ginzburg-Landau theory predicts the temperature dependence $\xi(T) = \xi(0)(1 - T/T_c)^{-1/2}$, which implies that $\xi(T) \rightarrow \infty$ at temperature $T \rightarrow T_c$. The same temperature dependence is predicted for $\lambda(T)$ [1]. Consequently, at temperatures near T_c , the size of the

*Contact author: wolfgang.lang@univie.ac.at

†Contact author: koelle@uni-tuebingen.de

Published by the American Physical Society under the terms of the [Creative Commons Attribution 4.0 International license](https://creativecommons.org/licenses/by/4.0/). Further distribution of this work must maintain attribution to the author(s) and the published article's title, journal citation, and DOI.

vortex cores and their interaction range rises significantly. For the anisotropic compound $\text{YBa}_2\text{Cu}_3\text{O}_{7-s}$ (YBCO) used here as a prototypical HTS, the in-plane parameters are $\xi_{ab}(0) \approx 1.2$ nm and $\lambda_{ab}(0) \approx 250$ nm (for epitaxial thin films) [3–5].

A single Abrikosov vortex can store a classical data bit [6] and can be manipulated by several methods [7]. Vortices and interacting vortex ensembles have been suggested to build superconducting devices like vortex ratchets [8], cellular automata [9,10], superconducting diodes, vortex-based memory cells [11], and artificial vortex ice [12]. Although some of these concepts have been realized in experiments [13–15], it has not yet been possible to exploit the fundamentally possible degree of complexity and miniaturization. Hence, previous experiments with artificial vortex pinning sites were restricted by the employed etching techniques and had to be operated at temperatures $T \rightarrow T_c$ where the interaction length $\Lambda(T)$ is longer than the spacing a between the pins [16–18]. Innovative concepts, such as growing Nb films on nanopore templates [19], have been employed to mitigate these issues.

However, one aims to create devices that work at temperatures below about $T_c/2$ where superconductivity is robust and thermodynamic fluctuations do not reduce the collective vortex effects. Accordingly, the goal is to design and fabricate arrangements of many pinning sites in YBCO with diameters $d \gtrsim 2\xi_{ab}(T_c/2)$ and spacings a such that $d < a \ll \Lambda(T_c/2)$.

Thin films of YBCO are usually patterned by etching away material, which leads to a landscape with varying thickness. This process is extremely delicate and becomes even more challenging for nanoscale patterning due to the potential loss of oxygen through the open side faces of the remaining material. However, the loss of oxygen ultimately results in the degradation of the superconducting properties.

To overcome this issue, a masked light-ion beam from an implanter has been employed to fabricate regions with suppressed superconductivity [20–28]. The impacting ions create mainly Frenkel defects of the oxygen atoms in the YBCO crystal [29], while maintaining the crystallographic framework and the surface of the film intact. The binding energies are typically in the range of 1–3 eV [30,31] for O atoms in the CuO chains and about 8 eV [31] for the O atoms in the CuO_2 planes of YBCO. Point defects caused by ion impact break the superconducting carrier pairs and suppress T_c . These defects also scatter charge carriers and increase the normal-state resistivity. He^+ ions with moderate energy are ideal [32] for creating enough point defects to completely suppress superconductivity at a practically available fluence of $\phi < 10^{16}$ ions/cm² while still penetrating a YBCO film with a thickness less than about 100 nm [33]. However, columns of nonsuperconducting material of diameters [15] d and spacings [34] a

achieved by masked ion irradiation of YBCO are presently limited to $d \sim 70$ nm and $a \sim 100$ nm.

In this work, we utilize the focused He-ion beam (He-FIB) of a helium ion microscope (HIM) to achieve a spatial resolution well below 70 nm. We exemplify the advantages of the HIM’s unique properties [35] by showcasing vortex-matching effects in a set of hexagonal pinning arrays. The matching effects show up in measurements of the critical current I_c and resistance R versus magnetic field B , and they are remarkably robust, extending to B as high as 6 T, and persisting at T from T_c down to 2 K. Our results represent a significant advancement in the fabrication of vortex pinning landscapes in thin YBCO films.

II. EXPERIMENTAL METHODS

A. Sample fabrication

For the studies presented here, thin YBCO films were grown epitaxially on (100)-oriented single crystal $(\text{LaAlO}_3)_{0.3}(\text{Sr}_2\text{AlTaO}_6)_{0.7}$ (LSAT) substrates by pulsed laser deposition. A 20-nm-thick Au film was deposited *in situ* by electron beam evaporation right after YBCO film growth, which serves for electrical contacting. The film thicknesses (see Table I) are small enough to permit complete penetration of the He-FIB. This guarantees a low level of angular and energy dispersion in the columnar defect (CD) array, a necessary condition for observing matching effects [36]. An excellent c -axis orientation of the films is confirmed by X-ray diffraction. Figure 1(a) shows a θ - 2θ scan of the 37-nm-thick YBCO film, and the inset shows the rocking curve (ω scan) of the YBCO (005) peak with a full width at half maximum (FWHM) of 0.08°.

To fabricate microbridges on each chip, we used a combination of photolithography and Ar ion milling to pattern the Au/YBCO bilayer. Subsequently, the Au layer was removed with Lugol’s iodine from the YBCO bridge structures to be exposed to He-FIB irradiation. The superconducting properties of the YBCO films did not change after patterning into microbridges. An optical image of a microbridge with an illustration of the electrical connections is shown in Fig. 1(b). The dimensions of different bridges are chosen to maintain the same number of irradiated dots for various pinning site spacings and to minimize the irradiation time for the denser lattices (see Table I).

B. He-FIB irradiation

The He-FIB irradiation was performed in a HIM (Zeiss Orion NanoFab) at the University of Tübingen. The sample chips were attached to aluminum sample stubs and grounded with silver paste. After mounting in the HIM, they were thermally acclimated for roughly 60 min before the irradiation procedure began. For simplicity, we will refer to the number of ions hitting a certain spot on the surface of the sample as the “dose” D , which will be

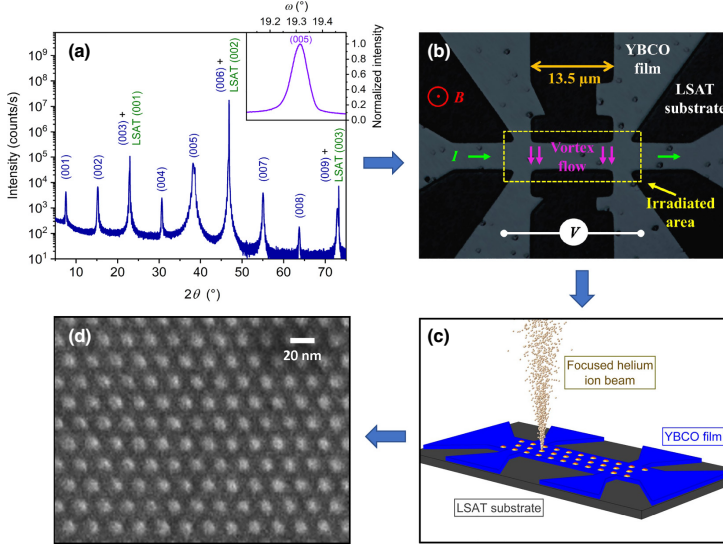


FIG. 1. Fabrication of nanopatterns by He-FIB, (a) X-ray diffraction θ - 2θ scan of the YBCO film before patterning (to create bridge H20); inset shows an ω scan of the (005) peak. (b) Optical micrograph of the bridge H20 with electrical connections after He-FIB irradiation within the area depicted by the yellow rectangle. (c) Sketch of the He-FIB patterning process. (d) Secondary electron helium ion microscope (HIM) image of a reference sample with a hexagonal $a = 20$ nm array after irradiation with an excessive dose $D = 60$ ki/dot. The white spots are blister-forming amorphous regions.

given in units of 1000 ions per dot (ki/dot). In Fig. 1(c), the fabrication of a hexagonal array of CDs by He-FIB is illustrated.

Notably, the dose $D = 10$ ki/dot was carefully selected to induce point defects and locally suppress T_c in the YBCO film, while avoiding amorphization within the CDs. To achieve this, the dose must not exceed a critical amorphization dose $D_c \approx 13$ ki/dot (see Sec. IV A 1). However, if $D < D_c$, the areas subjected to irradiation do not exhibit any visible surface degradation and cannot be seen by HIM imaging. To monitor the CD array fabrication process and visualize it, an auxiliary sample [shown in Fig. 1(d)] was

irradiated with a dose $D \gg D_c$. The scanning transmission electron microscopy (STEM) study presented in Sec. IV A 1 reveals that, for He-FIB doses above the amorphization threshold, the amorphous region causes local swelling, resulting in a bulge of the surface, as shown in Fig. 1(d).

Apart from the number of impinging ions, the lateral intensity profile of the He ion beam is also crucial. For our typical HIM parameters [a spot control (SC) value of 5 and an aperture of $10 \mu\text{m}$], we assume a Gaussian intensity profile with an estimated FWHM beam diameter $\varnothing \sim 9$ nm. The SC value for a given aperture diameter determines the width of the beam diameter. A higher SC value produces

TABLE I. Parameters of YBCO microbridges with pinning arrays reported in this paper. The length indicates the distance between the voltage probes. The critical temperature T_c is determined as the resistive transition's inflection point. The first magnetic matching field B_1 is calculated from Eq. (1) and confirmed by $I_c(B)$ and $R(B)$ measurements.

Name	Width (μm)	Length (μm)	Thickness (nm)	a (nm)	D (ki/dot)	T_c (K)	B_1 (T)
H30	8.0	20.0	26 ± 1	30 ± 0.6	10	75	2.7
H25	6.5	17.0	26 ± 1	25 ± 0.5	10	63	3.8
H20	5.0	13.5	37 ± 2	20 ± 0.5	10	52	6.0
H15	4.0	10.0	26 ± 1	15 ± 0.4	10	n/a	(10.6)

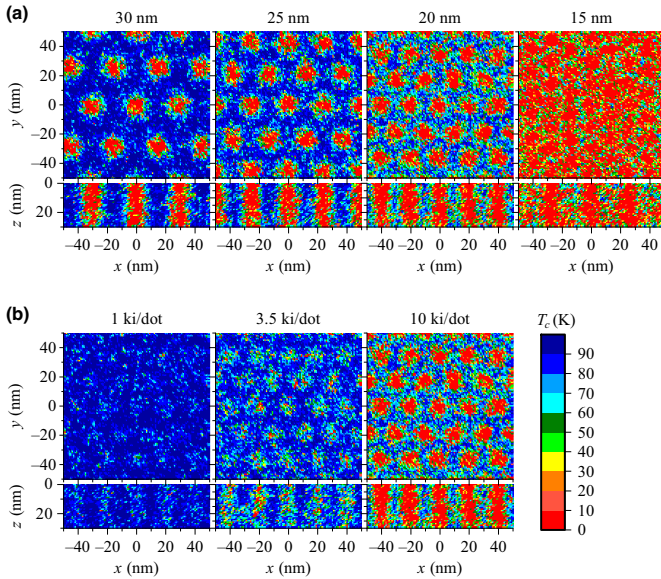


FIG. 2. Monte Carlo simulations of T_c suppression induced by He-FIB irradiation (with $\varnothing = 9$ nm) of YBCO; only the central parts of larger hexagonal patterns are shown. The x - y plots show cuts at $z = 15$ nm depth below the film surface, while the x - z plots show cuts at $y = 0$ nm. (a) Columnar defect (CD) lattices with various lattice spacings; $D = 10$ ki/dot. (b) CD lattices with $a = 20$ nm and various D .

a narrower beam profile at the expense of lower ion fluence and therefore longer irradiation time. For example, a narrow beam is required to draw lines across a YBCO microbridge to create Josephson junctions [37,38]. On the other hand, a lower SC value widens the beam and can lead to unwanted defects in the inter-CD areas, as discussed in Sec. IV A 2.

Throughout this work, we used a He-FIB with an energy of 30 keV. The irradiated area is limited by the field of view (FoV) of the HIM, and for optimum resolution of the HIM's beam deflection circuitry, the FoV should be $30 \times 30 \mu\text{m}^2$ or smaller. This provides a beam positioning accuracy of approximately 0.5 nm.

Several hexagonal arrays have been produced with spacings $a = 30, 25, 20, 15$ nm and doses ranging from $D = 1$ to 10 ki/dot. The different values of a were chosen to test the ultimate resolution that can be achieved. Here, we present the results for $D = 10$ ki/dot, which demonstrates the strongest pinning.

C. Transport measurements

The electrical measurements were carried out in a physical properties measurement system equipped with a 9-T superconducting solenoid and a variable temperature insert with a Cernox resistor for in-field temperature control (Quantum Design). For all experiments, the magnetic field was oriented perpendicular to the sample surface

(x - y plane), that is, the field is along the z axis. To rule out thermoelectric signals, resistance measurements were taken with constant excitation currents of 1.2–2.4 μA in both polarities. The magnetic field was swept in both polarities at fixed temperatures, and perfect mirror symmetry was observed. Furthermore, the results are independent of the magnetic field sweep direction and no hysteresis [26] was observed.

The critical current I_c is determined from isothermal voltage V versus current I measurements using a voltage criterion of 135 nV, which is above the noise floor of 40 nV and corresponds to an electric field $E = 100 \mu\text{V}/\text{cm}$. Supplementary resistance measurements in magnetic fields up to 12.5 T were performed in an Oxford Instruments helium bath cryostat.

III. SIMULATIONS

Our experiments were preceded by simulations of the expected $T_c(x, y, z)$ suppression patterns, which are summarized in Fig. 2. Briefly, atom displacement cascades due to He-FIB irradiation were calculated using the SRIM/TRIM program [39]. Individual He^+ atom impact points were shifted to simulate the Gaussian beam intensity distribution and the hexagonal irradiation pattern. The resulting three-dimensional landscapes of defects can be converted to local T_c values by using experimental data from uniformly large-area-irradiated thin YBCO films as

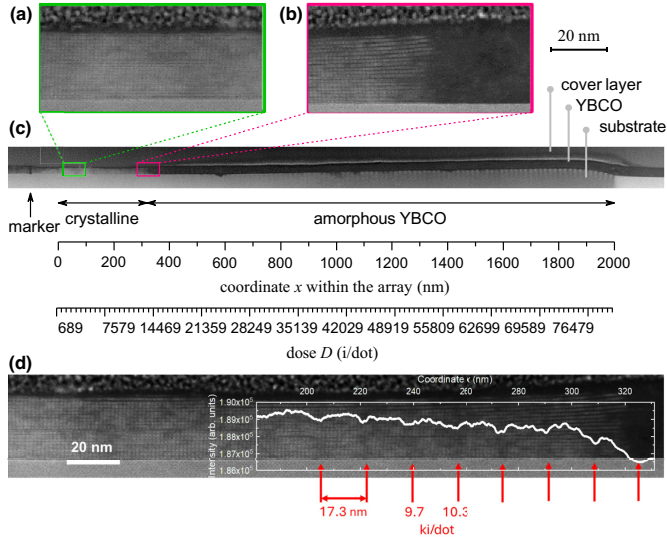


FIG. 3. Cross-sectional High-angle annular dark field STEM image of the lamella extracted from a hexagonal array of CDs with the lattice constant $a = 20$ nm, length 2000 nm in the x -direction. The array has a dose gradient along the x axis given by $D(x) = 689 \text{ i/dot} \cdot (N + 1) = 689 \text{ i/dot} \cdot (1 + x/a)$, where $N = 0, \dots, 115$ is the CD column number in the gradient direction and $a' = \sqrt{3}/2a \approx 17.32$ nm is the distance between the CDs in the x (D gradient) direction. (a),(b) Zoomed images in the region with preserved crystal structure and in the region with onset of amorphization ($x_c \approx 320$ nm, $D_c \approx 13$ ki/dot). (c) Overall view of the entire array. The scales below the image show the coordinate x within the array and the corresponding dose $D(x)$. Each small tick on the D axis corresponds to a position of a defect column (i.e., the distance between the ticks is a'). (d) The intensity profile (white) overlaid onto a selected part of the lamella's STEM image shows a slight contrast modulation with the periodicity a' . The red arrows indicate the locations of the irradiated spots.

calibration [40]. The size of the simulation cells is $1 \times 1 \times 1 \text{ nm}^3$, similar to the in-plane and larger than the out-of-plane coherence lengths of YBCO.

In Fig. 2(a), the red dots indicate hexagonal arrays of well-formed nanocolumns with suppressed T_c . They are well separated down to $a = 20$ nm, leaving a superconducting matrix in between. Because of the straggling of the ion trajectories, these inter-CD regions have a finite but smaller defect density and hence also slightly reduced T_c values. In contrast, the simulation of an array with $a = 15$ nm reveals little T_c contrast between defect columns and inter-CD regions, making the observation of matching effects unlikely.

Furthermore, proper dose selection is crucial, as demonstrated in Fig. 2(b) for a lattice with spacings $a = 20$ nm. Doses of $D \ll 10$ ki/dot do not entirely suppress superconductivity. They only decrease T_c locally, resulting in a weaker pinning potential, as shown in Fig. 4(a). Conversely, doses $D > 10$ ki/dot provide no additional benefit since the suppression of T_c is already maximal.

On the contrary, an excessive number of defects causes crystal lattice instabilities, which spread into neighboring regions and widen the defect columns.

IV. RESULTS AND DISCUSSION

A. Optimization of irradiation parameters

1. Irradiation dose

To maintain the crystalline framework of YBCO and still suppress its superconductivity, it is essential to determine the optimal number of 30 keV He^+ ions (referred to as dose D) to irradiate one dot of the pinning lattice. If the dose exceeds the threshold value D_c , it causes the breakdown of the crystalline structure, making the YBCO film amorphous. To identify D_c , a hexagonal array of dots was used with a distance of $a = 20$ nm. The dots were irradiated with increasing doses in steps of 689 i/dot from row to row, linearly from 0.689 ki/dot to 80 ki/dot, leaving the other irradiation parameters the same as for sample H20.

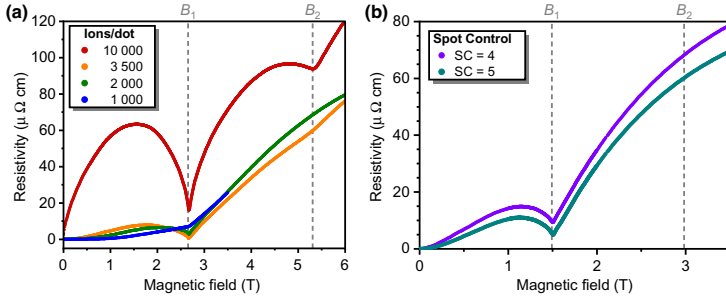


FIG. 4. Vortex-matching effects in the resistivity versus field curves of irradiated YBCO bridges. (a) Magnetoresistivity of four samples at $T/T_c \sim 0.96$ after irradiation with a $a = 30$ nm hexagonal pattern using $SC = 4$, and doses from 1 to 10 ki/dot. (b) Comparison of different spot control (SC) settings of the HIM. Two hexagonal pinning arrays with $a = 40$ nm were prepared with a dose $D = 2.0$ ki/dot on the same substrate. The magnetoresistivity at 86.5 K ($T/T_c \sim 0.96$) is plotted for $SC = 4$ and 5.

This array was characterized by aberration-corrected STEM in a probe-corrected FEI Titan 60-300 operated at 300 kV, equipped with a CEOS corrector for the condenser system, which provides a probe size below 1 Å. A high-angle annular dark field in STEM was used to provide Z-contrast images. The cross-sectional specimen was prepared by Ga^+ -FIB in an FEI Helios 650 Dual Beam FIB system. The bright bubble-like contrast on top of the YBCO film in Figs. 3(a) and 3(b) is the Pt-C deposit grown by focused electron beam induced deposition to protect the YBCO film during transmission electron microscopy (TEM) lamella preparation in SEM-FIB equipment. This is a standard procedure with negligible impact on the film quality due to the low dose and low energy of the electron beam used. The same type of coverage is used in the highly crystalline pristine areas, which does not evidence any apparent amorphization or beam damage.

The cross-sectional STEM image of the entire irradiated region is shown in Fig. 3(c). At low doses, the crystalline structure of YBCO is preserved, as can be seen in the magnified detail depicted in Fig. 3(a). At a critical dose, $D_c \approx 13$ ki/dot, the crystalline structure of YBCO disappears in the STEM image, indicating the amorphization of the film, as displayed in Fig. 3(b). Note that at $D \lesssim D_c$, the YBCO layer already begins to swell, but the surface of the substrate remains flat. Only at substantially higher D is the substrate also damaged, and individual beam tracks become clearly visible on the right in Fig. 3(c). This observation proves that the reported vortex-matching effects are not caused by local strain from the substrate, but rather originate from subtle modifications of the YBCO structure.

The intensity profile for $D \lesssim D_c$ shown as an overlay to the STEM image in Fig. 3(d) reveals a reduction with increasing x (i.e., increasing D) that begins when the YBCO lattice expands and reaches its lowest value in the

amorphized region. Intriguingly, it can clearly be seen that for $D < D_c$, the layered structure of YBCO is conserved, yet the intensity profile shows little dips with a periodicity of $a' = \sqrt{3}/2a$. Such an intensity depression is probably caused by the enhanced disorder in the CD channels. The width of the dips is up to 10 nm, supporting our previous estimate for the diameter of the CDs.

For lower dose values that do not cause visible damage, no signatures of the irradiation are visible in STEM images. However, the CDs created with lower doses strongly influence the behavior of magnetic flux quanta, as seen in electric transport measurements. The observation of magnetic-field commensurability effects with the flux-line lattice is a direct probe of efficient vortex pinning in periodic pinning landscapes. Minima of the resistivity and maxima of the critical current appear at so-called matching fields

$$B_k = k\Phi_0/A, \quad (1)$$

where k is an integer or rational number of vortices contained within the unit cell of the hexagonal pinning array with area $A = \frac{\sqrt{3}}{2}a^2$. The field B_1 corresponds to the flux density of one vortex per pinning site. When the magnetic field $B > B_1$, one of two scenarios may occur: either some or all CDs are filled with multi-quanta vortices when the CD radius is larger than the (in-plane) coherence length or interstitial vortices enter between the CDs [41].

The question of how lower doses $D \ll D_c$ influence the efficiency of the pinning lattices was investigated in several microbridges prepared on the same substrate. The bridges were patterned with a hexagonal $a = 30$ nm CD lattice using different doses but otherwise identical conditions. Figure 4(a) shows the resistivity ρ versus the applied magnetic field B of these bridges. Because T_c

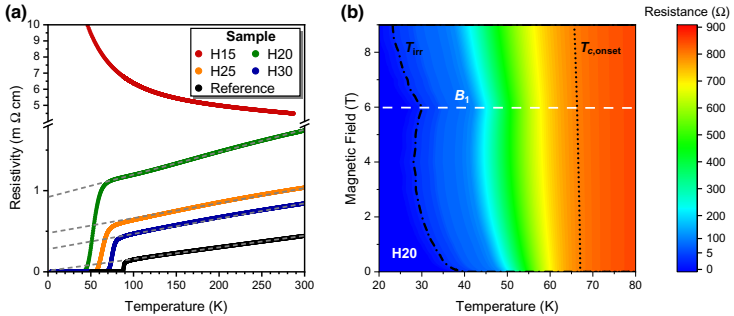


FIG. 5. (a) Resistivity versus temperature (at $B = 0$) of YBCO microbridges patterned with a hexagonal array of CDs of various spacings a by He-FIB irradiation with dose $D = 10$ ki/dot. Extrapolations of the normal-state resistivities are shown by dashed lines. The black line shows the data of a nonirradiated reference film. (b) Color-coded contour plot of the resistance of sample H20 as a function of temperature and magnetic field. The dotted line represents the onset of superconductivity, $T_{c,onset}$, taken as 90% of the normal-state resistance value at 100 K, $R(100$ K). The dashed-dotted line estimates the irreversibility line T_{irr} , using a criterion of 0.1% of $R(100$ K).

decreases with increasing D , the data were taken at the same normalized $T/T_c \sim 0.96$. Although commensurability effects are barely visible at $D = 1$ ki/dot, they appear at higher doses. Still, the $\rho(B)$ curves of the bridges with $D \leq 3.5$ ki/dot are similar and do not show matching dips at B_2 . Only for $D = 10$ ki/dot is there a clear matching effect at B_2 , and, moreover, the minimum at B_1 is remarkably pronounced. These experimental results confirm the simulation results presented in Fig. 2(b) and point to an optimal dose $D = 10$ ki/dot for our experiments.

2. Spot control

The SC value specifies the strength of the HIM's condenser lens, thus setting the position of the crossover point in the ion optical column. For a given aperture diameter, a higher SC value thus produces a narrower beam profile at the expense of lower ion fluence and longer irradiation time. For SC = 5 used in this study we estimate a beam diameter of FWHM $\varnothing \approx 9$ nm on the sample surface. At a dose of 10 ki/dot the dwell time of the beam for a single spot is about 3 ms, and the total irradiation time of the bridge is approximately 40 min for the lattice spacing $a = 30$ nm.

The processing time can be reduced by a factor of about 2 using SC = 4. To test the consequences, the resistivities at 86.5 K are compared as a function of the applied magnetic field in Fig. 4(b). The two bridges with a hexagonal CD pattern of $a = 40$ nm were manufactured from the same YBCO film and treated identically, except for the choice of SC. Despite the similarity of the vortex-matching characteristics, the resistivity of the SC = 4 bridge is

higher due to a wider tail of the ion beam profile, resulting in a higher defect density between the irradiated spots.

B. Resistivity and critical current

The microbridges described in Table 1 were further studied by electrical transport measurements. Figure 5(a) depicts the resistivity $\rho(T)$ of all four microbridges with arrays written using $D = 10$ ki/dot together with a non-irradiated reference film. The samples with $A = 30, 25,$ and 20 nm exhibit a metallic temperature dependence in the normal state and a critical temperature that decreases with smaller spacing. An invariance of the slope indicates that no oxygen is lost during irradiation [33], while the rising offset of a straight line extrapolated from the normal state indicates an increase in the number of defects in the percolation paths between the CDs. This observation is consistent with the decline of T_c and the simulation results presented in Fig. 2(a).

In contrast, the array with $a = 15$ nm displays a semi-conducting $\rho(T)$ dependence and does not become superconducting even at our lowest measurement temperature of 2 K. When the CDs are placed at such a close spacing, they begin to overlap and impede the supercurrent between the CDs. This observation from the resistivity measurements for variable a supports our estimate of the He-FIB's fluence profile $\varnothing = 9$ nm in the simulations.

In order to further investigate the superconducting transition of sample H20, we measured $R(T)$ for different magnetic fields, as shown in Fig. 5(b). The dotted line represents the onset of superconducting percolation paths between the CDs, $T_{c,onset}(B)$, which is defined as $R(T_{c,onset}, B) = 0.9R(100$ K, $B)$. The steep slope

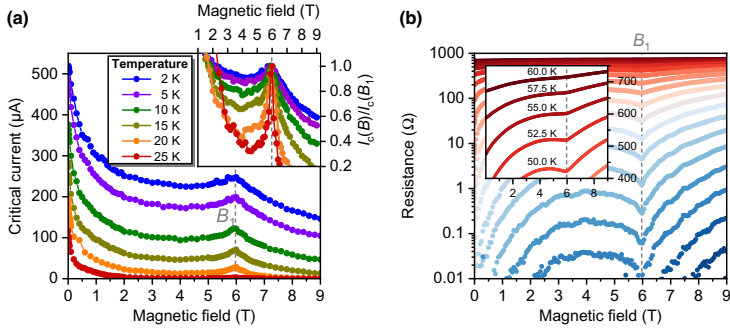


FIG. 6. Effects of vortex commensurability in sample H20. (a) Critical current versus applied magnetic field at various temperatures. The inset shows the critical current normalized to its value at the matching field B_1 . (b) Resistance versus applied magnetic field at temperatures from 17.5 K (dark blue symbols) to 60 K (dark red symbols) in 2.5 K steps. The inset shows details at higher temperatures.

$-dB/dT_{c,\text{onset}}$ implies that the upper critical field $B_{c2}(0\text{ K})$ is very high. Remarkably, no features in $T_{c,\text{onset}}(B)$ are observed at the first matching field $B_1 = 6.0\text{ T}$ [horizontal dashed line in Fig. 5(b)]. This suggests that in the strong fluctuation and vortex liquid regime near $T_{c,\text{onset}}(B)$, the current paths between the CDs are basically unaffected by the pinning array and the slope of $T_{c,\text{onset}}(B)$ is comparable to that of nonirradiated films. In contrast, we observe a distinct peak of the irreversibility temperature $T_{\text{irr}}(B)$, defined as $R(T_{\text{irr}}, B) = 10^{-3}R(100\text{ K}, B)$, right at B_1 . This indicates that the onset of dissipation caused by moving vortices is significantly shifted to higher temperatures when the vortices can arrange themselves commensurably with the CD array.

The vortex-matching effects can be investigated more directly by critical current $I_c(B)$ (static probe) or resistance $R(B)$ (dynamic property of moving vortices) measurements. The $I_c(B)$ curves in Fig. 6(a), taken at six different temperatures from 2 to 25 K, show peaks at $B_1 = 6.0\text{ T}$, which remain visible even down to $T = 2\text{ K}$. The inset of the figure highlights these peaks by normalizing I_c to $I_c(B_1)$. As the temperature increases, the pinning force of intrinsic defects decreases faster than that of CDs [42], which makes the peaks even more pronounced. It is worth noting that previous works [16–18,23,25–27,34,43–49] did not identify commensurability effects at such high magnetic fields. Furthermore, the vortex matching observed in our samples continues to occur even at very low temperatures. These observations are a natural consequence of ultradense and strong pinning sites created by He-FIB irradiation.

From Fig. 6(a) it is evident that the pinning effect remains strong not only at B_1 but also throughout the field range $0 \leq B < B_1$, where commensurability effects are less significant. The minimum value of I_c , which roughly

corresponds to the weakest pinning sites, is reached at about 4 T at low temperatures. At the lowest temperature $T = 2\text{ K}$, $I_c(B = 4\text{ T})$ is only half the value of $I_c(B = 0)$. However, for $B > B_1$ the pinning becomes less effective and I_c decays more rapidly. While at $B < B_1$ every vortex can, in principle, be pinned solely in a CD, this is not the case for $B > B_1$. Then an arrangement of multiquantum vortices in the CDs or interstitial vortices occurs, which is energetically less favorable. Thus, the value of B_1 sets an upper limit to the typical range of strong pinning that is relevant for practical applications. This implies that shifting B_1 to high magnetic fields is essential, which is possible with the method presented here.

On the high-temperature side, up to about 60 K, the vortex-matching effects are probed via reduced vortex mobility, resulting in minima of the resistance as shown in Fig. 6(b). This suggests that even at 80% of the normal-state resistance value $R(100\text{ K})$, correlations between vortices do exist. Hence, the vortex ensemble is not entirely melted but instead moves through a plastic vortex flow [50]. Voltage-current isotherms in sample H30 indicate that the interaction of artificial and intrinsic defects results in an ordered Bose glass state [51,52].

The magnetoresistance of sample H20 was investigated up to 12.5 T in a separate series of measurements. Figure 7 shows the $R(B)$ curves at temperatures from 17 to 55 K. Some measurements were taken at both magnetic field polarities to confirm the perfect mirror symmetry of the data. We do not find matching features [dips in $R(B)$] at $B_2 = 12.0\text{ T}$, though minima in $R(B)$ at B_2 are visible for the H30 bridge with a wider hexagonal $a = 30\text{ nm}$ CD array [see Fig. 4(a)]. In addition, $I_c(B)$, measured on the H20 bridge at lower temperatures, did not reveal any commensurability signatures at B_2 . One possible explanation is that the dynamics of interstitial vortices

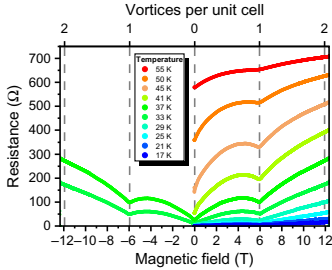


FIG. 7. Resistance versus applied magnetic field at various temperatures of the YBCO microbridge H20 patterned with a hexagonal array of CDs (spacing $a = 20$ nm and dose $D = 10$ ki/dot). Some data were collected in both polarities of the magnetic field and confirm the symmetry $R(B) = R(-B)$.

changes when the channels between the CDs become narrow. Such details of vortex-matching properties in ultradense pinning landscapes deserve further investigation.

V. CONCLUSIONS

To summarize, irradiating thin YBCO films with a 30-keV focused helium ion beam of undercritical dose $D < D_c$ is an excellent approach for introducing user-defined patterns of suppressed critical temperature. After evaluating the appropriate irradiation conditions, we demonstrated the ability to create ultradense hexagonal pinning arrays with a spacing as low as $a = 20$ nm. These arrays exhibit strong pinning across a wide range of magnetic fields up to the first matching field of 6 T. The overlap of neighboring CDs sets the present experimental minimum separation of the pins at $15 \text{ nm} < a \leq 20 \text{ nm}$. However, it is possible that further adjustment of irradiation parameters could slightly reduce this constraint.

Our experiments have shown that vortex-matching effects can be observed even at low temperatures of 2 K, where superconductivity is stable and not affected by fluctuations. This paves the way for designing more effective pinning landscapes that can operate at several tesla and at temperatures much lower than the critical temperature, avoiding the undesirable vortex liquid and fluctuation regimes.

Our findings have expanded the range of temperatures and magnetic fields that can be studied with *regular* artificial pinning landscapes. In order to bring the theoretical concepts in the field of fluxonics [6,8,10,11] into practical use and to facilitate high operating frequencies, it is essential to confine vortices to designed features with the smallest possible size [9]. With our findings, it is now possible to create complex pinning patterns with narrow spacing that can be utilized in applications such as

vortex-based cellular automata for fast logic with low power consumption [9,10]. Future developments in He-FIB instrumentation, such as a multibeam technique [53], would further augment the versatility of the presented method.

ACKNOWLEDGMENTS

We are grateful for insightful discussions with John Nottle (ZEISS Semiconductor Manufacturing Technology) and Gregor Hlawacek (Helmholtz-Zentrum Dresden-Rossendorf). B.B. acknowledges financial support from the Vienna Doctoral School in Physics (VDSP). O.D. acknowledges financial support from the Austrian Science Fund (FWF) under Grant No. I6079-N (FluMag). Work by O.D. was funded by the Deutsche Forschungsgemeinschaft (DFG, German Research Foundation) under Germany's Excellence Strategy – EXC-2123 Quantum-Frontiers – 390837967. C.M. acknowledges financial support from Regional Gobierno de Aragón through Project No. E13_23R, including FEDER funding and from the EU Horizon 2020 programme under Grant Agreement No. 823717-ESTEEM3. The authors acknowledge the use of instrumentation as well as the technical advice provided by the National Facility ELECMi ICTS, node “Laboratorio de Microscopías Avanzadas (LMA)” at Universidad de Zaragoza. The research was funded in whole, or in part, by the Austrian Science Fund (FWF) Grant No. I4865-N and the German Research Foundation (DFG), Grant No. KO 1303/16-1. For the purpose of open access, the authors have applied a CC-BY public copyright license to any author-accepted manuscript version arising from this submission. The research is based upon work from COST Actions CA19140 (FIT4NANO), CA21144 (SuperQuMap), and CA19108 (Hi-SCALE) supported by COST (European Cooperation in Science and Technology).

- [1] G. Blatter, M. V. Feigel'man, V. B. Geshkenbein, A. I. Larkin, and V. M. Vinokur, Vortices in high-temperature superconductors, *Rev. Mod. Phys.* **66**, 1125 (1994).
- [2] J. Pearl, Current distribution in superconducting films carrying quantized fluxoids, *Appl. Phys. Lett.* **5**, 65 (1964).
- [3] C. Sekirnjak, W. Lang, S. Proyer, and P. Schwab, Novel approach for the analysis of the fluctuation magnetoconductivity in $\text{YBa}_2\text{Cu}_3\text{O}_7$ thin films, *Physica C* **243**, 60 (1995).
- [4] D. Rohner, L. Thiel, B. Müller, M. Kasperczyk, R. Kleiner, D. Koelle, and P. Maletinsky, Real-space probing of the local magnetic response of thin-film superconductors using single spin magnetometry, *Sensors* **18**, 3790 (2018).
- [5] M. J. Martínez-Pérez, B. Müller, D. Schwebius, D. Korinski, R. Kleiner, J. Sesé, and D. Koelle, NanoSQUID magnetometry of individual cobalt nanoparticles grown by focused

- electron beam induced deposition, *Supercond. Sci. Technol. – Focus Issue on NanoSQUIDs and Their Applications* **30**, 024003 (2017).
- [6] T. Golod, A. Iovan, and V. M. Krasnov, Single Abrikosov vortices as quantized information bits, *Nat. Commun.* **6**, 8628 (2015).
- [7] I. Keren, A. Gutfreund, A. Noah, N. Fridman, A. Di Bernardo, H. Steinberg, and Y. Anahory, Chip-integrated vortex manipulation, *Nano Lett.* **23**, 4669 (2023).
- [8] J. F. Wambaugh, C. Reichhardt, C. J. Olson, F. Marchesoni, and F. Nori, Superconducting fluxon pumps and lenses, *Phys. Rev. Lett.* **83**, 5106 (1999).
- [9] M. B. Hastings, C. J. Olson Reichhardt, and C. Reichhardt, Ratchet cellular automata, *Phys. Rev. Lett.* **90**, 247004 (2003).
- [10] M. V. Milošević, G. R. Berdiyrov, and F. M. Peeters, Fluxonic cellular automata, *Appl. Phys. Lett.* **91**, 212501 (2007).
- [11] T. Golod, L. Morlet-Decarnin, and V. M. Krasnov, Word and bit line operation of a $1 \times 1 \mu\text{m}^2$ superconducting vortex-based memory, *Nat. Commun.* **14**, 4926 (2023).
- [12] A. Libál, C. J. Olson Reichhardt, and C. Reichhardt, Creating artificial ice states using vortices in nanostructured superconductors, *Phys. Rev. Lett.* **102**, 237004 (2009).
- [13] J. E. Villegas, S. Savel'ev, F. Nori, E. M. Gonzalez, J. V. Anguita, R. Garcia, and J. L. Vicent, A superconducting reversible rectifier that controls the motion of magnetic flux quanta, *Science* **302**, 1188 (2003).
- [14] Y.-Y. Lyu, J. Jiang, Y.-L. Wang, Z.-L. Xiao, S. Dong, Q.-H. Chen, M. V. Milošević, H. Wang, R. Divan, J. E. Pearson, P. Wu, F. M. Peeters, and W.-K. Kwok, Superconducting diode effect via conformal-mapped nanoholes, *Nat. Commun.* **12**, 2703 (2021).
- [15] J. Trastoy, M. Malnou, C. Ulysse, R. Bernard, N. Bergeal, G. Faini, J. Lesueur, J. Briatico, and J. E. Villegas, Freezing and thawing of artificial ice by thermal switching of geometric frustration in magnetic flux lattices, *Nat. Nanotechnol.* **9**, 710 (2014).
- [16] V. V. Moshchalkov and J. Fritzsche, *Nanostructured Superconductors* (World Scientific, Singapore, 2011).
- [17] A. Castellanos, R. Wördenweber, G. Ockenfuss, A. v.d. Hart, and K. Keck, Preparation of regular arrays of antidots in $\text{YBa}_2\text{Cu}_3\text{O}_7$ thin films and observation of vortex lattice matching effects, *Appl. Phys. Lett.* **71**, 962 (1997).
- [18] S. Avci, Z. L. Xiao, J. Hua, A. Imre, R. Divan, J. Pearson, U. Welp, W. K. Kwok, and G. W. Crabtree, Matching effect and dynamic phases of vortex matter in $\text{Bi}_2\text{Sr}_2\text{CaCu}_2\text{O}_8$ nanoribbon with a periodic array of holes, *Appl. Phys. Lett.* **97**, 042511 (2010).
- [19] W. Vinckx, J. Vanacken, V. V. Moshchalkov, S. Mátéfi-Tempfi, M. Mátéfi-Tempfi, S. Michotte, and L. Piraux, Vortex pinning in superconducting Nb thin films deposited on nanoporous alumina templates, *Eur. Phys. J. B* **53**, 199 (2006).
- [20] F. Kahlmann, A. Engelhardt, J. Schubert, W. Zander, C. Buchal, and J. Holikott, Superconductor-normal-superconductor Josephson junctions fabricated by oxygen implantation into $\text{YBa}_2\text{Cu}_3\text{O}_{7-\delta}$, *Appl. Phys. Lett.* **73**, 2354 (1998).
- [21] A. S. Katz, S. I. Woods, and R. C. Dynes, Transport properties of high- T_c planar Josephson junctions fabricated by nanolithography and ion implantation, *J. Appl. Phys.* **87**, 2978 (2000).
- [22] D. J. Kang, G. Burnell, S. J. Lloyd, R. S. Speaks, N. H. Peng, C. Jeynes, R. Webb, J. H. Yun, S. H. Moon, B. Oh, E. J. Tarte, D. F. Moore, and M. G. Blamire, Realization and properties of $\text{YBa}_2\text{Cu}_3\text{O}_{7-\delta}$ Josephson junctions by metal masked ion damage technique, *Appl. Phys. Lett.* **80**, 814 (2002).
- [23] I. Swiecicki, C. Ulysse, T. Wolf, R. Bernard, N. Bergeal, J. Briatico, G. Faini, J. Lesueur, and J. E. Villegas, Strong field-matching effects in superconducting $\text{YBa}_2\text{Cu}_3\text{O}_{7-\delta}$ films with vortex energy landscapes engineered via masked ion irradiation, *Phys. Rev. B* **85**, 224502 (2012).
- [24] W. Lang, M. Dineva, M. Marksteiner, T. Enzenhofer, K. Siraj, M. Peruzzi, J. D. Pedarnig, D. Bäuerle, R. Kornrner, E. Cekan, E. Platzgummer, and H. Loeschner, Ion-beam direct-structuring of high-temperature superconductors, *Microelectron. Eng.* **83**, 1495 (2006).
- [25] L. T. Haag, G. Zechner, W. Lang, M. Dosmailov, M. A. Bodea, and J. D. Pedarnig, Strong vortex matching effects in YBCO films with periodic modulations of the superconducting order parameter fabricated by masked ion irradiation, *Physica C* **503**, 75 (2014).
- [26] G. Zechner, F. Jausner, L. T. Haag, W. Lang, M. Dosmailov, M. A. Bodea, and J. D. Pedarnig, Hysteretic vortex-matching effects in high- T_c superconductors with nanoscale periodic pinning landscapes fabricated by He ion-beam projection, *Phys. Rev. Appl.* **8**, 014021 (2017).
- [27] G. Zechner, K. L. Mletschnig, W. Lang, M. Dosmailov, M. A. Bodea, and J. D. Pedarnig, Unconventional critical state in $\text{YBa}_2\text{Cu}_3\text{O}_{7-\delta}$ thin films with a vortex-pin lattice fabricated by masked He^+ ion beam irradiation, *Supercond. Sci. Technol.* **31**, 044002 (2018).
- [28] G. Zechner, W. Lang, M. Dosmailov, M. A. Bodea, and J. D. Pedarnig, Transverse vortex commensurability effect and sign change of the Hall voltage in superconducting $\text{YBa}_2\text{Cu}_3\text{O}_{7-\delta}$ thin films with a nanoscale periodic pinning landscape, *Phys. Rev. B* **98**, 104508 (2018).
- [29] R. L. Gray, M. J. D. Rushton, and S. T. Murphy, Molecular dynamics simulations of radiation damage in $\text{YBa}_2\text{Cu}_3\text{O}_7$, *Supercond. Sci. Technol.* **35**, 035010 (2022).
- [30] S. J. Rothman, J. L. Routbort, and J. E. Baker, Tracer diffusion of oxygen in $\text{YBa}_2\text{Cu}_3\text{O}_{7-\delta}$, *Phys. Rev. B* **40**, 8852 (1989).
- [31] S. K. Tolpygo, J. Y. Lin, M. Gurvitch, S. Y. Hou, and J. M. Phillips, Effect of oxygen defects on transport properties and T_c of $\text{YBa}_2\text{Cu}_3\text{O}_{5+x}$: Displacement energy for plane and chain oxygen and implications for irradiation-induced resistivity and T_c suppression, *Phys. Rev. B* **53**, 12462 (1996).
- [32] W. Lang, H. Richter, M. Marksteiner, K. Siraj, M. A. Bodea, J. D. Pedarnig, C. Grigoropoulos, D. Bäuerle, C. Hasenfuss, L. Palmethofer, R. Kolarova, and P. Bauer, Masked ion beam irradiation of high-temperature superconductors: Patterning of nano-size regions with high point-defect density, *Int. J. Nanotechnol.* **6**, 704 (2009).

- [33] W. Lang and J. D. Pedarnig, Ion irradiation of high-temperature superconductors and its application for nanopatterning, in *Nanoscience and Engineering in Superconductivity*, edited by V. V. Moshchalkov, R. Wördenwæber, and W. Lang (Springer, Berlin, 2010), p. 81.
- [34] C. Yang, H. Liu, Y. Liu, J. Wang, D. Qiu, S. Wang, Y. Wang, Q. He, X. Li, P. Li, Y. Tang, J. Wang, X. C. Xie, J. M. Valles, J. Xiong, and Y. Li, Signatures of a strange metal in a bosonic system, *Nature* **601**, 205 (2022).
- [35] *Helium Ion Microscopy*, edited by G. Hlawacek and A. Gözlhäuser (Springer International Publishing, Cham, 2016).
- [36] D. Niebieskikwiat, A. Silhanek, L. Civale, G. Niewa, P. Levy, and L. Krusin-Elbaum, Suppression of matching field effects by splay and pinning energy dispersion in $\text{YBa}_2\text{Cu}_3\text{O}_7$ with columnar defects, *Phys. Rev. B* **63**, 144504 (2001).
- [37] S. A. Cybart, E. Y. Cho, T. J. Wong, B. H. Wehlin, M. K. Ma, C. Huynh, and R. C. Dynes, Nano Josephson superconducting tunnel junctions in $\text{YBa}_2\text{Cu}_3\text{O}_{7-\delta}$ directly patterned with a focused helium ion beam, *Nat. Nanotechnol.* **10**, 598 (2015).
- [38] B. Müller, M. Karrer, F. Limberger, M. Becker, B. Schröpel, C. J. Burkhardt, R. Kleiner, E. Goldobin, and D. Koelle, Josephson junctions and SQUIDS created by focused helium-ion-beam irradiation of $\text{YBa}_2\text{Cu}_3\text{O}_7$, *Phys. Rev. Appl.* **11**, 044082 (2019).
- [39] J. F. Ziegler, M. D. Ziegler, and J. P. Biersack, SRIM – the stopping and range of ions in matter (2010), *Nucl. Instrum. Methods Phys. Res., Sect. B* **268**, 1818 (2010).
- [40] K. L. Mletschnig and W. Lang, Nano-patterning of cuprate superconductors by masked He^+ ion irradiation: 3-dimensional profiles of the local critical temperature, *Microelectron. Eng.* **215**, 110982 (2019).
- [41] A. I. Buzdin, Multiple-quanta vortices at columnar defects, *Phys. Rev. B* **47**, 11416 (1993).
- [42] I. B. Khalfin and B. Y. Shapiro, Relaxation of magnetic flux in a superconductor with a system of columnar defects, *Physica C* **207**, 359 (1993).
- [43] J. Y. Lin, M. Gurvitch, S. K. Tolpygo, A. Bourdillon, S. Y. Hou, and J. M. Phillips, Flux pinning in $\text{YBa}_2\text{Cu}_3\text{O}_{7-\delta}$ thin films with ordered arrays of columnar defects, *Phys. Rev. B* **54**, R12717 (1996).
- [44] R. Córdoba, T. I. Baturina, J. Sesé, A. Y. Mironov, J. M. de Teresa, M. R. Ibarra, D. A. Nasimov, A. K. Gutakovskii, A. V. Latyshev, I. Guillamón, H. Suderow, S. Vieira, M. R. Baklanov, J. J. Palacios, and V. M. Vinokur, Magnetic field-induced dissipation-free state in superconducting nanostructures, *Nat. Commun.* **4**, 1437 (2013).
- [45] N. Poccia, T. I. Baturina, F. Coneri, C. G. Molenaar, X. R. Wang, G. Bianconi, A. Brinkman, H. Hilgenkamp, A. A. Golubov, and V. M. Vinokur, Critical behavior at a dynamic vortex insulator-to-metal transition, *Science* **349**, 1202 (2015).
- [46] I. G. Serrano, J. Sesé, I. Guillamón, H. Suderow, S. Vieira, M. R. Ibarra, and J. M. de Teresa, Thickness-modulated tungsten-carbon superconducting nanostructures grown by focused ion beam induced deposition for vortex pinning up to high magnetic fields, *Beilstein J. Nanotechnol.* **7**, 1698 (2016).
- [47] O. V. Dobrovolskiy, V. M. Bevz, M. Y. Mikhailov, O. L. Yuzepovich, V. A. Shklovskij, R. V. Vovk, M. I. Tsindlekht, R. Sachser, and M. Huth, Microwave emission from superconducting vortices in Mo/Si superlattices, *Nat. Commun.* **9**, 4927 (2018).
- [48] B. Aichner, B. Müller, M. Karrer, V. R. Misko, F. Limberger, K. L. Mletschnig, M. Dosmailov, J. D. Pedarnig, F. Nori, R. Kleiner, D. Koelle, and W. Lang, Ultradense tailored vortex pinning arrays in superconducting $\text{YBa}_2\text{Cu}_3\text{O}_{7-\delta}$ thin films created by focused He ion beam irradiation for fluxonics applications, *ACS Appl. Nano Mater.* **2**, 5108 (2019).
- [49] C. Yang, Y. Liu, Y. Wang, L. Feng, Q. He, J. Sun, Y. Tang, C. Wu, J. Xiong, W. Zhang, X. Lin, H. Yao, H. Liu, G. Fernandes, J. Xu, J. M. Valles, J. Wang, and Y. Li, Intermediate bosonic metallic state in the superconductor-insulator transition, *Science* **366**, 1505 (2019).
- [50] C. Reichhardt and C. J. Olson Reichhardt, Depinning and nonequilibrium dynamic phases of particle assemblies driven over random and ordered substrates: A review, *Rep. Prog. Phys.* **80**, 026501 (2017).
- [51] L. Backmeister, B. Aichner, M. Karrer, K. Wurster, R. Kleiner, E. Goldobin, D. Koelle, and W. Lang, Ordered Bose glass of vortices in superconducting $\text{YBa}_2\text{Cu}_3\text{O}_{7-\delta}$ thin films with a periodic pin lattice created by focused helium ion irradiation, *Nanomaterials* **12**, 3491 (2022).
- [52] B. Aichner, L. Backmeister, M. Karrer, K. Wurster, R. Kleiner, E. Goldobin, D. Koelle, and W. Lang, Angle-dependent magnetoresistance of an ordered Bose glass of vortices in $\text{YBa}_2\text{Cu}_3\text{O}_{7-\delta}$ thin films with a periodic pinning lattice, *Condens. Matter* **8**, 32 (2023).
- [53] K. Höflich, *et al.*, Roadmap for focused ion beam technologies, *Appl. Phys. Rev.* **10**, 041311 (2023).